UNIVERSITÀ DEGLI STUDI DI UDINE
hic sunt futura

www.uniud.it

UNIVERSITÀ DEGLI STUDI DI UDINE
Dipartimento Politecnico di Ingegneria e Architettura

Ph.D. course
Industrial and Information Engineering
XXXI cycle

collaboration agreement with
Centro di Riferimento Oncologico CRO - IRCCS Aviano
Dipartimento della Ricerca e della Diagnostica Avanzata dei Tumori

Ph.D. Thesis

New devices and methodologies for the study of blood coagulation and its related pathologies from impedance measurements and digital images

Ph.D. Candidate
Denise De Zanet

Supervisor
Prof. Antonio Affanni
Co-Supervisor
Dr. Mario Mazzucato

Academic Year 2018/2019

To those who believed in me
more than I have ever done.

Your time is limited
so don't waste it
living someone else's life.
Don't let the noise of others' opinions
drown out your own inner voice.
Have the courage to follow
your heart and intuition.

Your work is going to fill
a large part of your life
and the only way to be truly satisfied
is to do what you believe is great work.
If you haven't found it yet
keep looking. Don't settle.
As with all matters of the heart
you'll know when you find it.

Steve Jobs

Abstract

This thesis describes the contributions in investigating the blood behavior both in physiological and pathological conditions. The Ph.D. activity outcomes are represented by two biosensors, one algorithm and one software, here subsequently presented.

The first topic of the thesis regards an impedance-based biosensor to measure and monitor in real time the thrombus formation and its related risk under flow conditions. The fast and accurate monitoring of the individual thrombotic risk represents a challenge in cardiovascular diagnostics and in treatment of hemostatic diseases. Actually, the thrombotic condition is quantified in laboratories only through static measurements that do not reproduce the dynamic physiological conditions of the blood circulation. Sometimes, in few laboratories, an additional information is provided by measuring the whole volume of thrombi formed *in vitro* under flow conditions. Thrombus volume, as representative index of the related thrombotic status, is usually estimated with confocal microscope at the end of each *in vitro* experiment, without providing a useful behavioral information about the biological sample in terms of platelets adhesion and aggregation in flowing blood. A new biosensor for the real-time analysis of thrombus formation is reported. The device has been developed to work either independently or integrated with the microscopy system. Thus, images of the fluorescently labeled platelets were acquired in real-time during the whole blood perfusion, while the global electrical impedance of the blood sample was simultaneously monitored between a pair of specifically designed gold microelectrodes. Fusing optical and electrical data with a novel technique, the dynamic of thrombus formation events in flowing blood could be reconstructed in real-time, allowing an accurate extrapolation of the three-dimensional shape and the spatial distribution of platelet thrombi forming and growing within the artificial capillaries. This biosensor revealed accurate and it has been used to discriminate different hemostatic conditions and to identify weakening and detaching platelet aggregates. The results obtained appeared compatible with those quantified with the traditional optical thresholding method. With advantages in terms of small size, user-friendliness and promptness of response, the biosensor can be proposed as a promising device for the fast and automatic individual health monitoring also at the point of care.

The second topic is related to a new algorithm for the improvement of accuracy in thrombus volumes estimation starting from three-dimensional images

acquired with the confocal scanning microscope. The accuracy of quantitative measurements represents an essential pre-requisite to characterize and define the complex dynamic phenomena occurring in the field of cell biology. In research projects that involve the induction of blood coagulation under flow in microfluidic artificial channels, thrombus volume represents an important parameter to be quantified as a significant index related to the individual thrombotic risk profile. For its importance in the early diagnosis of cardiovascular diseases, the estimated thrombus volume should reflect and represent the related real condition. In three-dimensional confocal microscopy, systematic errors can arise from distortions of the axial distance, whose accurate calibration remains a challenge. As a result, the volumetric three-dimensional reconstructions usually show a noticeable axial elongation and the volumes are thus overestimated. A 400-600 % of volume overestimation have been demonstrated and a new easy-to-use and automatic calibration procedure is proposed and described for this specific microfluidic and optical context. The adaptive algorithm proposed leads to the automatic compensation of the elongation error and thus allows to achieve an accurate thrombus volume measurement. The method has been calibrated using fluorescent beads of known volume, validated with groups of few distinct and visually countable platelets and finally applied on platelets thrombi.

The third topic of the thesis is represented by another biosensor to perform fast quality controls of blood quality in the pre-analytical phase in order to reduce or avoid laboratories analytical errors. In clinical laboratories, the major quantity of errors regarding blood analyses occurs in the pre-analytical phase. Pre-analytical conditions are key factors necessary to maintain the high quality of specimens, to limit day-to-day and batch variations and to guarantee the absolute reliability and accuracy of clinical results and related diagnoses. In particular, the quality of serum samples would have to be very high in order to avoid interferences due to hemolysis, thus preventing measurement errors. In addition, the quality of blood should be always fast monitored to identify inadequacies and guarantee their complete usability in transfusion procedures. In a near future, a possible solution could be supplying laboratories with smart and portable devices able to perform fast pre-analytical quality tests for every samples. Electrical impedance has a relevant potential in analyzing and monitoring blood quality. The proposal is a new simple impedance-based biosensor able to perform accurate and efficient single- and multi-frequency impedance measurements in the pre-analytical phase and to check in real-time the quality of the samples through quantitative thresholds as useful indicators to ensure the reliability of results and preventing laboratory errors. The sensor allows the discrimination of the different blood components, the identification of also a very little presence of hemolysis in serum, the evaluation of the blood quality and the rapid quantification of its hematocrit.

The last topic consists of the development of a new software for live cells imaging, in particular for signaling pathways investigation and analysis. The

progress in fluorescence microscopy and in information technologies have completely transformed the study of live cells improving the capability to quantify, to investigate and to analyze, in time and space, single phenomena occurring inside and outside cells. An user-friendly graphical user interface able to extract and analyze ion calcium signals was developed to understand how signaling pathways regulate cell behavior and metabolism. The software, named FluoLab, works on acquired confocal fluores-cence microscopy images and allows to obtain signals of mean representative fluorescence intensity for each object or cell analyzed. Afterwards, the fluorescence signals can be automatically converted in ion calcium concentration values [Ca^{2+}], expressed in micro-molarity [μM], by using the dissociation constant specific for each kind of fluorescent probes chosen to label the objects before the experiments. With FluoLab it is possible to analyze at the same time more than one object through the regions of interest defined around them and also objects of different type and different spatial hierarchy. The classical action of background compensation, normalization and smoothing of signals are implemented. This software shows versatility, visual immediacy and quickness in obtaining signals.

Contents

List of Figures

List of Tables

1. Introduction

Blood is a biological fluid that circulates throughout the body and contains extensive information on the state of health and diseases. It is composed by a conductive liquid called plasma and a suspension of particles, such as red blood cells, white blood cells and platelets. Once blood coagulates, cells aggregate forming red clots and the liquid all around becomes serum. Blood coagulation is a complex mechanism whose alteration can produce diseases such as thrombosis, embolisms and hemorrhages. In particular, thrombosis is one of the major causes of death and implicates a series of morphological and functional changes occurring in different temporal and spatial dimensional scales [1]. Platelets play a central hemostatic role, since, once activated, they rapidly adhere to a damaged substrate and aggregate forming thrombi [2, 3].

Impedance biosensor for the real-time thrombotic profile monitoring and prediction under flow

The advances in technologies and computational methods have moved the cell biology toward a quantitative view [4, 5]. Nowadays, there is an increasing interest for the *in vitro* measurement of coagulation process [6, 7] in order to determine, as quickly as possible, the risk of thrombosis or bleeding, especially during a surgical treatment. On the other hand, moving the attention toward diagnostics, it is becoming essential to evaluate thrombus formation under flow conditions [8–14] to monitor and control the individual thrombotic process in humans, with the goal of development of innovative screening platforms for personalized pharmacological treatments. The improvements in microscope technologies and computational techniques now make possible to investigate platelets functionality and thrombus formation [4, 15]. If the specific aim is to measure the volumetric structure of an object, confocal microscope provides as output a sequence of fluorescent images, called z-stack, acquired along the vertical axial z-dimension, that should facilitate the three-dimensional (3D) volume reconstruction and measurement, rejecting the out-of-focus fluorescence light. The accuracy and the standardization of thrombus volume measurements, starting from confocal microscope images, have always been open and problematic issues especially in the specific biological field of blood coagulation. However, the image acquisition and post process from confocal microscope represents a costly and laborious methodology and, for these reasons, its

application in clinics is still restricted.

In recent years, medical research has gradually oriented its attention to new non-invasive and real-time devices able to assess the thrombotic risk profile reproducing the dynamic conditions of the process. A preliminary electrical characterization of thrombus formation in microchannels under blood flow conditions using electrical impedance spectroscopy [16] has been presented in [17] by using an impedance meter and a low cost sensor based on copper printed circuit board technology and recently improved, as reported in [17–23].

New algorithm for the accuracy improvement in volumes estimation from confocal microscope images

Live cells microscopy has become essential to analyze and reconstruct the intra- and inter-cellular dynamic processes. Numerical computation offers to medicine the beneficial possibility of quantifying and assessing a broad variety of diseases and medical conditions through innovative automated methods of image analysis [24–27]. In the attempt to measure cellular functions and morphological features, samples can be studied by using various microscopy techniques [28], but digital fluorescent images show misrepresented objects, because they are modified and transformed by the acquisition system. Therefore, also the advanced technology of confocal microscopes hides limits, often difficult to be clearly identified and adjusted, that tend to move biologists often far from accurate and realistic measurements [29, 30].

Medical research has gradually moved its attention to new non-invasive and real-time devices with the aim of extracting and monitoring the individual thrombotic risk profile and the whole dynamic of thrombus formation events [7, 17, 18, 20–23, 31–34]. Some of these new technologies use confocal microscope results as references to calibrate their system numerical outputs, but in this specific context standardization and reproducibility still remain open and unsolved issues [15, 35]. In specific scientific literature (e.g. in [36–42]), starting from sequences of confocal images acquired along the axial z-dimension, thrombus volume has been often measured ignoring the presence of an intrinsic inaccuracy and of distortions that have not been compensated. They can be introduced by the optical system because of a convergence lack between marginal and paraxial rays and by the refractive indexes mismatch between the immersion medium and the biological object at their interface. Consequently, spherical aberration phenomena lead to a misrepresentation of the objects and their effects can be shown as an axial elongation in the three-dimensional reconstructions [30, 43–46]. This inaccuracy has never represented a problem because thrombus volume quantification always aimed at the comparison between an untreated situation, called control, and the variation from it due to the effects of biological or pharmacological treatments. In 3D confocal microscopy, systematic errors can arise from distortions of the axial distance, whose accurate calibration remains a challenge. As a result, the 3D reconstructions show a noticeable axial elongation and the volumes are thus

overestimated. A 400-600 % of volume overestimation using available post processing software has been demonstrated.

Impedance biosensor to perform fast quality controls in the pre-analytical phase

Moving the attention towards clinical laboratories, when clinicians make decisions about diagnosis, further investigations or patient management, they rely on the results of blood laboratory analyses. The capability to ensure the reliability and the accuracy of these analyses is, thus, clearly necessary in healthcare to guarantee that the laboratory tests reflect the real patient health state.

A huge quantity of control systems have been developed and they are in use in most clinical laboratories to maintain high levels of quality in the analytical phase [47]. This is not the case for the pre-analytical phase. The majority of laboratory errors are related to this phase, that includes all the processes from the time when a laboratory request is made by a physician until the sample is ready for testing. The magnitude of these errors effects on patient care is not negligible and the focus of health care institutions has become the improvement of laboratory tests quality renewing the interest in pre-analytical processes. Thus, the use of quality controls to prevent laboratory errors should be an essential part of any health care process [48–51]. Unfortunately, despite several methods and systems are currently used in clinic for the preparation of quality control samples [52,53], in practice they depend on the high dimensions of the instruments and of the specific commercial kits whose usage should be optimized.

The most frequent reason for the inadequacy of a sample, as it can cause analytical errors in laboratories, is represented by the hemolysis, that is the rupture of red blood cells with the release of their intracellular content, such as hemoglobin. Free hemoglobin causes interferences in many dosage methods and colorimetric analysis and makes serum samples unsuitable for analysis. Another inadequate sample is represented by the serum containing minute white clots, that can be intended as clots without red cells and made by a polymeric net called fibrin forming during the coagulation of blood. Also a very little presence of hemolysis or white clots is sufficient to lead to technical problems and measurement interferences [54]. Nevertheless, the quality of serum in the pre-analytical phase is usually measured only for the samples that visibly show pale red hemolytic shades, while it should be rapidly and always tested for every sample, without exclusions, in order to assure the complete accuracy of laboratory analyses.

In addition, for blood collected from both healthy donors and patients, a quality control of every sample before laboratory analyses or before transfusions is not always provided. Consequently, the identification of inadequacies and the prevention of measurement errors are not guaranteed. Anomalies involving the temperature of the containers for the transport and the storage

of blood are frequent and common and can lead to variations of blood consistency and also to its undesired coagulation or hemolysis. These problems should be identified and monitored with additional investigations to preserve the samples adequately and to rapidly identify an opportune corrective action. Accordingly, the changes of the hematocrit value, defined as the volume of red blood cells as a percentage of the whole blood volume, could represent an useful indicator reflecting the transport and storage conditions. Thus, the quality of blood samples should be always quantified in a fast way to guarantee the complete compatibility and efficiency in transfusion procedures and to avoid anomalies and errors in laboratory analyses.

Software development for live cells imaging

Fluorescence microscopy, as experimental approach to the direct observation of biological processes in living cells, has received a powerful impulse in recent years thanks to different factors as technological progress of survey instruments and development of specific probes to mark and follow cellular structures or functional parameters in real-time dynamic experiments [55]. In particular, with the development of confocal microscopy, live cells imaging has become increasingly complex. The availability of probes able to mark both living cell and subcellular elements like organelles, proteins and nuclei, or those able to measure important cellular parameters has a central role in the analysis of fluorescence digital images. In particular, one important quantity to be measured is represented by the calcium ion concentration [Ca2+] [56, 57], an intracellular messenger crucial for many biological processes [58, 59]. Calcium ions are released into the cytoplasm from intracellular stores or they enter from the extracellular space, in this case driven by a large electrochemical gradient across the plasma membrane. That is the reason why calcium plays a crucial role in many differ cellular process and its pathway represents a key index for cell life. Calcium is involved in cells excitability, exocytosis, motility, apoptosis, cell-cell interactions and also genes transcription. Unfortunately, the variety in cell types studied, in different biological mechanisms investigated and in different experimental conditions have led to the development of many analytical systems often associated with the instruments used for the acquisition of individual images or associated to the payment of a license to use the software [60–63].

A topic of our laboratory is the study of the dynamic mechanisms that regulate calcium signaling, using different fluorescent probes in different cell types, such as megakaryocytes, platelets, mesenchymal cells, exosomes [38,64,65]. For example it is noticeable that megakaryocytes, that are the platelets precursors, in particular experimental conditions, show a calcium mobilization from intracellular stores. This phenomenon represents the basis of a signal cascades activation that causes megakaryocyte adhesion, starts pro-platelet formation and platelets release and promotes extracellular calcium entry, which is largely involved in the regulation of the contractile force related to megakaryocyte

motility [65]. Also megakaryocytes products are dependent on calcium signals. In platelets, calcium is a substance crucial for their adhesion, activation and aggregation and it can lead to the activation of factors which could disempower the platelets functionality [66]. Calcium plays an important role also in cell differentiation. Bone marrow-derived mesenchymal stem cells can be differentiated into myocytes, as well as adipocytes, chondrocytes and osteocytes in culture, depending on the signals received. The capability of a cell to receive and transmit a signal of calcium represents a key factor for a cell also to become contractile. This is guaranteed by the expression of calcium channels that mediate contraction and that are essential for the muscle functionality [67].

The significant developments in research, through the use of very specific fluorescent probes and new detailed and precise acquisition systems, has greatly contributed to significant advancement in studying biological systems *in vitro*. Commercially, there are many image analysis systems using software specific for the different cell types. Some of them analyze the calcium signal as a global phenomenon quantifying and monitoring its temporal variations and providing global and individual calcium fluorescence intensity profiles [60]. Others focus on segmentation and time series extraction through specific control algorithms [62, 63]. There are also software able to analyze single-cell signals in large cell populations measuring their fluorescence intensity over time [61].

1.1 Aims and results of the thesis

Impedance biosensor for the real-time thrombotic profile monitoring and prediction under flow

The thesis further explores the relevance of blood impedance technique in measuring thrombus formation under flow conditions. First of all, a new biosensor is presented, cheaper than the confocal microscope, capable to characterize, with a non-invasive and real-time impedance analysis, the dynamic of platelet adhesion, aggregation and thrombus formation. A novel, fast and adaptive method is described to quantify volumes from confocal microscope images with more accuracy and standardization, thus providing a reference for the new device calibration and validation. From impedance measurements, it was possible to reconstruct the spatial and temporal distribution of thrombi using a specifically developed analysis tool based on a finite elements approach [18, 19, 22]. Volume measurements thus obtained highly matched volumes reconstructed from confocal microscope images acquisitions. In addition, the new device revealed to be capable of discriminating different hemostatic conditions and of identifying weakening and detaching aggregates, as demonstrated by the results here presented.

New algorithm for the accuracy improvement in volumes estimation from confocal microscope images

The accuracy of quantitative measurements represents an essential pre-requisite to characterize and define the complex dynamic phenomena occurring in the field of cell biology. In research projects that involve the induction of blood coagulation under flow in microfluidic artificial channels, thrombus volume revealed an important quantity to be estimated as a significant index related to the individual thrombotic risk profile. For its importance in the early diagnosis of cardiovascular diseases, the estimated thrombus volume should reflect and represent the reality. According to this necessity, a new easy-to-use and automatic calibration procedure is presented and described for this specific microfluidic and optical context. The adaptive algorithm proposed leads to the automatic compensation of the elongation error and to the accurate thrombus volume measurement. The method has been calibrated using fluorescent beads of known volume, then validated with groups of few distinct platelets and finally applied on platelet thrombi.

Impedance biosensor to perform fast quality controls in the pre-analytical phase

As already stated, electrical measurements represent a highly promising tool for analyzing blood and the relevance of impedance measurement technique in characterizing biomedical human aspects has been already proposed in literature [6, 68]. With regard to the characterization of single blood components, this is still an open challenge, not yet settled by a single multi-measurement sensor. Here, in addition to the biosensor proposed for the thrombi formation monitoring under flow, another new simple impedance-based sensor is presented. Comparing and combining the data obtained from impedance measurements, this technique has been applied to characterize and discriminate different blood components and to perform fast and accurate controls to test the quality of blood and serum samples, with the possibility to confirm or reject their usability in clinics.

Software development for live cells imaging

Finally, in order to optimize the analysis of digital images, a new easy-to-use and user-friendly graphical user interface (GUI) was developed. The software is named FluoLab and works on acquired confocal fluorescence microscopy images. With FluoLab, biologists and physicians are able to obtain, from different types of cells and from hierarchically different spatial regions, quantitative and qualitative data related to cells functionality, such as concentration of calcium ion $[Ca^{2+}]$, thus understanding how they regulate the cells behavior and metabolism. This software differs from the other ones and showing more versatility, more visual immediacy in results and more quickness in obtain-

ing signals. The processing time to analyze images reduced, respect to the traditional approaches used in our laboratory, from days to hours.

1.2 Structure of the thesis

The thesis is organized as follows. In chapter 2 some useful and basic concepts regarding the blood coagulation and the platelets role in the processes involved will be introduced. In chapter 3 the principles of the impedance spectroscopy will be described exploring the fundamental notions about measurement uncertainty and a brief description of the main impedance measurement techniques commonly used. In chapter 4 the field of the live cells imaging, with the description of the principles of the confocal laser scanning microscope, will be provided. Chapter 5 contains the description of the experimental setup and the methodologies implemented and used to perform the experimental activities. In chapter 6 the results and the major outcomes will be illustrated, from the biosensor for the evaluation of the thrombotic profile and the prediction of the related thrombotic risk, to the algorithm for the accuracy improvement in thrombus volume evaluation, from another biosensor for the assessment of the quality of blood components and their characterization, to the software developed for cells signals extraction and analysis. Finally, in chapter 7 conclusions will be drawn and defined.

2. Blood coagulation

2.1 Blood

Blood is a specialized body fluid consisting of 45 % blood cells and 55 % of a protein-rich fluid called plasma. Whole blood can be separated into four main components: plasma, red blood cells, white blood cells and platelets [69], as illustrated in the Figure 2.1.

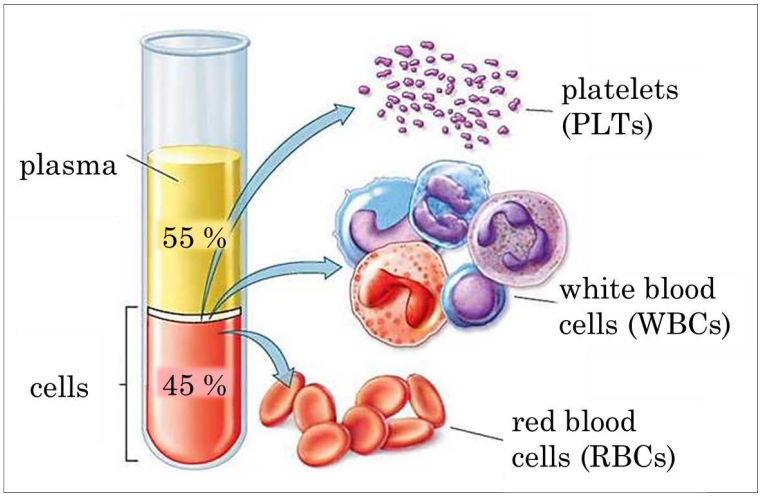

Figure 2.1: ***Blood composition.*** *Blood consists of the liquid plasma, a medium for the transport of materials in the blood, in which cells are suspended. The other elements of which the blood is formed are red blood cells, white blood cells and platelets.*

2.1.1 Cellular components

Plasma

Plasma is the liquid component of blood and it is a mixture of water, sugar, fat, protein, and salts. The main function of the plasma is to transport blood cells throughout the body along with nutrients, waste products, antibodies, clotting proteins, chemical messengers such as hormones and proteins that help maintain the body fluid balance [70].

Red blood cells (RBCs)

Red blood cells (RBCs), also named as erythrocytes, are known for their bright red color and represent the most abundant cell in the blood (4.2-6.1 x 10^9/mL), accounting for about 40 % to 45 % of its volume. The shape of a RBC is a biconcave disk with a flattened center. Production of red blood cells is controlled by the erythropoietin, an hormone produced primarily by the kidneys. Red blood cells start as immature cells in the bone marrow and, after approximately seven days of maturation, are released into the bloodstream. They contain a special protein called hemoglobin, which helps carry the oxygen from the lungs to the rest of the body and then returns carbon dioxide from the body to the lungs so it can be exhaled. The percentage of RBCs in whole blood volume is called hematocrit (HCT) and is a common measure of red cells level. Due to their discoid shape, deformability, intrinsic viscoelastic properties and fibrinogen-binding ability, RBCs are the primary determinants of blood viscosity [71].

White blood cells (WBCs)

White blood bells (WBCs), also known as leukocytes, protect the body from infections. They are much fewer in number than red blood cells, accounting for about 1 % of blood volume. The most common type of white cell is represented by the neutrophils, which are the immediate-response cells and account for 55-70 % of the total WBCs count. Each neutrophil lives less than a day, so the bone marrow must constantly generate new neutrophils to maintain the protection against infections. The other major type of white blood cell is represented by the lymphocytes. There are two main populations of these cells. On one hand, T lymphocytes help in regulating the function of other immune cells and directly attack various infected cells and some tumors. On the other hand, B lymphocytes produce antibodies, which are proteins that specifically target bacteria, viruses and other foreign materials.

Platelets (PLTs)

Platelets (PLTs) are anuclear blood cells that have a discoid shape when circulating in their inactivated state. Also called thrombocytes, they have a diameter of approximately 2–3 μm, a thickness of 0.75 μm and a number density of 200–400 x $10^3/\mu$l. Platelets help the blood clotting process, or coagulation, by gathering at the site of an injury, sticking to the lining of the injured blood vessel and forming a platform on which blood coagulation can occur. This results in the formation of a fibrin clot, which covers the wound and prevents blood from leaking out. Fibrin, a polymeric net, also forms the initial scaffolding upon which new tissue forms, thus promoting healing.

A complete blood count (CBC) test related to a blood sample gives important information about cells types and numbers contained in it, especially

about the red blood cells and their percentage, that is the hematocrit, or the protein content, related to the hemoglobin and then the white blood cells and platelets. The results of a CBC may diagnose conditions like anemia, infections and other disorders. The platelet count and plasma clotting tests may be used to evaluate bleeding and clotting disorders. In particular these tests are the prothrombin time, the partial thromboplastin time and the thrombin time. In addition, it is possible perform a blood smear, which is a way of looking at blood cells under the microscope. Accordingly, in a normal blood smear, red blood cells will appear as regular, round cells with a pale center. Variations in the size or shape of these cells may suggest a blood disorder.

2.1.2 Blood functions

Blood has many different functions that are central to survival, including:

- transport of oxygen to cells and tissues;
- supply of essential nutrients to cells, such as amino acids, fatty acids and glucose;
- removal of waste products, such as carbon dioxide, urea, and lactic acid to the kidneys and liver, which filter and clean the blood;
- protection of the body from infections and foreign bodies through the white blood cells;
- formation of blood clots to prevent an excess of blood loss;
- transport of hormones from one part of the body to other ones, transmitting messages and completing important processes;
- regulation of acidity levels (pH) and of body temperature;
- protective action against diseases through the carriage of cells and antibodies that fight infections.

2.2 Platelet physiology

The fundamental role of platelets in the physiological hemostasis and in the pathological thrombosis relies on their capability of adhesion to specific locations of the perturbed vessel wall upon an injury, a damage or during an inflammation process.

2.2.1 Adhesion

Continued adhesion of flowing platelets leads to building up a platelet plug or thrombus and this is required to arrest bleeding or, under pathological conditions, to induce thrombosis, for instance after the rupture of an atherosclerotic plaque. Platelet adhesion and aggregation occur over the full range of physiological shear rates, thus from 50 s^{-1} to 1800 s^{-1}, and at much higher shear rates, up to 20.000 s^{-1}, that occur under pathological situations. The adhesive properties of PLTs support their attachment to extracellular matrix (ECM) proteins, collagen and von Willebrand factor (VWF). At venous shear rates, so < 200 s^{-1}, the bonds between the glycoprotein GP_{VI} receptors and collagen form and trigger the activation of integrin receptors $\alpha_2\beta_1$ and $\alpha_{IIb}\beta_3$ sufficiently fast. In this way the platelets are brought to rest and firmly adhere to the surface. Bonds between the GP_{Ib} receptors and the adsorbed vWF may play a role at these shear rates but they are not essential. GP_{Ib}-vWF bonds become increasingly important at shear rates found in arteries and arterioles, so $>$ 500 s^{-1} and between 1000 s^{-1} and 1800 s^{-1}, respectively. Thus, a repertoire of receptors and surface-bound ligands, acting synergistically, is required to achieve the adhesion over the range of flow conditions in the blood circulation (Figure 2.2).

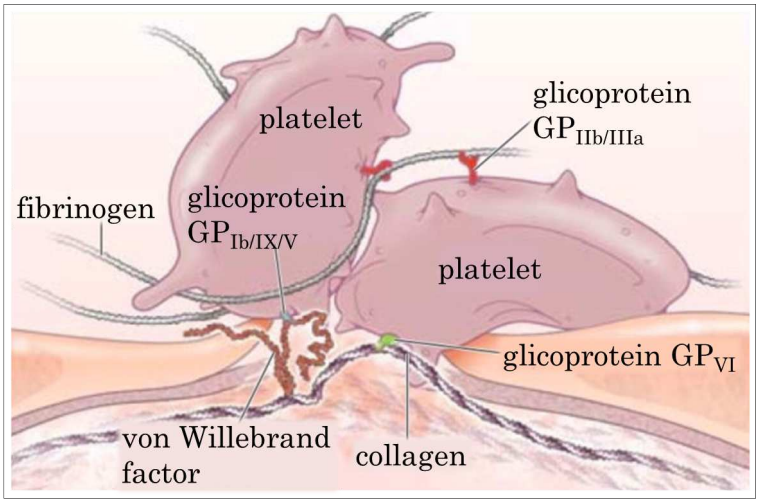

Figure 2.2: ***Platelets adhesion.*** *The adhesive properties of PLTs support their attachment to extracellular matrix proteins, collagen and VWF. In order to immediately respond, platelets express a wide variety of integrin receptors and glycoproteins that engage context-specific ligands in different flow regimens (low or high shear rate).*

2.2.2 Activation and aggregation

Adherent platelets can rapidly recruit to the site of injury additional platelets necessary to achieve the hemostasis, or different types of leukocytes, which set

off host defense responses. Such selective recruitment is orchestrated by the activation pathways stimulated by the initial adhesive interactions and by the soluble agonists released or locally generated, which lead to the appearance on the platelet membrane of different molecules capable of attracting distinct circulating cells.

Platelets activation consists of a number of diverse responses [72]. Fist of all the platelets cytoskeleton reorganizes to extend pseudopodial appendages that help it to spread out on the surface, to become more firmly attached provide a lower profile that reduces drag force. Then, the platelets $\alpha_2\beta_1$ and $\alpha_{\mathrm{IIb}}\beta_3$ receptors become activated and mediatea a firm adhesion and spreading on the vascular surface. The $\alpha_{\mathrm{IIb}}\beta_3$ receptors also enable a platelet-platelet binding. Afterwards, the lipid phosphatidylserine becomes exposed on the platelets surface, allowing them to support the coagulation reactions. Finally, platelets secrete chemicals into the blood plasma. These chemicals provide a way to activate other platelets without their having to directly contact the injured vessel wall and allow the activation process to be propagated away from the wall [73, 74]. Platelet activation is not an all-or-nothing process. Some activation triggers cause only some of these responses to occur. There is a significant evidence that different stimuli, such as collagen, adenosine diphosphate (ADP) and thrombin, can act synergistically to promote a strong activation response [75]. After that, different collagens are present in wall vessel, among which the type I, III and VI are known to support platelet adhesion and aggregation [76].

In addition to their roles in hemostasis and thrombosis, it is known that platelets have been increasingly recognized as multipurpose cells. Indeed, circulating platelets have the ability to influence a wide range of seemingly unrelated pathophysiologic events. The platelets involvement in the interplay between hemostasis, thrombosis, inflammation and cancer is likely complex, yet extremely important in each disease process [77]. For example, thromboembolic complications represent a condition of significant clinical relevance in cancer patients. In particular, venous thromboembolism (VTE) is one of the most important causes of morbidity and mortality in cancer patients. Platelets, by their nature, adhere and are activated in the areas of vascular, inflammatory and neoangiogenesis lesions. Here, the increase in the concentration of cytosolic calcium concentration $[Ca^{2+}]$ is necessary to allow the cell to interact with the microenvironment. Moreover, it is known that the platelets secrete the content of their granules, especially ADP, ATP and serotonin, with a consequent amplification of the activation signals. On the other hand, primary tumors produce many substances that stimulate angiogenesis and can enter in the circulation. Platelets can recognize and respond to circulating tumor products and initiate the coagulation cascade in the absence of intact cells. The system is challenged further as extracellular matrix is exposed during tumor cell invasion or as circulating cancer cells interact directly with platelets. As platelets fulfill their normal hemostatic function in the presence of cancer, they

tend to initiate thrombotic events that can facilitate cancer progression [78].

2.2.3 Thrombus formation and coagulation

Vascular damage-induced exposure of subendothelial tissue factor (TF) generates trace amounts of thrombin with multiple effects on other coagulation factors and platelets. Through multiple enforcement loops in the coagulation system and in platelets activation, phase called primary hemostasis, large amounts of polymeric fibrin are formed stabilizing earlier formed platelets thrombi. In details, fibrin strands form an insoluble mesh of fibres that trap blood cells at the site of damage. This phase is known as secondary hemostasis.

The process by which blood clots are formed involves a complex set of reactions collectively called the coagulation cascade, represented in the Figure 2.3. This cascade is stimulated by clotting factors released from damaged cells or platelets, thus acquiring the names of extrinsic and intrinsic pathway, respectively. The coagulation process involves many intermediary steps, however the

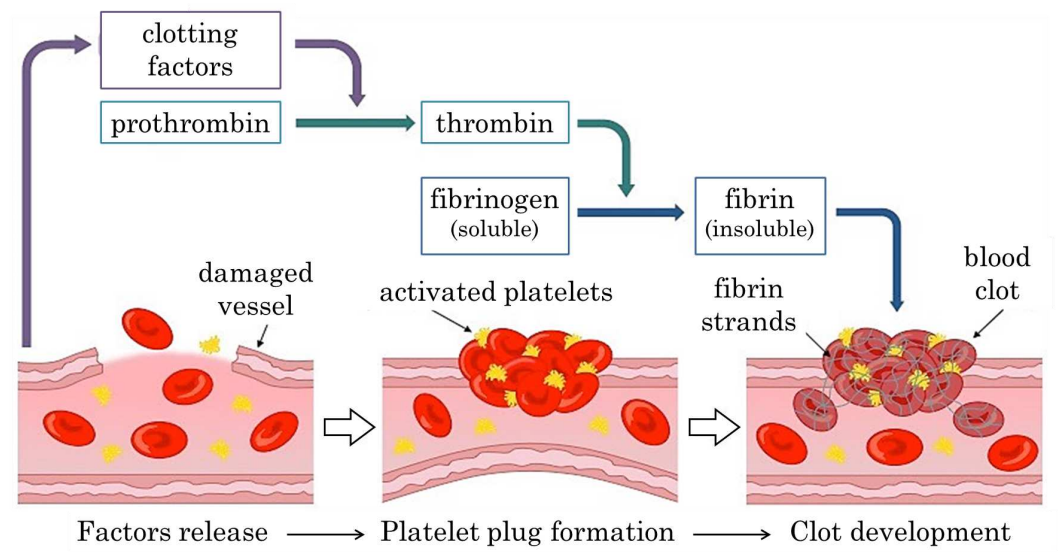

Figure 2.3: ***Coagulation cascade.*** *Injury to vessel lining triggers the release of clotting factors. Then vasoconstriction limits blood floe and platelets form a sticky plug. Finally, fibrin strands adhere to the plug to form an insoluble clot.*

principal events are those immediately introduced. An initial localised vasoconstriction reduces the blood flow through the damaged region and clotting factors lead platelets to become sticky and to adhere to the damaged region forming a solid plug. Additionally, clotting factors trigger the conversion of the inactive zymogen prothrombin into the activated enzyme thrombin that in turn catalyses the conversion of the soluble plasma protein fibrinogen into its insolube fibrous form called fibrin. The fibrin strands, as already described, form a mesh of fibres around the platelet plug and traps blood cells to form a

temporary clot. When the damaged region is completely repaired, an enzyme called plasmin is activated to dissolve the clot [79].

2.3 Coagulation models

Platelet deposition and coagulation occur in the presence of moving blood and are strongly affected by fluid dynamics in ways that are only partially understood. One indication of flow influence is that clots that form in veins, where blood flow is slower, are made mainly of fibrin gel and trapped RBCs, whereas clots that form in arteries, where blood flow is faster, are mainly made of platelets. Elucidating the mechanisms by which fluid dynamics influences clot formation and stability is the aim of a growing level of experimental activity using microfluidic chambers and of theoretical modeling and simulation using the tools of computational fluid dynamics [15, 31, 80]. Mathematical modeling and computer simulation of clotting are essential to understand how the clotting system as a whole, or even major pieces of it, functions as an integrated dynamical system. Yet modeling of platelet adhesion, aggregation and coagulation presents enormous challenges both in formulating models and in studying them computationally. To look at thrombus development beyond initial adhesion, one must account for the disturbance to the flow that the growing thrombus generates. Hence, models of thrombus growth involve, at a minimum, a coupled problem of fluid dynamics, transport of cells and chemicals, platelet activation, adhesion and cohesion mechanics, and growth of a fluid-perturbing platelet mass. These processes involve spatial scales ranging from millimeters to nanometers and timescales, from minutes to milliseconds. Exploiting the biochemical and physiological characteristics of platelets and megakaryocytes, the platelets precursors, it is possible to hypothesize their use both in supportive therapies, for example in cases of thrombocytopenia following high-dose chemotherapy treatments, and as vehicles for tumor transport of substances with therapeutic efficacy. Fast and accurate monitoring of the single thrombotic risk represents a diagnostic challenge in the cardiovascular field and in the treatment of relevant clinical problems in the hematological, onco-hematological and oncological fields.

3. Impedance spectroscopy (IS)

3.1 Theory and background

3.1.1 Fundamentals

Impedance spectroscopy (IS) represents a relatively new and powerful method to characterize the electrochemical behavior and properties of materials [16]. In particular, is nowadays established as a powerful tool for the investigation of mechanisms involved in the electrochemical reactions, for measuring dielectric and transport properties of materials and for the study of surfaces and electrode-material interfaces. This various and multifaceted context force the abandon of the simple concept of resistance using, in its place, the more generalize concept of impedance. The term impedance was introduced by Oliver Heaviside in 1886 and soon after Arthur Kennelly was the first to represent impedance with complex numbers. It is a complex quantity and it can be defined as the frequency dependent resistance to current flow of a circuit element or groups of elements. In addition to resistances of direct current (DC) circuits, impedance in alternating current (AC) circuits permits to include inductances and capacitances, that are the effects of the induction of voltages in conductors by the magnetic fields and the electrostatic storage of charge induced by voltages between conductors, respectively. The impedance caused by these two different effects is named reactance, indicated with the letter X and representing the imaginary part of impedance, whereas resistance, indicated as R, forms the real part. Applying an electrical stimulus to a couple of electrodes, several microscopic processes occur in the material under study and they lead to a global electrical response. These processes consist of transport of electrons through electronic conductors, transfer of electrons at the interfaces and flows of charged atoms. The electrical current, that is the flow rate of charged particles, thus depends on the resistance of electrodes and materials and on the reactions at their interfaces. Hence, any intrinsic property influencing the conductivity of an electrode-material system can be studied by IS. In particular, the parameters obtained from impedance measurements can belong to those related only to the material itself or to those pertinent to the electrode-material interface.

Ohm's law generally defines the resistance R, in terms of ratio between the voltage V, measured in volt [V] and the current I, measured in Ampere [A],

as

$$R = \frac{V}{I} \tag{3.1}$$

Resistance is expressed in ohm [Ω]. This is a well-known equation, but its use is limited to only linear systems, in which the ratio V/I remains constant, regardless of the voltage and current applied. Unfortunately, electrochemical and biological systems generally do not show a linear voltage-current characteristics. In particular, both solid and liquid electrochemical systems tend to exhibit a strong non-linear behavior, especially at the interfaces, due to the presence of impurities, the growth of oxide layers, the coating degradations, the temperature changes. However, since any continuous, differentiable function can be considered linear for reasonably small input perturbation amplitudes, also real systems under study can be approximated as pseudo-linear. This means that if the input consists of the weighted sum of several signals then the output is simply the superposition, as a weighted sum, of the responses of the system to each of the signals. Nevertheless, the between the properties of a system and its response to a periodic input voltage is very challenging in the time domain. In general, the solution of several differential equations is required, but the equations system is often too much intricate to be solved in the time domain. The Fourier Transform (FT) allows a significant simplification of the mathematical treatment of the problem, reducing it to an algebraic one. FT takes time domain sinusoidal data and generates the equivalent frequency domain data. IS is based on the application of a small sinusoidal perturbation of fixed frequency, commonly a known voltage, to the system and on the measurement of the electrical response, the resulting related current. Repeating the measurements for a wide range of frequencies, the whole response of the system, known as impedance spectrum, can be analyzed and represented in the frequency domain. The impedance values are thus derived by FT from the time domain and it is defined for a set of individual frequencies.

Electrical impedance is usually measured exciting the system with a small signal in order to obtain a pseudo-linear response. In particular, during an IS measurement, the small signal sinusoidal voltage $v(t) = V_0 \sin(\omega t + \phi_v)$, with amplitude V_0, at the frequency $f = \omega/2\pi$ [Hz], where ω is the angular or radial frequency [rad/s], is applied to the system under study. The resulting current $i(t) = I_0 \sin(\omega t + \phi_i)$ is measured at the same frequency, showing an amplitude of I_0, as illustrated in Figure 3.1. Here $\theta = \phi_v - \phi_i$ is the phase difference between voltage and current, expressed in degrees [deg] or radiants [rad] and equal to zero only for purely resistive behavior. The shift appears because, in linear or pseudo-linear systems, the response to a small periodic excitation is a sinusoidal wave at the same frequency, but with different amplitude and shifted in phase (Figure 3.1). An expression analogous to the Ohm's law (Equation 3.1) allows to calculate ratio between voltage and current as

$$\frac{v(t)}{i(t)} = \frac{V_0 \sin(\omega t + \phi_v)}{I_0 \sin(\omega t + \phi_i)} \tag{3.2}$$

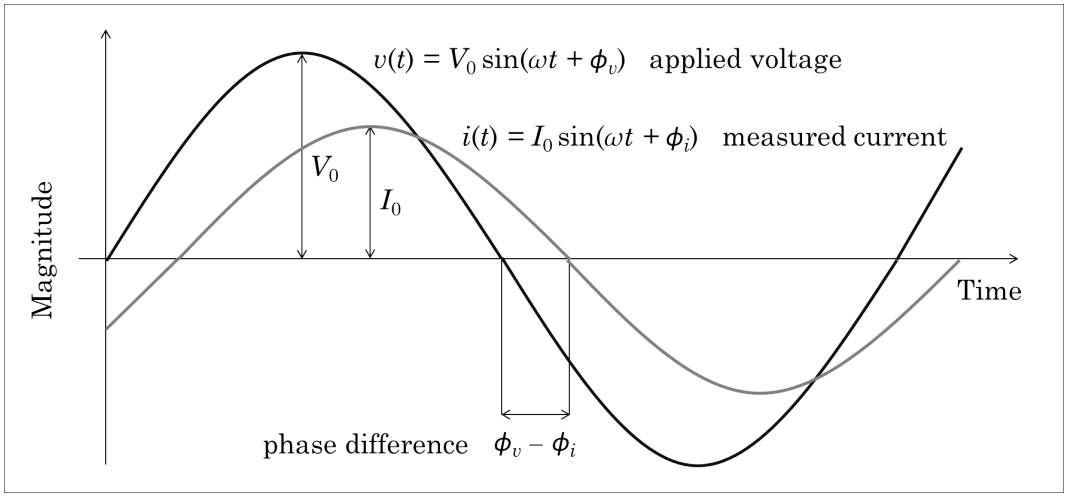

Figure 3.1: ***Voltage*** $v(t)$ ***and current*** $i(t)$ ***signals in IS experiments.*** *A sinusoidal voltage* $v(t) = V_0 \sin(\omega t + \phi_v)$*, with amplitude* V_0*, is applied to the system under study. The resulting current* $i(t) = I_0 \sin(\omega t + \phi_i)$ *shows the amplitude* I_0*. In linear or pseudo-linear systems, the response to a small periodic excitation is a sinusoidal wave at the same frequency, but with different amplitude and shifted in phase. The phase difference between voltage and current is defined as* $\theta = \phi_v - \phi_i$*.*

where the ratio V_0/I_0 acts just like a resistance [Ω]. To semplify calculations, sinusoidal voltage and current are commonly represented in the frequency domain, by exploiting the complex number notation, as $V(\omega) = V_0 e^{j(\omega t + \phi_v)}$ and $I(\omega) = I_0 e^{j(\omega t + \phi_i)}$, respectively, where $j = \sqrt{-1}$ is the imaginary unit. With this notation, the impedance of the system can be expressed rewriting the Equation 3.2 as

$$Z(\omega) = \frac{V(\omega)}{I(\omega)} = \frac{V_0 e^{j(\omega t + \phi_v)}}{I_0 e^{j(\omega t + \phi_i)}} = \frac{V_0}{I_0} e^{j(\phi_v - \phi_i)} = Z_0 e^{j\theta} \tag{3.3}$$

where $\theta = \phi_v - \phi_i$ is the impedance phase angle. An impedance value can thus be considered as the ratio between voltage and current for a single complex exponential at a particular angular frequency ω. In other words, the complex quantity $Z(\omega)$ is defined as the impedance function and its values at particular frequencies represent the impedance of the system under study. The inverse of impedance is named admittance $Y(\omega) = 1/Z(\omega)$ and its magnitude measurement unit is siemens [S]. Because of this Ohm's law-like relation between voltage and current, the whole impedance of a circuit with multiple impedance elements can be quantified with the same rules as with multiple resistors, which greatly semplifies calculations. In addition, just as impedance extends the Ohm's law to cover AC circuits, other results from DC circuit analysis can also be extended to AC circuits, such as voltage division, current division, Thevenin's and Norton's theorems, by replacing resistance with impedance.

It is essential to remember that FT, linear because computed through a

linear integral, helps in reducing differential equations in the time domain to algebraic forms in the frequency domain only under the system conditions of linearity, causality, stability and finiteness. Therefore, impedance is properly defined only for systems satisfying these conditions. The concept of linearity is related, as already said, to the effects superposition principle. Causality means that the response of the system under study has to depend only from the AC input and not from any other external stimulus. Stability means that the system being measured must remain in a stationary state until an external source provide to excite it and it should return to the same state after the perturbation is finished. This implies that throughout the time required to measure impedance the system should not incur in any drift. Finiteness means that impedance values have to be finite over the whole frequency range without divergences towards infinite values. In order to met these criteria, some rules and suggestions can be followed. The amplitude of the AC signals has to be chosen in order to be small enough to maintain the system in a linear condition, but large enough to measure a response. In addition, frequency range and measurement conditions have to be properly chosen in order to have a total tome of measurement fast enough to not incur in long term drift of the system to be analyzed. In order to verify the linearity of the system and the correct choice of the stimulus, it is possible to repeat the impedance measurements by varying the AC amplitude. In this case, if the spectrum does not change the system is linear. On the other hand, if the measurements are instead repeated different times without changing any parameter and the response appears always the same, the system can be considered stable. A graphical method that can be used to assess the reliability of the impedance data is represented by the Lissajous curves (Figure 3.2). Plotting the AC ap-

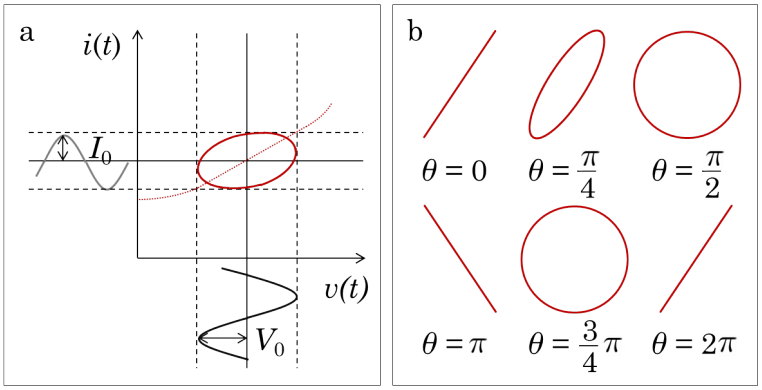

Figure 3.2: ***Lissajous curves.*** *The origin of the curves, obtained plotting the applied voltage $v(t)$ and its response $i(t)$ in an orthogonal system of axes (a). The Lissajous curves allow a visualization of the relation between voltage and current useful to detect any distortion from linearity and reflecting their phase difference θ, here expressed in radiants (b).*

plied sinusoidal voltage $v(t)$ on the horizontal axis and the response $i(t)$ on the

vertical axis, the result is generally an oval, as shown in Figure 3.2a. In particular, the Lissajous curves allow a visualization of the relation between voltage and current that perfectly reflects, as illustrated in Figure 3.2b, their phase shift $\theta = \phi_v - \phi_i$. The analysis of Lissajous curves on oscilloscope screen was the only impedance measurement technique before the availability of modern IS instrumentation, while nowadays maintains its usefulness in detecting any distortion from linearity or the presence of external perturbation.

IS is demonstrated to be a suitable analytical tool in materials research and characterization because it involves a relatively simple electrical measurement that can be automated and whose results may be correlated with many materials variables, such as mass transport, rates of chemical reactions, dielectric properties, defects and microstructures. IS can predict aspects of the performance of sensors and it can be used to investigate membranes behavior in living cells. Impedance measurements are useful also in emprical quality control procedures, contributing to the interpretation of fundamental electrical and chemical processes. A flow diagram of a general characterization procedure using IS is presented in Figure 3.3. Experimentally obtained impedance data for a given electrode-material system may be analyzed by using an exact mathematical model based on a plausible physical theory that predicts theoretical impedance or by a relatively empirical equivalent circuit from which an equivalent impedance can be predicted. In either the case of the mathematical model or of the equivalent circuit, the impedance-related parameters can be estimated and the impedance measurements obtained from IS experiments can be compared to either the predicted theoretical impedance or that associated to the equivalent circuit. The analysis of physical processes often suggests an equivalent circuit and may explain and account adequately for the observed IS response, with the aim of associating each electrical parameters to a specific properties or physical aspect of the system under study until the achievement of its knowledge and characterization.

3.1.2 Impedance representation

The quantitative measurement of the output spectrum of a system in response to a stimulus and its representation and analysis is useful to characterize the system under study and to reveal its internal dynamics. In particular, IS consists in measurements of the magnitude and the phase angle as functions of frequency and their visualization reflect the changes in impedance of the system during the excitation.

Phasors theory

The magnitude and the phase angle of sinusoidal functions of time characterize phasors in the frequency domain representation. A phasor can be imagined as a planar vector rotating in the complex plane and it is described by a constant

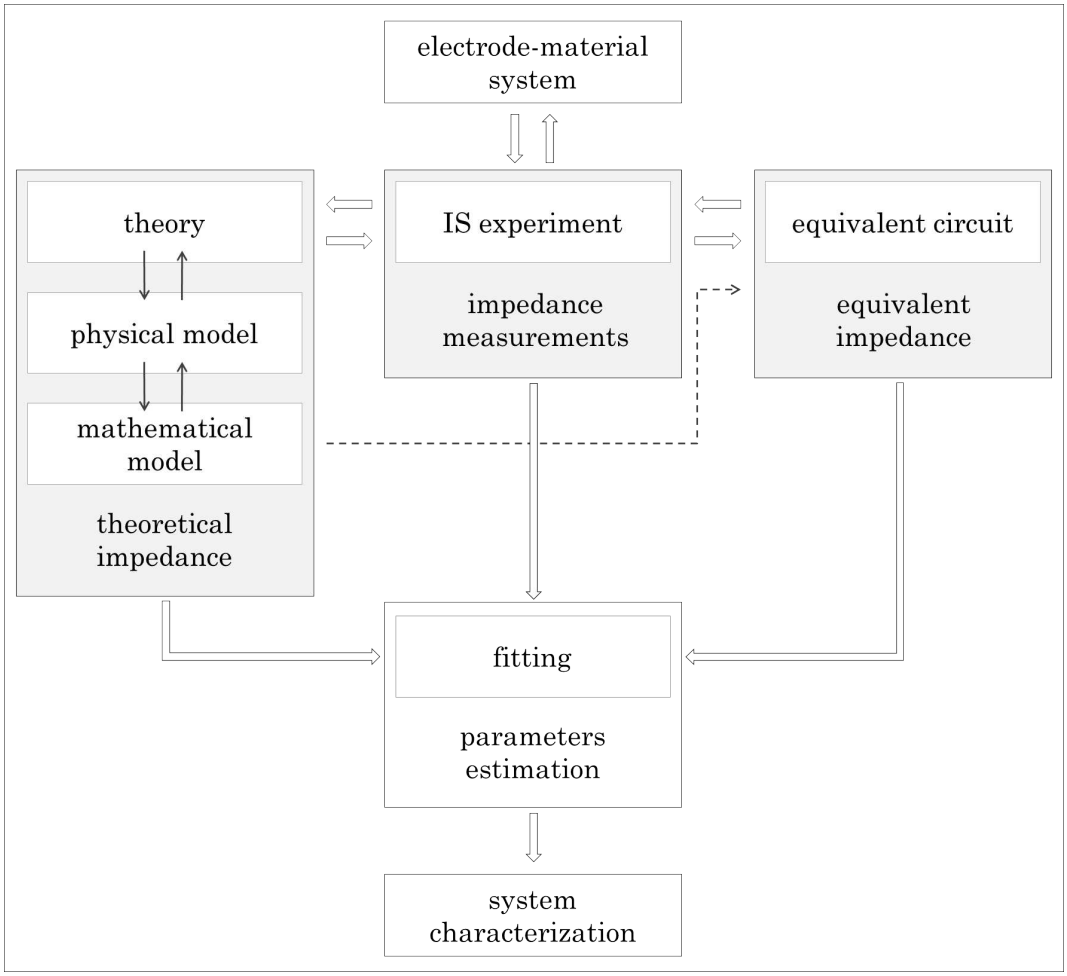

Figure 3.3: ***Impedance spectroscopy (IS) flow diagram.*** *Scheme for the characterization of an electrode-material system with impedance measurements.*

complex number that captures both magnitude and phase characteristics, expressed with $|\cdot|$ and $\angle\cdot$, respectively. Phasors, generally indicated with bold letters, are used by electrical engineers to semplify computations involving sinusoids in linear or pseudo-linear systems because their capability to reduce a differential equation problem in the time domain to an algebraic one in the FT space. The impedance phasor $\bar{Z}$ of a circuit element can be defined as the ratio of the voltage phasor $\bar{V} = |V|e^{j\angle V}$ across the element to the phasor of the current $\bar{I} = |I|e^{j\angle I}$ through the element, with the expression

$$\bar{Z} = \frac{\bar{V}}{\bar{I}} \tag{3.4}$$

The impedance phasor $\bar{Z}$ of a circuit element, can be represented in the polar form or in the rectangular form, as shown in Figure 3.4. Rewriting the Equation 3.4, the polar form conveniently captures both magnitude and phase

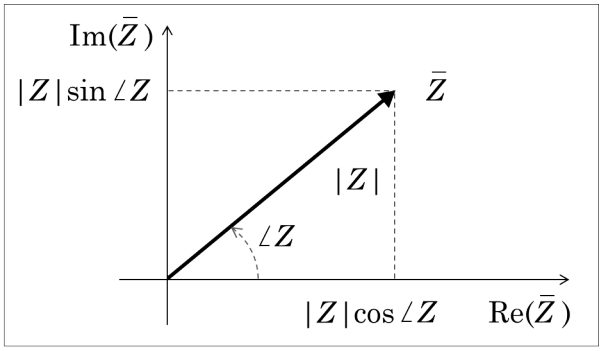

Figure 3.4: ***Impedance phasor representation in the complex plane.*** *The impedance phasor $\bar{Z}$ is a planar vector rotating in the complex plane and it can be represented in the polar form, in terms of magnitude and phase angle or in the rectangular form, in terms of real component along the horizontal axis and imaginary component along the vertical axis.*

characteristics as

$$\bar{Z} = \frac{\bar{V}}{\bar{I}} = \frac{|V|e^{j\angle V}}{|I|e^{j\angle I}} = \frac{|V|}{|I|}e^{j(\angle V - \angle I)} = |Z|e^{j\angle Z} \tag{3.5}$$

In the polar form the magnitude of impedance $|Z|$ is the ratio of the voltage to the current magnitudes and its phase angle $\angle Z$ is the phase shift or difference by which the current lags the voltage. The expression is analogous to the definition obtained from the Ohm's law-like (Equation 3.3). The planar impedance phasor can be represented also in an orthogonal system of axes, by the vector sum of the real and imaginary components along the horizontal axis and the vertical one, that are their rectangular coordinates, by the complex number

$$\bar{Z} = \mathrm{Re}(\bar{Z}) + j\mathrm{Im}(\bar{Z}) = R + jX \tag{3.6}$$

where the real part of impedance, $\mathrm{Re}(\bar{Z})$, is the resistance R, while its imaginary part, $\mathrm{Im}(\bar{Z})$, is the reactance X. The Equations 3.5 and 3.6 can be rearranged and further modified by applying the Euler's relation

$$e^{j\varphi} = \cos\varphi + j\sin\varphi \tag{3.7}$$

thus obtaining

$$\bar{Z} = |Z|e^{j\angle Z} = |Z|(\cos\angle Z + j\sin\angle Z) = |Z|\cos\angle Z + j|Z|\sin\angle Z \tag{3.8}$$

Here the two rectangular coordinates values are clearly $\mathrm{Re}(\bar{Z}) = |Z|\cos\angle Z$ and $\mathrm{Im}(\bar{Z}) = |Z|\sin\angle Z$, as indicated in Figure 3.4. The polar and the rectangular forms are different representations of the same complex quantity and are mathematically equivalent. Where it is needed to add or subtract impedances the rectangular form is more convenient, but when quantities have to be multiplied or divided the calculation becomes simpler if the polar form is used.

Conversions between the forms follows the normal conversion rules of complex numbers and the magnitude and phase angle can be obtained from

$$|Z| = \sqrt{\mathrm{Re}^2(\bar{Z}) + \mathrm{Im}^2(\bar{Z})} \tag{3.9}$$

$$\angle Z = \tan^{-1}\left(\frac{\mathrm{Im}(\bar{Z})}{\mathrm{Re}(\bar{Z})}\right) \tag{3.10}$$

Spectrum visualization

IS is characterized by the measurement and the analysis of impedance-related parameters and the visualization of impedance spectrum can be very helpful in interpreting the small signal AC response of each electrode-material system being investigating. As a complex quantity, impedance expression consists of a real and an imaginary part. Considering the complex plane, where the imaginary part is plotted as function of the real part, impedance measurements can be represented with a Nyquist plot (Figure 3.5). The most common use

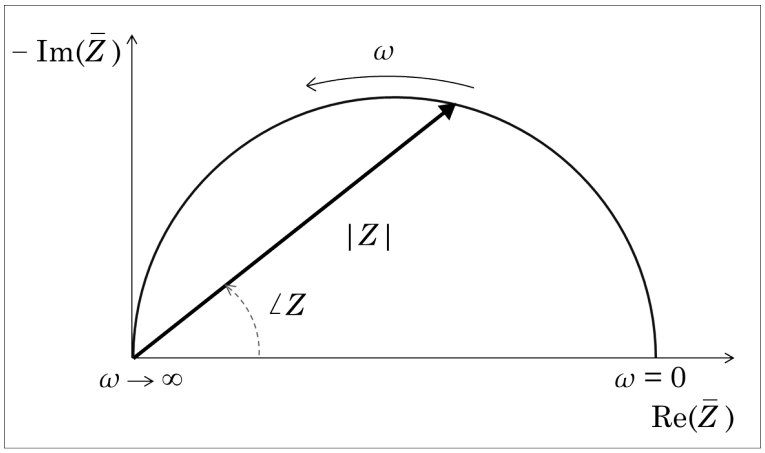

Figure 3.5: ***Nyquist plot.*** *The real part of the impedance is plotted on the horizontal axis while the imaginary part is plotted on the vertical one. Magnitudes and phase angles measured at all the explored frequencies appear simultaneously on a single polar plot, with frequency as parameter, and the points series can be drawn imagining the rotation of the impedance phasor in the complex plane. The negative imaginary axis -Im($\bar{Z}$) is usually represented, instead of the positive Im($\bar{Z}$), because IS generally involves capacitances and rarely inductances, thus ensuring that the vast majority of all curves fall in the first quadrant.*

of Nyquist plot is the assessment of the stability for automatic systems with feedback in controls theory. The real part of the impedance is plotted on the horizontal axis while the imaginary part is plotted on the vertical one. Directly deriving from the phasor representation of Figure 3.4, the Nyquist plot can be described also using the polar representation, where the magnitude is the radial coordinate and the phase is the angular one. As visible in Figure 3.5,

magnitudes and phase angles measured at all the explored frequencies appear simultaneously on a single polar plot, with frequency as parameter. In particular, every point in the Nyquist diagram identifies the impedance value at one specific frequency among all the frequencies chosen for the measurements and the sum of these points allows the visualization of the whole impedance spectrum. The points series can be drawn imagining the rotation of the impedance phasor $\bar{Z}$, defined by its magnitude $|Z|$ and its phase angle $\angle Z$, in the complex plane. The rotation begins at low frequencies, corresponding to the right part of the Nyquist diagram, finishing at high frequencies, represented on the left part of the plot, as indicated in Figure 3.5. Therefore, the diagram has to be read from the right to the left, following the increase of frequency. Even if not essential, it can be a good practice to employ isometric axes in this type of graph, in order to immediately detect the possible presence of non-ideal capacitive behavior, as subsequenlty illustrated. In addition, as visible in Figure 3.5, because IS usually involves capacitances and rarely inductances, it has become common to represent impedances in a complex plane where the vertical axis represents -Im($\bar{Z}$), instead of Im($\bar{Z}$), thus ensuring that the vast majority of all curves fall in the first quadrant.

Another opportunity to visualize the electrical response of the system under study in terms of impedance spectrum is represented by the Bode diagrams (Figure 3.6). They consists in a pair of diagrams reporting the measured magnitudes (Figure 3.6a) and phase angles (Figure 3.6b) on two rectangular plots as explicit function of frequency. Because of the wide range of frequencies and magnitudes usually involved in electrical measurements, Bode diagrams tipically express both frequency and magnitude values in a logarithmic scale with the logarithm to the base 10, where axes are, thus, divided in decades, that are intervals of equal length between a number and that one ten times bigger. The logarithmic representation of angular frequency ω is illustrated in Figure 3.7. To express the network gain $\mathrm{G}(\omega)$ in circuit theory, such as the voltage gain of an amplifier, the gain magnitude is commonly represented in decibel, dB, as $|\mathrm{G}(\omega)|_{\mathrm{dB}} = 20 \log_{10} |\mathrm{G}(\omega)|$, where decibel is not a measurement unit, but a pure number. In this way, a factor of 10 in gain magnitude, leading to a power gain of 100, corresponds to 20 dB and gains of less than 1 have a negative values in decibel scale. Decibel scale is useful in studying the frequency response of amplifiers and filters. On the other hand, in the case of the analysis of general a quantities with their measurement unit, the magnitude is simply expressed in logarithmic scale to the base 10. In general, a logarithmic scale allows a detailed representation of quantities falling in wide ranges of values, as already stated. Therefore, in Bode diagrams related to the impedance spectrum, magnitude can be represented as $|Z|(\omega)$ [Ω] either in linear or logarithmic scale, while the frequency and the phase angles as $\log_{10} f$ [Hz] and $\angle Z(\omega)$ [deg], respectively. In Bode plot frequency is explicit and small impedances in presence of large impedances can be identified easily instead to be swamped. In addition, Bode plots are useful in analyzing complicated functions because the key

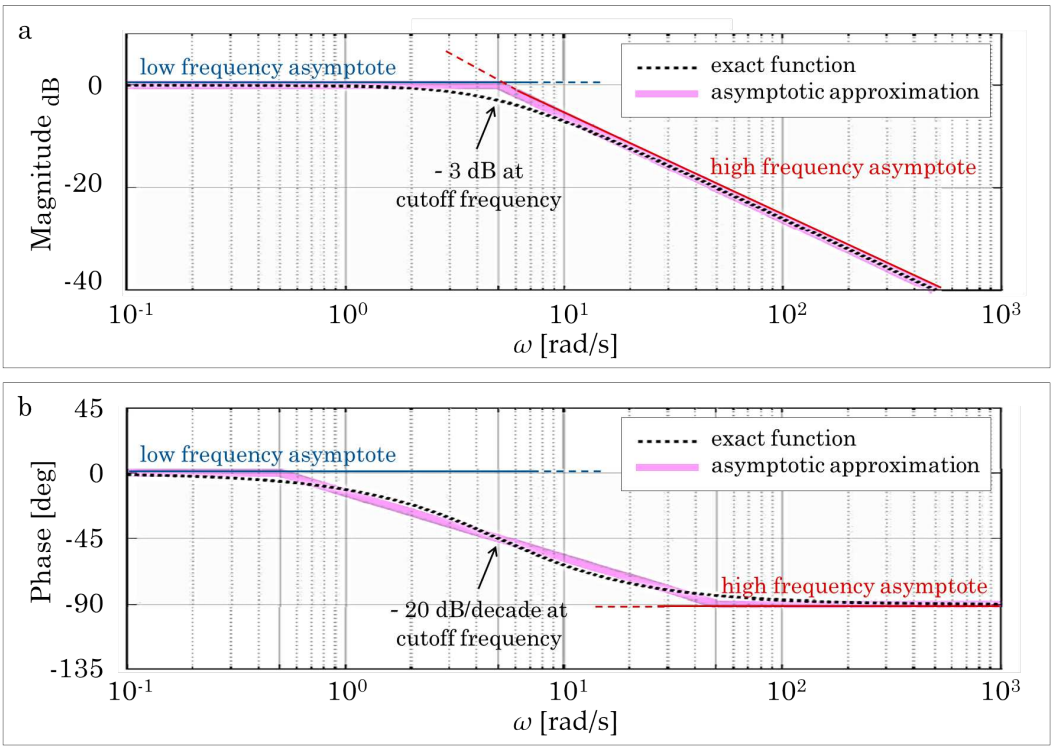

Figure 3.6: ***Bode diagrams.*** *Magnitude diagram (a). Phase diagram (b). For complicated functions, Bode diagrams can be obtained considering the asymptotes at low and at high frequencies and the slope changes at the cutoff frequencies.*

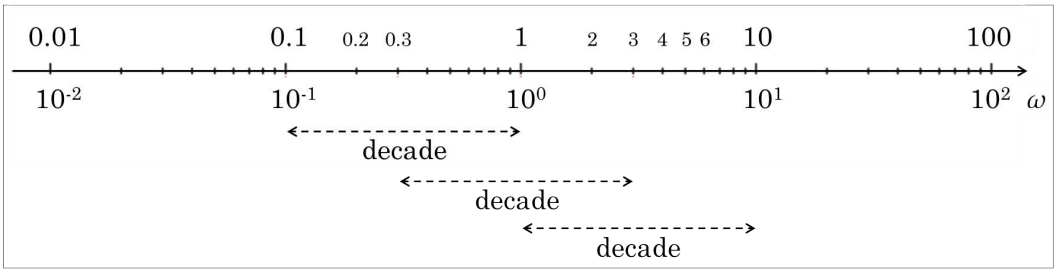

Figure 3.7: ***Logarithmic scale of the angular frequency.*** *The angular frequency ω is reported using the logarithmic scale to the base 10. The logarithmic function is linear in this scale. Decades are intervals of equal length between a number and that one ten times bigger.*

features of the diagrams can be quickly sketched by hand using some simple rules that identify how the circuit elements influence the frequency response of the system. In fact, a system response H can be generically represented in the frequency domain as a rational polynomial function of the Laplace complex variable s

$$\mathrm{H}(s) = \frac{b_m s^m + b_{m-1} s^{m-1} + \ldots + b_1 s + b_0}{a_n s^n + a_{n-1} s^{n-1} + \ldots + a_1 s + a_0} \tag{3.11}$$

where it is often convenient to factor the polynomials in a numerator $\mathrm{N}(s)$

and in a denominator D(s) and to rewrite the Equation 3.11 in terms of these factors

$$\mathrm{H}(s) = \frac{\mathrm{N}(s)}{\mathrm{D}(s)} = K\frac{(s-z_1)(s-z_2)...(s-z_{m-1})(s-z_m)}{(s-p_1)(s-p_2)...(s-p_{n-1})(s-p_n)} \tag{3.12}$$

where the numerator and the denominator, N(s) and D(s), have real coefficients and $K = b_m/a_n$. The values z_1, z, ..., z_{m-1}, z_m of s, that make N(s) = 0, are the roots of the numerator and are known as the zeros of the system. The values p_1, p, ..., p_{n-1}, p_n of s, that satisfy D(s) = 0, are the roots of the denominator and are defined to be the poles of the system. By substituting $j\omega$ by s directly into the factored form, the Equation 3.12 allows to obtain the impedance Z(ω) as

$$\mathrm{Z}(\omega) = \frac{\mathrm{N}(\omega)}{\mathrm{D}(\omega)} = K\frac{(j\omega-z_1)(j\omega-z_2)...(j\omega-z_{m-1})(j\omega-z_m)}{(j\omega-p_1)(j\omega-p_2)...(j\omega-p_{n-1})(j\omega-p_n)} \tag{3.13}$$

Zeros and poles represent properties related to the differential equations describing the system dynamics. From the complex algebra, zeros and poles can be dealt with separately and the results added up to find the impedance magnitude and its phase angle as

$$|Z(\omega)| = K\frac{\prod_{i=1}^{m}(j\omega-z_i)}{\prod_{i=1}^{n}(j\omega-p_i} \tag{3.14}$$

$$\angle Z(\omega) = \sum_{i=1}^{m}\angle(j\omega-z_i) - \sum_{i=1}^{n}\angle(j\omega-p_i) \tag{3.15}$$

The advantage of this approach, especially for complicated functions, consists of the possibility to obtain Bode diagrams combining the elementary diagrams of the individual factors. In addition, by factoring the polynomial representative function as in Equation 3.13 and, thus, identifying the zeros and the poles of the system, the impedance spectrum can also be sketched without drawing the individual component curves. The method is based on the fact that the curves of magnitude and phase undergo a change in slope at each cutoff frequency, coinciding with poles and zeros, considered and arranged in ascending order. In general, as summarily represented in Figure 3.6, when a pole is encountered the magnitude slope always decreases by 20 dB/decade, corresponding to a decrease of a factor of 10, while the phase angle lowers of 90 deg with a negative slope of 45 deg/decade. On the other hand, even if not illustrated, when a zero is encountered the slope always increases by 20 dB/decade, corresponding to a factor of 10, while the phase angle increases of 90 deg with a positive slope of 45 deg/decade. Therefore, at any frequency, the slope of the asymptotic magnitude function depends only on the break points related to lower cutoff frequencies, thus on the values in the left part of the Bode plot. To find a reference level, the limiting behavior at low and high frequencies can be exploited to identify a starting point, from which the

Bode plot can be constructed from straight line segments changing in slope at every zero and pole. Once the asymptotic plot is sketched, a more accurate version can be drawn, as visible for instance in Figure 3.6 where the asymptotic approximation and the exact function are shown. Smoother magnitude curves has to be plotted with an attenuation of $1\sqrt{2}$ or 3 dB below or above each break point (Figure 3.6a), while smoother phase diagrams can be obtained joining the asymptotes with the tangent to the diagram at each cutoff frequency (Figure 3.6b).

3.2 Electrical equivalent circuits for IS data analysis

3.2.1 Electrical circuit elements

With the frequency domain representation and the phasors theory at disposal a system under study can be analyzed and characterized. As already described in Figure 3.3, impedance measurements experimentally obtained may be compared to a theoretical impedance obtained from physical and mathematical models whose aim is the detailed reproduction of physical processes and properties of the system. In practice, IS data are commonly analyzed by fitting to an equivalent circuit model, to simply reproduce the properties of the system without the claim of describe them with inticate mathematical expressions. In this way the electrode-material system can be modeled as a network of circuit elements and the equivalent impedance obtained is compared to the system response.

Resistors, capacitors and inductors

The most common electrical circuit elements are resistors, capacitors and inductors (Figure 3.8). Each of them is equipped with two terminals and is characterized by a current that flows through it and a voltage across it.

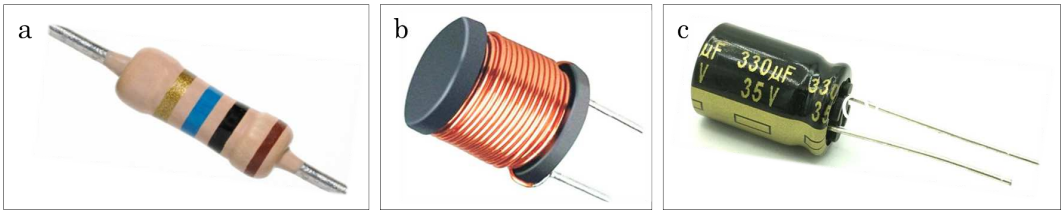

Figure 3.8: ***Common electrical circuit elements.*** *Resistor (a). Inductor (b). Capacitor (c).*

The simplest circuit element is the resistor (Figure 3.8a) whose electrical circuit symbol is represented in Figure 3.9a. For this element, the relation

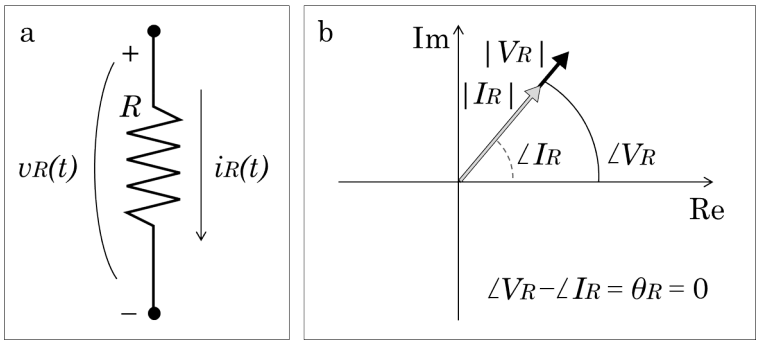

Figure 3.9: ***Resistor.*** *Electrical circuit symbol (a). Phasors representation in the complex plane (b).*

between voltage $v_R(t)$ and current $i_R(t)$ in the time domain is given, according to the Equation 3.1 and the Equation 3.2, by

$$v_R(t) = Ri_R(t) \tag{3.16}$$

where resistance R [Ω] is a real number that represents the fundamental property of the resistor. The resistance of a material strongly depends on its conducibility σ [Sm^{-1}] and on the element geometry. When a sinusoidal voltage is applied to the system, the current response appears perfectly in phase with the excitation. In fact, in order to satisfy the equality $V_0 \sin(\omega t + \phi_v) = RI_0 \sin(\omega t + \phi_i)$, the phase angles ϕ_v and ϕ_i have to coincide, so voltage and current have to be in phase, that is equivalent to $\theta_R = 0$. With the complex notation, the voltage-current relation becomes

$$V_R(\omega) = RI_R(\omega) \tag{3.17}$$

and the resistor impedance $Z_R(\omega)$ simply assumes the expression of a purely real resistance

$$Z_R(\omega) = R \tag{3.18}$$

Figure 3.9b shows the phasors representation in the complex plane of V_R and I_R.

An inductor (Figure 3.8b) is an electrical circuit element that consists of a filiform conductor, wrapped aroud a magnetic core or simply in air, forming a winding of coils. Its electrical symbol is shown in Figure 3.10a. The Ampere's law says that if a current $i_L(t)$ flows through a winding of coils, a proportional magnetic field B, whose measurement unit is tesla [T], is produced and it can be represented with the expression

$$B = \mu_0 \mu_r N i_L(t) \tag{3.19}$$

where N is the number of coils per unit of length [m^{-1}]. The constant term μ_0 represents the magnetic permeability of the vacuum, corresponding to $\mu_0 = 4\pi 10^{-7}$ Tm/A, and μ_r refers to the magnetic permeability of the medium on

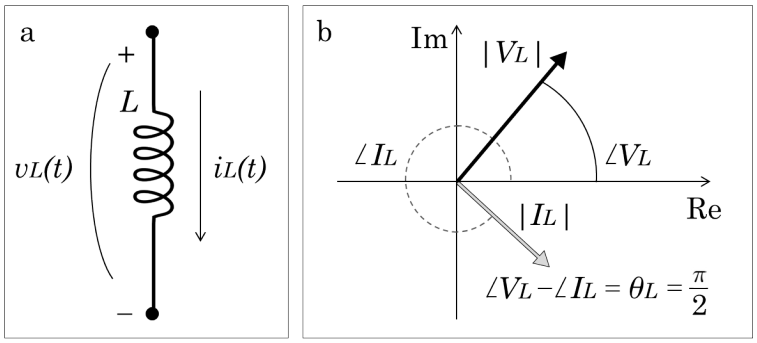

Figure 3.10: ***Inductor.*** *Electrical circuit symbol (a). Phasors representation in the complex plane (b).*

which the coils are wounded. In the generic case of air $\mu_r = 1$. A magnetic flux Φ_B is associated with the magnetic field and its relation with the current from which it is produced, linearly proportional, is

$$\Phi_B = Li_L(t) \tag{3.20}$$

where L is named inductance, it is measured in henry [H] and it depends only on geometrical and constructive parameters of the material of which the element is made. If the current changes over time, also the magnetic flux is obviously variable and it determines an electromotive force, that is a voltage, which opposes to the flux. The Faraday's law establishes that

$$v_L(t) = \frac{d\Phi_B}{dt} \tag{3.21}$$

defining the value of the voltage $v_L(t)$ induced at the terminals of the inductor when a flux variation is produced by the current $i_L(t)$. The Equation 3.20, combined with the Equation 3.21, allows to obtain the voltage-current relation for an inductor as

$$v_L(t) = L\frac{di_L(t)}{dt} \tag{3.22}$$

For an inductor the relation between voltage and current is not linear in the time domain, while in the complex space the Equation 3.22 becomes

$$V_L(\omega) = j\omega L I_L(\omega) \tag{3.23}$$

The imaginary unit $j = \sqrt{-1} = e^{j\frac{\pi}{2}}$ indicates an anticlockwise rotation by $\frac{\pi}{2}$ respect to the horizontal axis. Thus, the inductor impedance can be defined as

$$Z_L(\omega) = j\omega L \tag{3.24}$$

with the observation that it is pure imaginary, with a phase angle $\theta_L = \pi/2$. Figure 3.10b illustrates the phasors representation of V_L and I_L in the complex plane. According to the impedance expression of Equation 3.24, at low

frequencies the inductor tends to behave like an ideal short circuit while at high frequencies follows the open circuit behavior. As previously said, since the mostly of IS systems rarely present inductive elements, it is a common procedure to represents -Im($\bar{Z}$), instead of Im($\bar{Z}$), as a function of Re($\bar{Z}$) in Nyquist plot.

A capacitor (Figure 3.8c) is a circuit element that stores electrical charges. It consists of two conductive surfaces, called armatures, between which a non-conductive material, called dielectric, is interposed. The electrical circuit symbol of a capacitor is illustrated in Figure 3.11a. If charges of opposite sign are

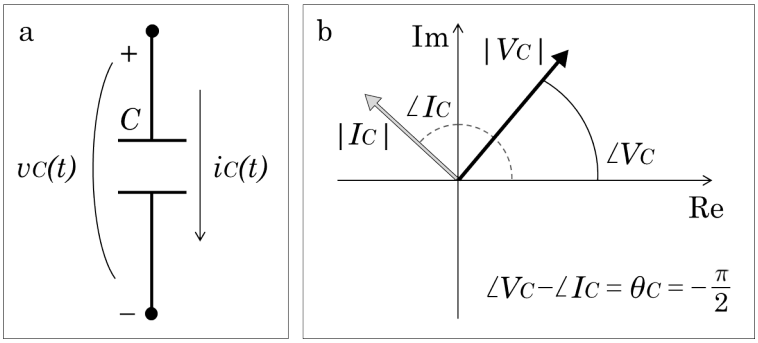

Figure 3.11: ***Capacitor.*** *Electrical circuit symbol (a). Phasors representation in the complex plane (b).*

placed on the armatures, an electrical field is proportionally produced amongst them and then a voltage $v_C(t)$ is generated. A similar thing can be done by imposing a voltage at the terminals, in order to attract the charges towards the armatures, where they accumulate. Anyway, the relation between the generic variable charge $Q(t)$ on the armatures, measured in coulomb [C], and the voltage $v_C(t)$ related to the terminals can be expressed as

$$C = \frac{Q}{v_C(t)} \tag{3.25}$$

where the term C is the capacitance of the capacitor, measured in farad [F] and dependent only on the geometry of the conductors and on the electrical characteristics of the dielectric interposed. The charges on the armatures are not able to pass directly from one terminal to the other because of the presence of the dielectric. Nevertheless, being the voltage variable over time, a displacement current is generated, inducted by one of the two surfaces on the other one. It can be shown that the resulting current at the capacitor terminals $i_C(t)$ is equal to the charge variation over time

$$i_C(t) = \frac{dQ(t)}{dt} \tag{3.26}$$

In this way, rearranging the Equation 3.25 and the Equation 3.26 the voltage-current relation obtained for a capacitor is

$$i_C(t) = C\frac{dv_C(t)}{dt} \tag{3.27}$$

The reasoning seen for the inductor with sinusoidal functions is transferable to the capacitor but, in this case, the voltage is derived, instead of the current. In the complex notation the relations obtained are

$$I_C(\omega) = j\omega C V_C(\omega) \tag{3.28}$$

$$V_C(\omega) = \frac{1}{j\omega C} I_C(\omega) = -j\frac{1}{\omega C} I_C(\omega) \tag{3.29}$$

A capacitor at low frequencies behaves like an ideal open circuit while at high frequencies becomes a short circuit. The imaginary unit at the denominator, that becames negative at the numerator represents a characteristic phase angle $\theta_C = -\pi/2$, associated to a purely real capacitive impedance of

$$Z_C(\omega) = -j\frac{1}{\omega C} \tag{3.30}$$

The phasors V_C and I_C are represented in Figure 3.11b and Figure 3.11b. A summary of the electrical circuit elements just described is presented in Table 3.1.

Table 3.1: *Overview of the expressions describing a resistor, an inductor and a capacitor in the time domain and in the complex space.*

Element	Symbol	Time relation	Impedance	Phase angle
Resistor	R	$v_R(t) = Ri_R(t)$	$Z_R(\omega) = R$	$\theta_R = 0$
Inductor	L	$v_L(t) = L\frac{di_L(t)}{dt}$	$Z_L(\omega) = j\omega L$	$\theta_L = \frac{\pi}{2}$
Capacitor	C	$i_C(t) = C\frac{dv_C(t)}{dt}$	$Z_C(\omega) = -j\frac{1}{\omega C}$	$\theta_C = -\frac{\pi}{2}$

Costant Phase Element (CPE)

Ordinary circuit elements, such as those just described, are considered lumped elements because each of them represents a physical parameter that can be considered constant concerning the spatial dimension and related to ideal properties. However, there are some cases in which this assumption can not be made. With the aim of modelling blood, in terms of components and dynamic behavior, ideal circuit elements may be inadequate to describe its electrical response. In addition, the interaction of blood with electrodes is too complex to be represented with the ideal response expected for a single electrochemical reaction. In fact, the interaction between a biological fluid and a metal electrode forms a narrow interface, known as double layer, where the charges of the

electrode and those of the material are separated and the current thus flows as in a capacitive layer. The value of the double layer capacitance depends on the electrode potential, the temperature and its variation, the charges concentrations, the kind of material, the electrode roughness and the possible adsorption of impurities.

For these reasons, in addition to the three common electrical circuit elements, it is useful to define the Constant Phase Element (CPE) [16], often used as representative element in equivalent circuits. The CPE is a generalization of conventional capacitors and it is considered a sort of lumped electrical circuit element with distributed properties, looking at the imperfect response of real systems. The impedance of a CPE $Z_{\mathrm{CPE}}(\omega)$ is defined as

$$Z_{\mathrm{CPE}}(\omega) = \frac{1}{C_{\mathrm{CPE}}(j\omega)^{\psi}} \tag{3.31}$$

where C_{CPE} is the capacitance, while the parameter ψ, with $0 \leq \psi \leq 1$, is the CPE index. Being an imperfect capacitor, the impedance phase angle is usually less than -90 deg. In particular, $\theta_{\mathrm{CPE}} = -\psi\pi/2$ and the CPE resembles a pure resistor when $\psi = 0$, while it looks like an ideal capacitor when $\psi = 1$ [16].

Warburg element

In electrochemical systems the diffusion of ionic species at the interface is a common phenomenon. In 1899 the physicist Emil Warburg determined an impedance due to the diffusional transport of electroactive species to and from an electrode surface. Diffusion can thus create an impedance called Warburg impedance $Z_{\mathrm{W}}(\omega)$, representing a resistive behavior to mass transfer. A Warburg impedance element can be used to model a sort of linear diffusion, that is defined as an unrestricted diffusion to a large planar electrode [16]. This is the simplest diffusion situation because it is only the linear distance from the electrode that matters.

Warburg impedance is given by

$$Z_{\mathrm{W}}(\omega) = \frac{\sigma}{\sqrt{\omega}} - j\frac{\sigma}{\sqrt{\omega}} = \frac{\sigma}{\sqrt{\omega}}(1 - j) \tag{3.32}$$

where σ is the Warburg coefficient or Warburg constant, dependent on diffusion coefficients, on the electrode surface and on the number of electrons involved in the phenomenon. At high frequencies the Warburg impedance is small since diffusing reactants do not move fast. At low frequencies the reactants diffuse farther and the impedance thus generated increases. Warburg can be considered as a CPE with a constant phase, thus independent of frequency. On the Bode diagrams Warburg impedance thus exhibits a constant phase shift of 45 degrees, while in the Nyquist plot it appears as a diagonal with a slop of 45 degrees, with the real and the imaginary components equal at all the frequencies. The impedance depends on the frequency of the perturbation. In particular, the magnitude of Warburg impedance $|Z_{\mathrm{W}}(\omega)|$ is inversely

proportional to the square root of the frequency $1/\sqrt{\omega}$ through the expression

$$|Z_{\mathrm{W}}(\omega)| = \frac{\sqrt{2}\sigma}{\sqrt{\omega}} \tag{3.33}$$

The form of the Warburg impedance is only valid if the diffusion layer has an infinite thickness. Quite often, however, this is not the case. If the diffusion layer is bounded, as in thin-layer cell or in coated samples, the impedance at lower frequencies no longer responds to the Equation 3.32 and the Equation 3.33. Instead, the more finite-length general form to express the Warburg impedance is

$$Z_{\mathrm{W}}(\omega) = (\sigma\ \sqrt{\omega})\ (1-j)\ tanh\left(\delta\sqrt{\frac{j\omega}{D}}\right) \tag{3.34}$$

where δ represents the diffusion layer thickness and D the diffusion coefficient. Without going deeply in details, there are two special conditions of finite-length Warburg elements: the Warburg short, for a finite-length diffusion with transmissive boundary, and the Warburg open, describing the impedance of a finite-length diffusion with reflective boundary.

3.2.2 Electrical equivalent circuit models

In a circuit with two elements in series, $Z_1(\omega)$ and $Z_2(\omega)$ the same current flows through both of them, while the total voltage is given by the sum of the voltages across each element. For this reason, the total impedance $Z_{\mathrm{series}}(\omega)$ related to series of the two elements is given by

$$Z_{\mathrm{series}}(\omega) = Z_1(\omega) + Z_2(\omega) \tag{3.35}$$

Thus, the impedance is additive for elements in series. Symmetrically, by considering two elements in parallel, the total current is given by the sum of the currents flowing into each element, while the total voltage is equal to the voltage across each of them. Accordingly, the total impedance $Z_{\mathrm{parallel}}(\omega)$ is

$$Z_{\mathrm{parallel}}(\omega) = \left(\frac{1}{Z_1(\omega)} + \frac{1}{Z_2(\omega)}\right)^{-1} \tag{3.36}$$

In this case, the admittance is additive for elements in parallel. Both Equation 3.35 and Equation 3.36 can obviously be extended to the series or the parallel of more elements with the same logic.

By exploiting the above reported rules, the impedances related to useful electrical equivalent circuit models is presented. The simpler electrical circuit often found in biomedical applications is the parallel of a resistance R and a capacitance C (Figure 3.12a). The equivalent impedance can be calculated as

$$Z(\omega) = \frac{R}{1 + j\omega RC} \tag{3.37}$$

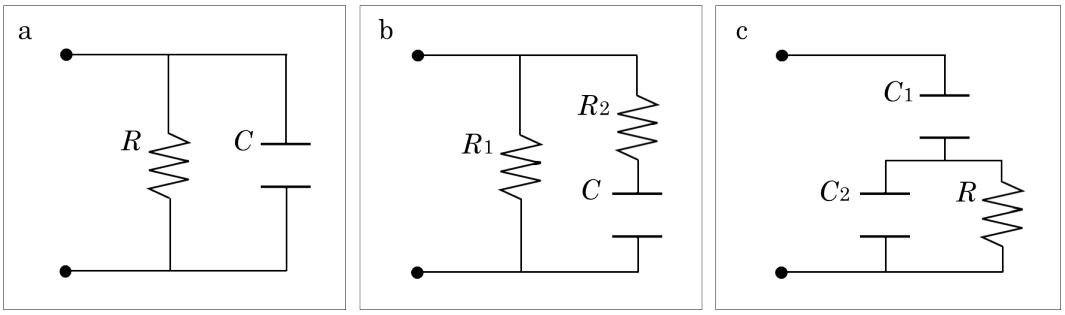

Figure 3.12: ***Useful electrical equivalent circuit models.*** *The parallel of a resistance R and a capacitance C (a). The parallel between a resistance R_1 and the series of another resistance R_2 with a capacitance C (b). The series between a capacitance C_1 and the parallel of another capacitance C_2 and a resistance R (c).*

In the Nyquist plot, this parallel appears as a semicircle centered in $R/2$ with radius equal to $R/2$. Another useful elements combination to be considered, represented in Figure 3.12b is the parallel between a resistance R_1 and the series of another resistance R_2 with a capacitance C. In this case, the equivalent impedance is given by the expression

$$Z(\omega) = \frac{R_1(1 + j\omega R_2 C)}{1 + j\omega R_2 C + j\omega R_1 C} \tag{3.38}$$

Figure 3.12c shows the last important equivalent circuit model recurrent in biomedical impedance spectroscopy, that is the series between a capacitance C_1 and the parallel of another capacitance C_2 and a resistance R. The equivalent impedance is

$$Z(\omega) = \frac{1}{j\omega C_1} + \frac{R}{1 + j\omega R C_2} \tag{3.39}$$

Where considered appropriate or necessary, each capacitance can be substitute by a CPE, with the related changes in the equivalent impedance expressions of Equation 3.37, Equation 3.38 and Equation 3.39. In fact, regarding the Figure 3.12a, substituting the capacitance with a CPE, the resulting parallel between the CPE and R is commonly named ZARC and its equivalent impedance $Z_{\mathrm{ZARC}}(\omega)$ is given by

$$Z_{\mathrm{ZARC}}(\omega) = \frac{R}{1 + j\omega R C_{\mathrm{ZARC}}(j\omega)^{\psi}} \tag{3.40}$$

Commonly found in electrochemical systems is the Randles circuit where a diffusional element, usually a Warburg or a Warburg short is put in series with the charge transfer resistance. This circuit is usually exploited to model an electrochemical system composed by an electrode immersed into an electrolytic solution with dissolved ionic species.

3.3 Metrology fundamentals

The accuracy, precision and fitness for purpose of medical laboratory results rely on the basic metrological concepts of a common system of units, traceability of measured values, uncertainty of measurement and commutability of results within a calibration hierarchy. A measurement system is generally a device whose input, named measurand, is the quantity of interest to be measured and whose output is the measurement result of this quantity. A measurement procedure thus provides a resulting measurement value of the quantity to be measured. The purpose of a measurement is to provide information about a quantity of interest, the measurand.

3.3.1 Measurements, errors and uncertainty

No measurement is exact. When a quantity is measured, the outcome depends on the measuring system, the measurement procedure, the operator skills and the environment. No measurement is exact, thus every measurement is affected by error. In the international vocabulary of metrology (VIM) the measurement error is defined as the value obtained from the measured quantity value minus its the reference quantity value [81]. Measurement error, as difference between the measured value and the true value, is therefore intended as a single number, even if consisting of random components, unpredictable because of their unknown origin, and systematic ones, more or less compensable if identified. In practice, the true value of a measurand is nowadays considered unknown because a physical quantity can not determined with absolute certainty and a content of vagueness has always to be associated to the measurement. In metrology, the parameter representing the dispersion of the values attributed to a measured quantity is called uncertainty and, for this reason, a measurement result is complete only when it is accompanied by the associated uncertainty. In general, error may refer to a single discrepancy, as for a systematic error or biases and it can be appropriately corrected, while random fluctuations lead to uncertainty. Because of this incompleteness in the detailed definition of any quantity to be measured, there is not a single true value for a measurand, but a coherent range of plausible values, although they are not exactly known. Uncertainty has become a basic property of measurements and to calculate it, unlike measurement error, it is not necessary to know the true value of the physical quantity under investigation. The uncertainty assessment is necessarily required in order to decide if the measured result is adequate for its intended purpose and to establish if it is consistent with other similar or previous results. By international agreement, the uncertainty is a statistical concept that has a probabilistic basis and reflects the incomplete knowledge of the quantity value, whose measurement has to be thus defined through a range of values within it is probably included.

The measurement of a quantity should involve its comparison with a sample of known value. This operation is not always possible because for many

quantities, especially in the biomedical field, a reference quantity does not exist because it has never been quantified. Consequenlty, two types of measurements are then possible. The simplest is the direct measurement, done measuring the quantity directly with an instrument and comparing the measurement with a reference sample. The other possibility is represented by the indirect measurement. In this case, the quantity of interest is not directly measured, but it is obtained from measurement of other quantities related to it. An example is the measurement of resistance through the Ohm's law.

A measurements is thus an estimate of the true unknown value of the quantity, as it is not possible to know exactly its real value because of the the presence of random phenomena and imperfections in the correction of systematic errors, often difficult to be identified and quantified. Even if all the error components are evaluated and compensated, still the uncertainty remains on the provided results and this is a doubt on how good the result represents the true value of the measurand. The uncertainty is associated to the measurement result and represents the dispersion of the values that can reasonably be attributed to the measurand. Therefore, a measurement result is composed and described by:

1. the measured quantity, the value that can be directly obtained from the measurement system, obtainable from a single measurement or as mean value of a series of measurements;

2. the measurement uncertainty, that quantifies its reliability;

3. the unit of measurement, used to report the measured quantity to a scale of default values.

These three elements alone provide a complete description of a single measurement. In addition, it is important to give some basic definitions of the terms commonly used in metrology:

- accuracy is the closeness of agreement between a measured quantity value and the true quantity value of a measurand;

- resolution is the smallest change in a quantity being measured that causes a perceptible change in the corresponding measurement;

- sensitivity is the quotient of the change in an indication of a measuring system and the corresponding change in a value of a quantity being measured;

- dynamic range is the ratio, often expressed in dB, between the maximum and the minimum values that can be measured with the same instrument settings;

- precision is the closeness of agreement between indications or measured quantity values obtained by replicating measurements on the same or similar objects under specified conditions;

- repeatability is the precision in repeated measurements with the same measurement procedures, same operators, unchanged conditions and location, replicating measurements on the same or similar objects over a short period of time;
- reproducibility is the precision in repeated measurements in different conditions and measuring systems, replicating measurements on the same or similar objects, with the aim of assess the concordance of the results;
- stability is a property of a measuring instrument, whereby its metrological properties remain invariant in time, in the brief term (minutes or hours) or in the long term (days, months or years);
- uncertainty is a parameter indicating the dispersion of the values attributed to a measured quantity and it provides the quality of the measurement method and its result.

Two elements are basic to make a measurement. They are the measurement system, made up of a set of tools and equipment, and the methodology that is the description of how these tools are used to realize the measurement. In addition, the measurement procedure is the most detailed description of how the measurement has to be carried out. In order to decide which measurement system should be used, many aspects and factors have to be taken into account, from the measurement conditions to the measurement parameters, range and accuracy. To make an increasingly accurate and reliable measurement, it is advisable to carry out more measurements at the same conditions, thus allowing the identification of many sistematic errors and the evaluation of the correctness regarding the chosen methodology. Furthermore, more measurements provide a statistical description of the uncertainty that can be so quantified experimentally as well as theoretically.

3.3.2 Uncertainty evalutation and propagation

Even if the terms error and uncertainty are used somewhat interchangeably in everyday descriptions, they actually have different meanings according to the definitions provided by VIM and by the guide to the expression of uncertainty in measurement (GUM). By definition, the measurement error is the difference between the true value and the measured value. The most likely or true value may thus be considered as the measured value including a statement of uncertainty which characterises the dispersion of possible measured values. As the measured value and its uncertainty component are at best only estimates, it follows that the true value is indeterminate [81, 82]. Uncertainty is caused by the interplay of errors which create dispersion around the estimated value of the measurand; the smaller the dispersion, the smaller the uncertainty.

Uncertainty of measurement, traceability and numerical significance are related concepts that affect both the format and the information transmit-

ted by a quantitative result. As every measurement is prone to error, it is often stated that a measurement result is complete only when accompanied by a quantitative statement of its uncertainty. This uncertainty assessment is required in order to decide if the result is adequate for its intended purpose and to ascertain if it is consistent with other similar or previous results. The uncertainty of quantitative results must thus always be available to demonstrate how well a measured value represents the quantity being determined. The GUM is generally accepted as the master document describing the theory and implementation of uncertainty of measurement and the general law for the propagation of uncertainty. In metrology, measurement uncertainty is a non-negative parameter characterizing the dispersion of the values attributed to a measured quantity [81]. All measurements are subject to uncertainty and a measurement result is complete only when it is accompanied by a statement of the associated uncertainty. By international agreement [81, 82], this uncertainty has a probabilistic basis and reflects incomplete knowledge of the quantity value. The measurement uncertainty is often taken as the standard deviation of a state-of-knowledge probability distribution over the possible values that could be attributed to a measured quantity. In clinical biochemistry, in fact, this may be the variability or dispersion of a series of similar measurements, for example a series of quality control specimens and it can be expressed as combined uncertainties. Today, many clinical laboratories have more than one instrument which can perform the same group of tests. Laboratories with automated systems which incorporate several analytical modules providing the same test capability may provide uncertainty estimates for each measurand independently from which module actually produced the result. In this type of automated testing system, any differences which may actually be observed between modules are probably considered as random effects, provided that all systematic errors have been correctly identified and appropriately corrected. On the other hand, if the uncertainty analysis is aimed at a specific instrument or module, its imprecision with respect to the group requires a separate evaluation, provided that the systematic errors have been appropriately corrected.

Regarding the measurand as a random variable y, if n repeated measurements x_i, with $i = 1, 2, ..., n$, of the same quantity are made, statistical procedures can be used to determine the uncertainties in the measurement process. This type of statistical analysis provides uncertainties which are determined from the data themselves without requiring further estimates. There are two mathematical approaches to evaluate the uncertainty associated to the measurement result x. Type A concerns the evaluation of the uncertainty $u_A(x)$ using statistical analysis from a series of observations. Type B evaluates the uncertainty $u_B(x)$ with probabilistic methods on the basis of available a priori information. The information or data obtained from type A and type B uncertainty evaluations is essentially the same, even if the procedures are different.

A Type A evaluation of standard uncertainty may be based on any valid

statistical method for treating data. When performing a series of n repeated measurements x_i, with $i = 1, 2, ..., n$, the average value of the sample set $\bar{x}$ is given by the expression

$$\bar{x} = \frac{1}{n} \sum_{i=1}^{n} x_i \tag{3.41}$$

The related sample standard deviation $s(x)$ is defined as

$$s(x) = \sqrt{\frac{1}{n-1} \sum_{i=1}^{n} (x_i - \bar{x})^2} \tag{3.42}$$

where $n - 1$ are the associated degrees of freedom. The uncertainty $u_A(x)$ to be associated with x is the estimated standard deviation of the mean

$$s(\bar{x}) = \sqrt{\frac{1}{n(n-1)} \sum_{i=1}^{n} (x_i - \bar{x})^2} \tag{3.43}$$

providing a quantification of quality and variability of measurement procedure the related results.

Differently, Type B evaluation of uncertainty is usually based on scientific judgment using all of the relevant information available, which may include previous measurement data, general knowledge, the behavior and properties of relevant materials and instruments, specifications of manufacturer, data provided in calibration or uncertainties assigned to reference data taken from handbooks. By assuming appropriate probability distributions, on the basis of experience or other information, the uncertainty $u_B(x)$ can be expressed as the standard deviation of the chosen distribution, tipically normal, uniform, triangular or U-shaped, as a priori evaluation. This evaluation can be applied if there is not the possibility to repeat measurements, because of time delays or costs.

As previously mentioned, in many situations the measurand is not measured directly but it is calculated from other measurements through a functional relationship. From a mathematical perspective, a function f can be regarded as an output quantity y whose value can be derived from one or more input quantities $x_1, x_2, ..., x_n$, upon which the y depends, by applying a defined mathematical formula. In general, a functional relationship indicates that a mathematical relationship exists between the value of the function and the input variables, without specifically identifying the exact mathematical form of the relationship. These input quantities themselves can often be viewed as measurands, with their associated uncertainty. If the measurand y is determined from input variables $x_1, x_2, ..., x_n$ through a functional relationship, the uncertainty of each input propagates through the calculation to an uncertainty in y. Usually, the input variables have no relationship with each other, except through their functional relationship which defines the measurand. Under these circumstances, the input variables are described as having

zero covariance or correlation. On the other hand, there are situations where a separate relationship may exist between two or more of the input variables. Procedures for the propagation of uncertainty arising from both uncorrelated and correlated variables can be derived from the general expression describing the propagation of uncertainty as outlined in the GUM [82]. Given the general expression for the measurand y in terms of input quantities $x_1, x_2, ..., x_n$, that is $y = f(x_1, x_2, ..., x_n)$, a corresponding expression which describes the uncertainty $u(y)$ can be obtained by appropriately combining the uncertainty estimates of the various input $u(x_1), u(x_2), ..., u(x_n)$. With uncorrelated input variables the uncertainty propagates from variables to the measurand as

$$u(y) = \sqrt{\left(\frac{\partial y}{\partial x_1}\right)^2 u^2(x_1) + \left(\frac{\partial y}{\partial x_2}\right)^2 u^2(x_2) + ... + \left(\frac{\partial y}{\partial x_n}\right)^2 u^2(x_n)} \tag{3.44}$$

that can be rewritten in a more compact form as

$$u(y) = \sqrt{\sum_{i=1}^{n} \left(\frac{\partial y}{\partial x_i}\right)^2 u^2(x_i)} \tag{3.45}$$

These Equation 3.44 and the Equation 3.45 state that the squared combined uncertainty $u^2(y)$ of the measurand y is a weighted sum of the squared uncertainties $u^2(x_i)$ of the input quantities x_i, with $i = 1, 2, ..., n$. The partial derivatives are often referred to as sensitivity coefficients, dscribing how the output estimate depends on the individual uncertainties, by determining the sensitivity of the output to uncertainty related to each input. The expression for the propagation of uncertainties for uncorrelated variables described in the Equation 3.44 and in the Equation 3.45, is a special form of the general law for the propagation of uncertainty. In fact, when two or more of the input quantities are correlated, an alternative extended form of the general law of uncertainty propagation is required. The expression is similar to that given in Equation 3.44, but includes an additional term which incorporates the correlation coefficient r between input variables. The coefficient can vary from -1, when there is a perfect negative correlation, to 1, when the correlation is perfect positive. The correlation coefficient between two generic variables x_1 and x_2 is defined as

$$r(x_1, x_2) = \frac{u(x_1, x_2)}{u(x_1)u(x_2)} \tag{3.46}$$

where the term $u(x_1, x_2)$ is the covariance of the random variables and represents the relation between their variability. An example describing the uncertainty propagation due to two input quantities x_1 and x_2 is given by the expression

$$u(y) = \sqrt{\left(\frac{\partial y}{\partial x_1}\right)^2 u^2(x_1) + \left(\frac{\partial y}{\partial x_2}\right)^2 u^2(x_2) + 2r_{x_1,x_2}\left(\frac{\partial y}{\partial x_1}\right)\left(\frac{\partial y}{\partial x_2}\right) u(x_1)u(x_2)} \tag{3.47}$$

with the evidence that, if there is not correlation, when $r = 0$, the last term in Equation 3.47 becomes zero and the expression naturally tends to the same form as Equation 3.44. In the GUM the correct model for uncertainty evaluation is the probabilistic one, but it is still in use, especially in sensors, another model named worst case, which provides an overestimation of uncertainty. It uses the maximum uncertainty of input variables considering the linear sum of all the contributions in absolute value, thus excluding their compensation. In other words, the worst case model is equivalent to the probabilistic one with all the correlation coefficients acting positively with value 1.

3.4 Impedance measurement techniques

The instruments for impedance measurement, commonly named LCR meter, are based on different measurement techniques from which impedance can be obtained. Automated measurement instruments allow you to make a measurement by merely connecting the unknown component, circuit or material to the instrument. However, sometimes the instrument displays an unexpected result. One possible cause of this problem is the incorrect choice of measurement technique. In fact, every impedance measurement technique presents advantages and disadvantages and there is not a single technique that includes all capabilities, so it is necessary to consider the specific measurement requirements and conditions and then choose the most appropriate one according to such factors as frequency coverage, measurement range, accuracy and ease of operation. Hereinafter, the most used and known impedance measurement techniques are summarily described leaving, instead, more details for the description of the AC auto-balancing bridge technique.

3.4.1 DC techniques

To find the impedance, we need to measure at least two values because impedance is a complex quantity. Many modern impedance measuring instruments measure the real and the imaginary parts of an impedance vector and then convert them into the desired parameter. Measurement ranges and accuracy for a variety of impedance parameters are determined from those specified for impedance measurement. In order to obtain an impedance measurement, many DC and AC techniques exist. The impedance of a device under test (DUT) represents the extension of the concept of electrical resistance to alternating current applications. Consequently, in the DC systems the impedance measurement reduces to a resistance measurement because of the lack of the imaginary part. One of the simplest approach is represented by the volt-amperometric technique. As the name implies, it is based on two measurements of which one is represented by a current and the other one is a voltage. Being a simple technique, it is commonly used to measure resistance values. The technique exploits the Ohm's law (Equation 3.1) to perform an indirect

measurement. Regarding the implementation details, there are two types of circuits that depend on the connections of the instruments in terms of potioning of the voltmeter upstream or downstream of the ammeter. The two different circuit configurations would be equivalent with ideal instruments, but in practice a real voltmeter presents its own resistance in parallel and a real ammeter has its own resistance in series, thus influencing the measurement result. In particular, if the resistance to be measured is low, it is advisable to insert the voltmeter downstream of the ammeter, since the parallel of the resistors has little influence on the effective value of the unknown resistance. On the other hand, if the unknown resistance is high, then it is discouraged this approach and it is better to resort to the voltmeter configuration upstream of the ammeter since the relatively small resistance of the ammeter does not affect considerably the series of the two resistors.

The Wheatstone bridge is another specific technique implemented for DC impedance measurement. The Wheatstone bridge configuration is obtained connecting two branches, each with two resistances, in parallel and maintaining an explicit reference to their intermediate point, in order to realize a symmetrical circuit structure in which one of the resistances is unknown but measurable, two are known and of equal value and the other one is variable. Initially, this techniques was used simply to reach the balancing of the two branches, while now it can be used also to measure unknown resistances, taking advantage of this possibility to manually determine the balance point of the bridge at which the difference between the two intermediate points voltages results null. In this way, the value of the unknown resistance can be measured starting from its relation with the other circuit elements of the bridge. The Wheatstone bridge is very effective as measurement technique as it is mainly entrusted to the stability of the passive components forming the branches to be balanced.

3.4.2 AC techniques

Applications requiring components or materials characterization generally involve AC measurement techniques, in which the impedance takes into account also the inductive and capacitive real contributions and depends on the frequency.

The most traditional approach is that of the manual balancing bridge, where the symmetrical structure realized with four impedances allows to obtain the unknown impedance thanks to its relation with the other impedances, as illustrated in Figure 3.13. Initially, the method was used to determine the balancing of the two branches, while now it can be used also for impedance measurements in circuits. In particular, when a sinusoidal voltage is applied, no current flows through the detector and the value of one variable impedance are manually changed until reaching the bridge balancing condition, called null, in which the differential voltage drop is null and therefore the value of unknown

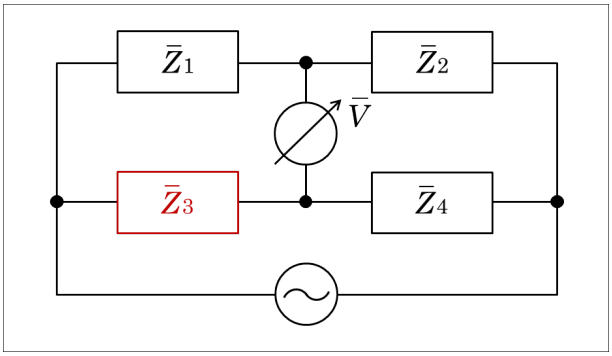

Figure 3.13: ***AC bridge technique.*** *In order to measure $\bar{Z}_3$, the null condition is manually reached varying $\bar{Z}_1$. The expression that relates the impedances is $\bar{Z}_1\bar{Z}_4 = \bar{Z}_2\bar{Z}_3$ and the impedance to be measured can be immediately obtained as $\bar{Z}_3 = \bar{Z}_1\bar{Z}_4/\bar{Z}_2$.*

impedance can be obtained. In particular, according to the Figure 3.13, with the aim of measuring $\bar{Z}_3$, when the null condition is manually reached varying $\bar{Z}_1$, the expression that relates the impedances is $\bar{Z}_1\bar{Z}_4 = \bar{Z}_2\bar{Z}_3$ and the impedance to be measured can be immediately obtained as $\bar{Z}_3 = \bar{Z}_1\bar{Z}_4/\bar{Z}_2$. Various types of bridge circuits, employing combinations of inductors, capacitors and resistances as the bridge elements, are used for various applications, with the advantage of covering a wide range of frequencies even if each single instrument is able to cover a narrow interval of frequencies. The advantages of this technique are the rejection of common-mode disturbances and the fact that the differential amplifier that reads the output voltage always operates around zero. Generally a bridge method is effective as it is mainly entrusted to the stability of the passive components forming the circuit branches. Thus, the accuracy of the measurement does not depend critically on the reading circuits, but on the accuracy of the elements of the bridge. The main defects are the high number of switches present, the need to know a priori the type of impedance, choosing between a limited number of equivalent models as combinations of elements in series or in parallel, and the inconvenience of having to manually balance the bridge. Therefore, these instruments do not therefore adapt to impedance spectroscopy measurements.

Another impedance measurement technique is the AC volt-amperometric technique, where the unknown impedance can be calculated from measured voltage and current values, as in Figure 3.14. Current can be obtained with an ammeter or using a voltage measurement across an accurately known low value resistance, replaced in practice by a low loss transformer to prevent the effects caused by placing a resistance in the circuit. The procedure allows to measure the voltage and the current magnitude and, in addition, the phase difference has to be obtained through a phasemeter and used in conjunction with the magnitude information. The volt-amperometric technique provides unique features in that it can perform measurements on a grounded device, as

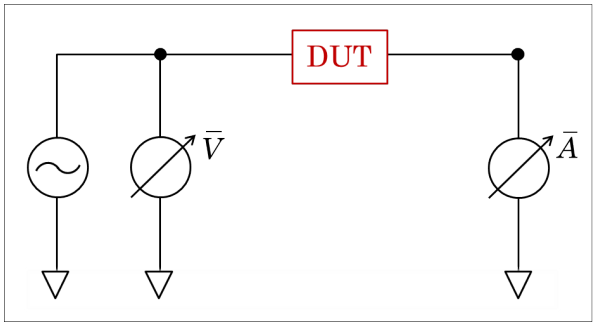

Figure 3.14: ***AC volt-amperometric technique.*** *The unknown impedance of the DUT is calculated from measured voltage and current.*

well as probe components in a circuit. However, the impedance measurement range and the lower frequency range are limited, if compared with those of other techniques.

The radio frequency (RF) volt-amperometric technique is an enhancement of the previous one, which successfully expands the frequency range to the GHz region. This technique is suitable for a broad set of applications in the RF frequency range. The measurement method is the same of the volt-amperometric, but the configuration is different to be able to measure at higher frequences. The signal source section generates an RF test signal applied to the unknown device and typically has a variable frequency range from 1 MHz to 3 GHz. When testing components in the RF region, the RF volt-amperometric measurement method is often compared with the network analysis, a technique that obtains impedance from reflection coefficient measurements and involves a characteristic impedance to be matched, thus limiting the measurement accuracy to the impedance values that are close to the characteristic impedance of the analyzer. The reflection coefficient is obtained by measuring the ratio of an incident signal to the reflected signal detected.

In general, applications requiring impedance measurement, such as components and materials evaluation, utilize the auto-balancing bridge technique, subsequently illustrated and described in detail. This technique provides the best measurement accuracy and the broadest impedance coverage in all the measurements applications from Hz to MHz region. In fact, especially in the biomedical field, many systems under test exhibit an impedance dependency as a function of frequency that requires a measurement instrument with wide frequency coverage. Considering the measurement accuracy and the need of accuracy maintainance for the whole frequency range, the auto-balancing bridge technique appears the best choice for impedance measurements.

Table 3.2 represents an overview of the AC techniques just described and commonly used to measure impedance.

Table 3.2: ***AC impedance measurement.*** *Overview and comparison of the common AC impedance measurement techniques.*

Technique	Advantages	Disadvantages	Range	Application
Bridge technique	- High accuracy - Wide frequency range covered with different types of bridges - Low cost	- Manual balancing - Limited frequency coverage with a single instrument	DC to 300 MHz	- Use in laboratories
Volt-amperometric technique	- Probing measurement - Grounded device measurement	- Limited frequency coverage - Limited impedance measurement range	10 kHz to 100 MHz	- Grounded device measurement - In-circuit impedance measurement
RF volt-amperometric technique	- High accuracy - Wide impedance range at high frequencies	- Limited frequency coverage	1 MHz to 3 GHz	- Components and materials measurement
Network analysis technique	- Good accuracy if the unknown impedance is close to that of the analyzer - High frequency range	- Recalibration required when measurement frequency is changed - Limited impedance measurement range	≥ 10 kHz	- Components and materials measurement
Auto-balancing bridge technique	- High accuracy - Wide frequency and impedance range - Grounded device measurement	- No availability of higher frequency range	20 Hz to 110 MHz	- Grounded device measurement - Components and materials measurement

3.4.3 Theory of auto-balancing bridge technique

The auto-balancing bridge techniques is commonly used in impedance spectroscopy and its operating principles deserves further description because it provides the best combination of accuracy, speed and versatility for a wide range of component measurements. Offering fast measurement speed and outstanding performance at both low and high impedance ranges, the auto-balancing technique represents the best choice to obtained the measurements described as a result.

A huge advantage for modern measurement systems, which has resulted to their great diffusion, is represented by the possibility of having devices for the integrated external communication. This possibility is given by the fact that the acquired signals from measurement bridges can be digitized and numerically computed through processors. There are some basic parameters that must be considered in the use of an auto-balancing bridge:

- the impedance range, specifies the impedance limit of the component to be measured, usually dependent on the value range of each single circuit element that can be measured with the device;
- the measurement accuracy, that specifies how close the measurement is respect to the true value and it is normally specified expressed as a percentage compared to the true value and an added offset measurement uncertainty, that quantifies its reliability;
- the test signal level, that specifies the signal level applied to the component being measured and it is very important for some components whose value may vary with the voltage at their ends;
- the measurement time, that is the actual measurement time of the device and it is very important when many measures must be taken on multiple components, for example in an assembly line; the faster the measurement, the more components can be tested; in addition to the measurement time, the possible time for which the component returns to the normal state must also be considered;
- the temperature range, that can be defined as the variation of the environment temperature in which the meter can work.

To correctly choose an automatic device, it is therefore necessary to consider the kind of measurements to be made and the related expected measurement range.

Basically, for the auto-balancing bridge technique, in order to measure the impedance of the DUT it is necessary to measure the voltage of the test signal applied to the DUT and the current that flows through it. Accordingly, the resulting impedance can be obtained with a measurement circuit consisting of a signal source, a voltmeter and an ammeter. The voltmeter and ammeter measure the vectors in terms of magnitude and phase angle of the voltage and current signals, respectively. In order to perform precise impedance measurements, the voltage applied and the current flowing through the DUT, need to be accurately measured. Figure 3.15a shows the instrument front panel and Figure 3.15b the circuit diagram of the auto-balancing bridge technique, as implemented in the Agilent E4980A high precision LCR meter [83], where the so called 4-wires configuration is generally used. Generally, any interferences of the test signals, or unwanted residual factors in the connections have a significant effect on measurement, especially at high frequency. The E4980A LCR

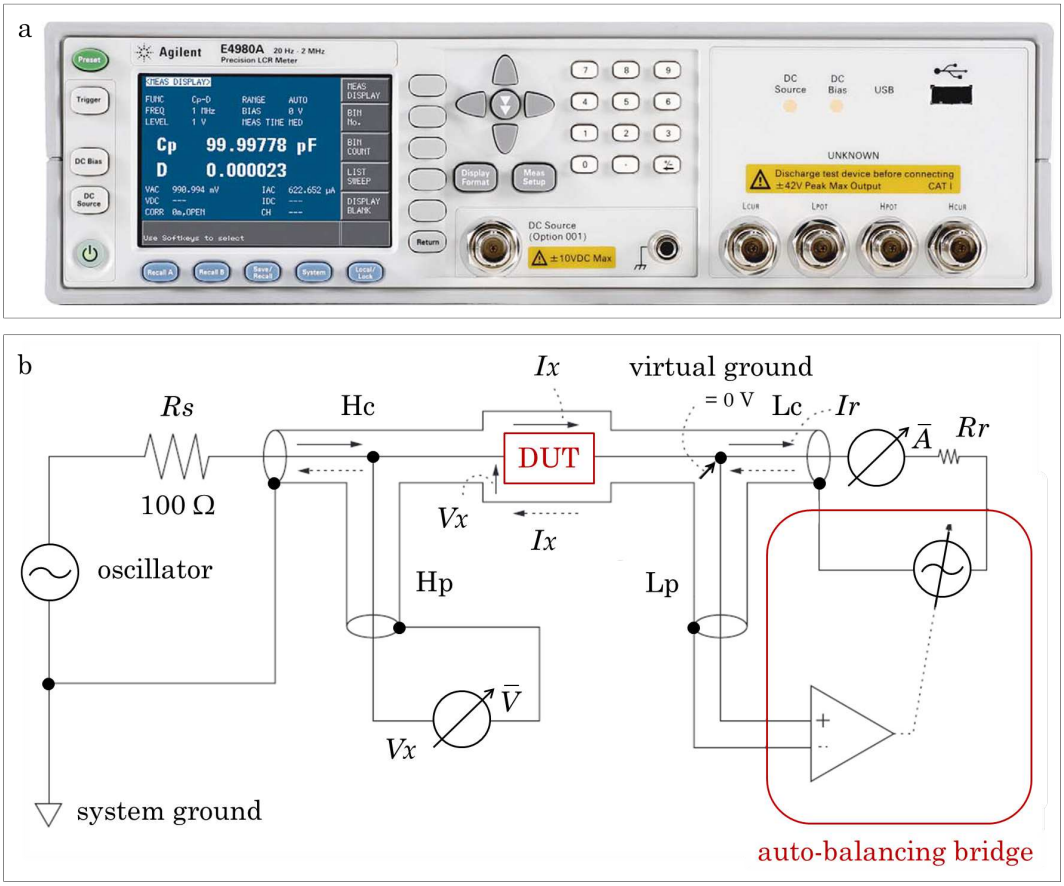

Figure 3.15: ***Agilent E4980A LCR meter based on the AC auto-balancing bridge technique.*** *The null detector detects the unbalance current and controls both the magnitude and phase angle of the balancing oscillator output so that the detected current goes to zero. The current flowing through the DUT I_x is thus equal to the current I_r measured (a). Instrument front panel (b).*

meter employs a 4-wires configuration that permits easy, stable and accuarate measurement avoiding the negative influences inherent in the above factors. The set of unknown terminals consists of four coaxial connectors: high current (Hc), high potential (Hp), low current (Lc), low potential (Lp). Each terminal has a specific role in the auto-balancing technique.

The signal source section generates the test signal applied to the unknown device. The frequency of the test signal and the output signal level are variable. The generated signal is output at the Hc terminal through an source oscillator and a source resistor R_s, measuring about 100 Ω, and it is applied to the DUT. The voltage related to the DUT is detected as V_x at the Hp terminal of the instrument, according to the known source signal and voltage drop across R_s. The oscillator output signal is thus output through the Hc terminal and can be varied to change the test signal level applied to the DUT. The oscillator level should be set as high as possible to obtain a good signal-to-noise ratio (SNR), improving the accuracy and stability of the measurement, but in some

cases the oscillation level should be decreased if critical for the measurement and to the device itself, as in the case of electrochemical reactions occurring at the electrode-material interfaces. The Hp terminal is isolated from the Hc terminal, which is a signal output terminal. This isolation enables accurate detection of the voltage applied to the DUT. The current I_x flows through the DUT and goes towards the Lc terminal. If there exists a certain potential at the Lc terminal, stray capacitance between the terminal and ground is generated and current may flow to the ground. To avoid this, the Lp terminal is kept near the voltage level of the ground. This is called a virtual ground and it is functionally dependent on a feedback loop, called null-loop, generally an high gain operational amplifier that maintains the virtual ground at the Lp terminal and pulls the current I_x to a range resistor R_r. If the range resistor current is not balanced with the DUT current, an unbalance current that equals $I_x - I_r$ flows into the null detector at the Lp terminal. The unbalance current vector represents how much the magnitude and phase angle of the range resistor current I_r differ from the DUT current I_x. The null detector detects the unbalance current and controls both the magnitude and phase angle of the balancing oscillator output so that the detected current goes to zero. The current flowing through the DUT I_x is thus equal to the current I_r measured. Impedance analyzers usually have several range resistors in order to achieve a high resolution for various current measurements. In addition, while low frequency instruments, below 100 kHz, employ a simple operational amplifier to configure the null detector and the equivalent of the oscillator, as shown in Figure 3.15, the instruments that cover frequencies above 100 kHz, considering the performance limits of the operational amplifier, have an auto-balancing bridge circuit consisting of a null detector, a phase detectors and a vector modulator. Anyway, the balancing operation that maintains the low terminal potential at zero volts has the following advantages in measuring the impedance of a DUT. First of all, the input impedance of ammeter becomes virtually zero and does not affect measurements. Afterwards, distributed capacitance of the test cables does not affect measurements because there is no potential difference between the inner and outer shielding conductors of Lp and Lc cables. Finally, guarding technique can be used to remove stray capacitance effects.

Impedance measurement instruments are calibrated at unknown terminals and measurement accuracy is specified at the calibrated reference plane. However, an actual measurement cannot be made directly at the calibration plane because the unknown terminals do not geometrically fit to the shapes of components that are to be tested. Various types of test fixtures and test leads are used to ease connection of the DUT to the measurement terminals. As a result, a variety of error sources are involved in the circuit between the DUT and the terminals. The instrument compensation function eliminates measurement errors due to these error sources. Generally, the instruments have the compensation functions of open, short and load compensation and cable length correction. The induced errors are dependent upon test frequency, test fixture,

test leads, DUT connection configuration and surrounding conditions of the DUT. Hence, the calibration procedure is a key aspect to obtaining accurate measurement results.

With the technology of the feedback loop described, the cabling method called 4-wires configuration is generally used. This configuration minimizes error factors that exist in the measurement path. The 4-wires configuration removes influences such as the series residual impedance of a cable, stray capacitance between cables, and mutual inductance of cables. With this configuration, a wide range of impedance can be measured. In general, many measurement instruments offer both 2-wires and 4-wire measurement capabilities. However, these two techniques are not equally well suited for all impedance measurement applications.

4. Live cells imaging

4.1 Confocal Laser Scanning Microscope (CLSM)

4.1.1 Fundamentals

Optical microscopy is widely used in many systems where the domain of interest lies in the sub-micrometer to micrometer range. These include biological systems such as cells or tissue. Central to the investigation of cellular processes and regulation pathways is the ability to represent and analyze the cell as a three-dimensional (3D) object. A single image taken with a standard microscope produces only a bi-dimensional (2D) representation of a complex 3D specimen. Small adjacent features in the focal xy plane can be resolved distinctly, but their contrast is generally reduced by the out-of-focus fluorescence, originating from the remainder of the cell and obscuring the spatial information. In fact, the spatial relation of features separated along the z-dimension is often not detectable at all. The reduced contrast and the lack of a completely connected 3D view in the conventional fluorescence microscope hamper the understanding of the organization of the fluorescent probe throughout the volume of the cell.

There are several different modes of fluorescence microscopy, each of which will produce a different image of the same specimen. There is no one fluorescence microscopy technique that can be intended as the best one. Instead, the different modes are more or less appropriate for different samples and experimental requirements. The best choice depends on the specimen and the type of information that is needed. It is critical to determine which technique will provide sufficient signal level over the background, lateral and axial resolution and temporal resolution for the experiments [43].

The technique of confocal laser scanning microscope (CLSM) has become an essential tool in biology and the biomedical sciences, as well as in materials science due to characteristics that are not readily available using other traditional microscopy techniques [30, 84–88]. The technique was developed to study organic samples in 3D and to quantify the volume of their different parts without having to destroy and dissect the sample [89]. The development of this technique was motivated by the need to overcome some problems regarding the images acquired by an optical traditional microscope. In particular, these problems were represented by the light reflected from the non-focused

planes making the image blurred and by the light that illuminated the sample spreading in it and disturbing the image. The birth of the basic concept of confocal microscopy occurred in 1957 and it was originally developed by Marvin Minsky when he was a postdoctoral student the Harvard University [90], who patented its principles in 1961 [91] and later became a pioneer in the field of artificial intelligence. As a young research scientist, he saw the limitations of conventional fluorescence microscopes. It was necessary to become able to acquire information from the samples planes of analysis without having the disturb due to the reflection of the out-of-focus planes. To achieve this, he had the idea to equip the optical microscope with a punctual illumination of particular points on the specimen and with one or more pinholes, small holes which suppressed the light coming from the out-of-focus planes. The core of this approach was the use of spatial filtering techniques to eliminate the out-of-focus light in specimens whose thickness exceeded the immediate focus plane. The term confocal derived from this idea and this configuration. Then, in 1969 and in 1971 Paul Davidovits and Maurice David Egger, from the Yale University, published two papers describing the first CLSM [92, 93]. They combined the confocal configuration with lasers to increase the resolution still further.

Confocal microscopy offers several advantages over conventional optical microscopy, including the ability to control the depth of field, the reduction of background information away from the focal plane and the capability to collect sequences of optical sections from thick specimens. These 3D sequences of images acquired along the z-axis have been called z-stacks. In a conventional optical microscope, secondary fluorescence emitted by the specimen often occurs through the excited volume and obscures the resolution of features that lie in the plane focused by the objective. Confocal microscopy provides only a marginal improvement in optical resolution both axial, along the optical z-axis, and lateral, along the x- and the y-dimension. Nevertheless, it is able to exclude from the resulting images the secondary fluorescence related to the regions not fitting with the focal plane. There has been a huge increase in the popularity of confocal microscopy in recent years, due to the relative ease with which very high quality images can be obtained and to the growing number of applications in cell biology that depend on images analysis. Confocal technology has proved to be one of the most important advances ever achieved in live cells imaging. Nowadays, laser confocal microscopy, with computers, can produce 3D images of complex biological materials, included their structural details.

4.1.2 Operating principles

The confocal principles in fluorescence laser scanning microscopy are schematically shown in Figure 4.1. The CLSM is formed by a light source consisting of monochromatic laser beam. The wavelength depends on the type of laser source that can be automatically changed with a specific software. The light

beam is initially filtered to be sure to use a correct intensity. Coherent light emitted by the laser system, the excitation source, passes through a pinhole aperture that is situated in a conjugate plane, confocal, with a scanning point on the specimen and a second pinhole aperture placed ahead of the detector. The first pinhole forms a punctual light source through a perforated disc allowing the illumination of a small area of the sample and a dichroic mirror allows to separate the excitation light from that of the emission, reflecting the light below a certain wavelength and being only traversed by the light with longer wavelength. As the laser is reflected by a dichroic mirror and scanned across the specimen in a defined focal plane, secondary fluorescence emitted from the other points on the specimen, in the same focal plane, pass back through the dichroic mirror and are focused as a confocal point at the detector pinhole aperture. The amount of fluorescence that occurs at points above and below the objective focal plane is not confocal with the pinhole, meaning that it is out-of-focus, and it forms extended Airy disks in the aperture plane. Only a small fraction of the out-of-focus fluorescence emission thus passes through the pinhole aperture, so most of this superfluous light is not detected and does not contribute to the resulting image. The dichroic mirror and a system of lenses perform similar functions to identical components in traditional fluorescence microscopes. Refocusing the objective in a confocal microscope moves the excitation and the emission points related to a specimen to a new plane that becomes confocal with the pinhole apertures of the light source and detector. In the conventional fluorescence microscopy the method of image formation is fundamentally different from that in the confocal approach. With the traditional microscope the entire specimen is subjected to intense illumination from a mercury or xenon lamp and the resulting image of the secondary fluorescence emission can be directly viewed or projected onto the surface of an electronic array detector. In contrast to this simple concept, the mechanism of the image formation in a confocal microscope is basically different. The confocal fluorescence microscope consists of multiple laser excitation sources, a scan head with optical and electronic components, electronic detectors and a computer for acquisition, processing, analysis, and display of images. In particular, the illumination in a confocal microscope is achieved by scanning one or more focused beams of light, usually from a laser, across the specimen. An image produced by scanning the specimen in this way is called optical section or z-slice. The method of sectioning and of image collection by the instrument is clearly non-invasive because of the use of light rather than physical means to section the specimens. The confocal approach has thus facilitated the imaging of live cells, enabled the automated collection of 3D data in the form of z-stacks and improved the images of multiple labeled specimens.

The signal that arrives at the detector is converted into digital and sent to the computer for data acquisition and features extraction. The computer is the fundamental element of this microscope because it allows to modify every parameter before and during the experiments. The microscope is connected

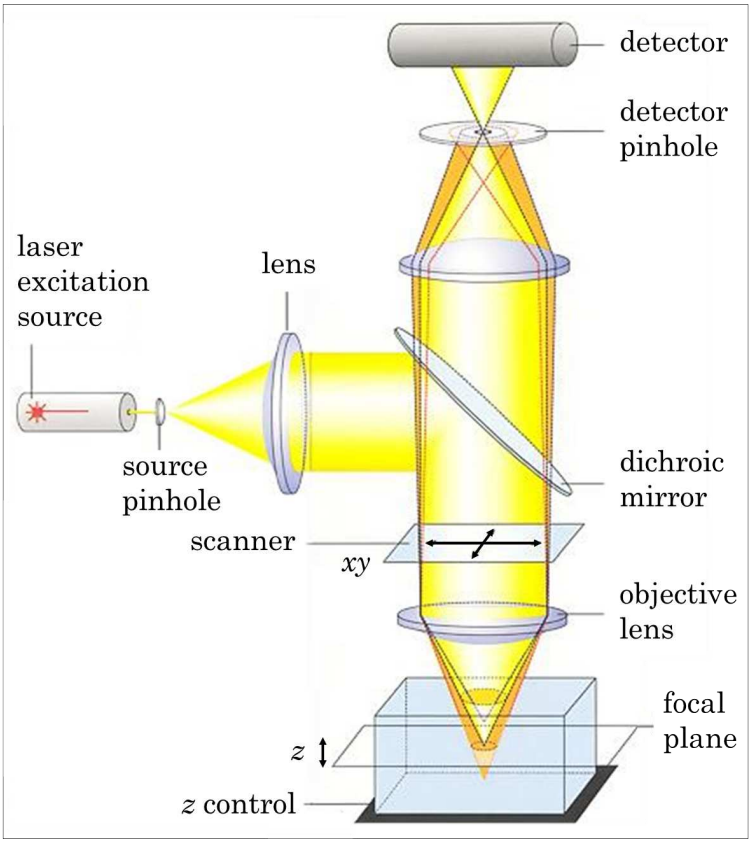

Figure 4.1: ***Confocal laser scanning microscope.*** *The light emitted by the laser source passes through a pinhole aperture. The first pinhole forms a punctual light source allowing the illumination of a small area of the sample and, through a system of lenses and a dichroic mirror, the excitation light and that of the emission are separated. As the laser is reflected by a dichroic mirror and scanned across the specimen, secondary fluorescence emitted from the other points on the specimen pass back through the dichroic mirror and are focused as a confocal point at the detector pinhole aperture. Most of the out-of-focus fluorescence is not detected and does not contribute to the resulting image.*

with the detector, that sends images on the screen where it can be visualized in real time.

4.1.3 Hardware components configuration

The nature of the fluorescence process requires some key elements in the optical systems. With the aim of exciting fluorescence, an illumination source must be delivered onto the sample. Illumination is realized and achieved by a series of lenses which usually consist of a collimator and of an objective. The detection of the emitted signal then requires an optical element for light collection, usually an objective lens, and a detector, that can be the human eye, a charged coupled device (CCD) camera or a photomultiplier tube (PMT). The

geometrical arrangement of the above mentioned elements makes the difference between widefield and confocal systems.

The confocal optical scanner is used in conjuction with the microscope, the light source, the digital CCD camera and a computer workstation running the acquisition software. The confocal optical scanner is mounted onto the microscope and it is attached to the digital camera and the light source. The confocal scanner is of the Nipkow disk type. In a Nipkow scanner the specimen under study is illuminated by the light passing through a spinning pinhole disk, as illustrated in the Figure 4.2. Then the image collected by the microscope objective lens passes back through the same pinhole disk transmitting the in-focus light from one plane, rejecting stray light and producing a sharp image of a single plane or z-slice of the specimen. The confocal optical scanner

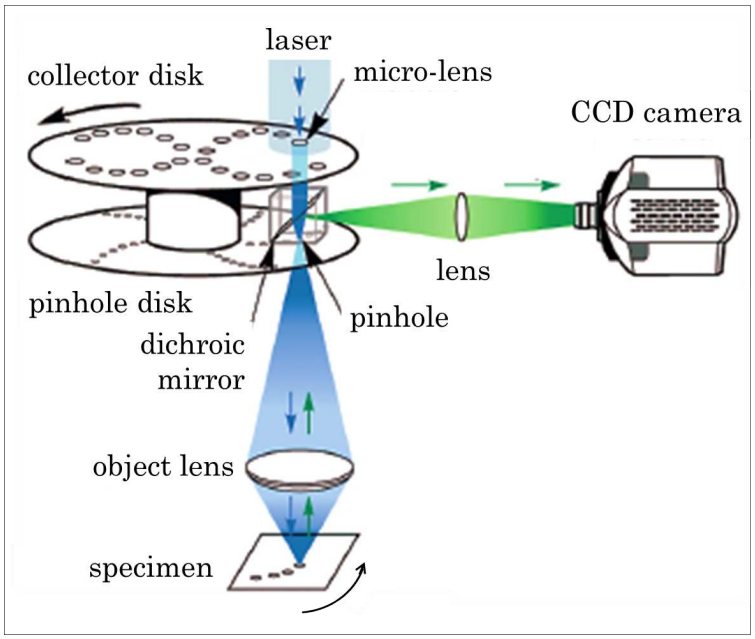

Figure 4.2: ***Nipkow disk for the confocal scanner.*** *In a Nipkow scanner the specimen under study is illuminated by the light passing through a spinning pinhole disk. The scanner increses light throughput and sensitivity by including a second disk with micro-lenses accurately aligned with the pinholes. Light is gathered by the micro-lenses and focused on to the pinholes, producing an high increse of the illumination of the sample.*

increses light throughput and sensitivity by including a second disk, shown in the Figure 4.2, with micro-lenses accurately aligned with the pinholes. Light is gathered by the micro-lenses and focused on to the pinholes, producing an high increse of the illumination of the sample. Further improvements can also be achieved separating the illumination beams and the image beams between the two disks. With this configuration, a real time, high speed, bright image of a well defined plane of the specimen can be achieved.

The scanner is a unit based on two or more mirrors, which guide the focused

laser beam across the specimen. The scan head is at the heart of the confocal system and it is responsible for rasterizing the excitation scans, as well as collecting the photon signals from the specimen that are required for the assembly of the final image. In a CCD image sensor, pixels are represented by p-doped metal oxide semiconductors (MOS) capacitors. These capacitors are biased above the threshold for inversion when image acquisition begins, allowing the conversion of incoming photons into electron charges at the semiconductor-oxide interface. The CCD is then used to read out these charges. Although CCD is not the only technology allowing the light detection, CCD image sensors are widely used in professional, medical, and scientific applications where high-quality image data are required and, for these reasons, in confocal microscopes. The resolution of a CCD camera is function of the number of pixels and their size. If the diameter of the projected image is equivalent to one or even two pixel diagonals, the image reproduction is still not a faithfull reproduction of the object and critically varies on wether the center of the image projection falls on either the center of a pixel or at the vertex of pixels.

4.2 Fluorescence microscopy images

4.2.1 Introduction and background

Mostly of the recent progresses in understanding the biological processes occurring in individual cells derive from the study of their structural and functional organization. During the last decade, live cells imaging has become a distinct field of study and imaging has been increasingly used to enable the interplay of experimental and theoretical biology. Imaging can play a vital role in biological systems investigation, capturing quantitative data with high resolution and doing so non-invasively or minimally invasively in order to preserve the biological functions and structure of cells. With the emergence of automated instrumentation and advanced analysis tools, such imaging approach has become practical for hypothesis driven research and for discovery science.

In addition to being the basic structure blocks of organisms, cells represent the computational unit in biological pathways. Most components of regulatory networks, of signal transduction and of transcription factors act within single cells. Although the interactions and the signaling in general can influence the behavior of distant cells, the quantification and the interpretation of signals are executed within single cells. The output of many biological pathways is a quantitative cellular level representing changes in cell shape, in activity, in proliferation or representing a situation of apoptosis. Because of the action of biological systems over time, specific techniques are needed to assess their temporal dynamics. The structure and the function of biological systems varies from tissue to tissue within an organism, from cell to cell within a tissue and even between subcellular compartments. These differences make different the parts of an unique organism. Live cells imaging has the ability to obtain both

qualitative and quantitative data at all dimensional ranges and it can monitor the status of each cell of a population repeatedly in time, in accord with the timescale of the specific biological process occurring, without disrupting cells and without altering their functions. In this way it is possible to achieve quantitative information about both single cells and the population in terms of average behavior.

There are a number of methods for generating contrast in optical imaging, but the most important approach without doubt is fluorescence. Fluorescence imaging permits a number of different color channels to be imaged in one specimen and allows a wide range of very specific structures and even molecules to be detected. Small molecule fluorophores can be used to mark a variety of structures in order to measure ion concentrations, such as Ca^{2+} and other ions, to evaluate the cellular functions, to identify structures and shapes quantifying objects. In fluorescence microscopy the image contrast is often degraded by high background arising from out-of-focus regions of the specimen. This background can be greatly reduced by several methods such as confocal scanning microscopy. The major application of confocal microscopy in the biomedical sciences is for imaging either fixed or living tissues that have been labeled with one or more fluorescent probes. When these samples are imaged using a conventional light microscope, the fluorescence in the specimen in focal planes away from the region of interest interferes with resolution of the structures in focus. The confocal approach provides a slight increase in both lateral and axial resolution. It is the ability of the instrument to eliminate the out-of-focus flare from thick fluorescently labeled specimens that caused the explosion in its popularity. Fluorescence microscopy thus provides a spatially and temporally measurement of the concentration of multiple molecules in cells and tissues. The wide variety of labels and a range of new imaging techniques and modalities have transformed fluorescence microscopy from a simple localization test to a suite of quantitative tools for functional analysis. Considering the wide use of fluorescence microscopy and the development of new methodologies, it has become important for biologists and physicians to be able to critically evaluate fluorescence images and to perform quantitative analysis.

All the types of optical microscopes are limited in the resolution that they can achieve by a series of physical factors [30, 84–87, 94]. The performance and limitations of each system depend on a common key element, that is the objective lens. In all optical systems diffraction limits the capabilities of the system. Regardless of the sample or imaging method, a successful imaging experiment requires achieving sufficient resolution and signal-to-noise ratio (SNR) to obtain a definitive result. The SNR, defined as the ratio of the average signal value to the standard deviation of the background, varies greatly depending on the imaging system and determines the minimum level of detectable fluorescence [30, 43, 95]. Collecting images with high signal level and low noise reveals important for quantitative fluorescence microscopy, as images with poor SNR yield less accurate quantitative results.

4.2.2 Resolution and point spread function

The spatial resolution in a microscope image is defined as the ability to distinguish two separate objects as separate [94]. In a perfect optical system, resolution is restricted by a fixed solid angle, the numerical aperture (NA), of the optical components and by the wavelength of both incident and detected light, that are the excitation and the emission ones, respectively. The concept of resolution is related to that of the contrast, and it is defined for two objects of equal intensity as the minimum separation between two points that results in a certain level of contrast between them. In other words, contrast can be indicated as the difference between their maximum intensity and the minimum intensity occurring in the space between them [30, 96]. At decreased distance, as the two point spread functions begin to overlap, the dip in intensity between the two maxima and the contrast are increasingly reduced. The distance at which two peak maxima are no longer discernible, and the contrast becomes zero, is referred to as the contrast cut-off distance [94, 97]. In a typical fluorescence microscope, contrast is determined by the number of photons collected from the specimen, from the dynamic range of the signal, from optical aberrations of the imaging system, and from the number of pixels per unit of area in the final image [30, 96].

The objective lens can only collect photons within a fixed NA. The NA is the product of the refractive index n of the immersion medium and the sine of the angular aperture of the lens $\sin\alpha$, as presented in the Figure 4.3a. On

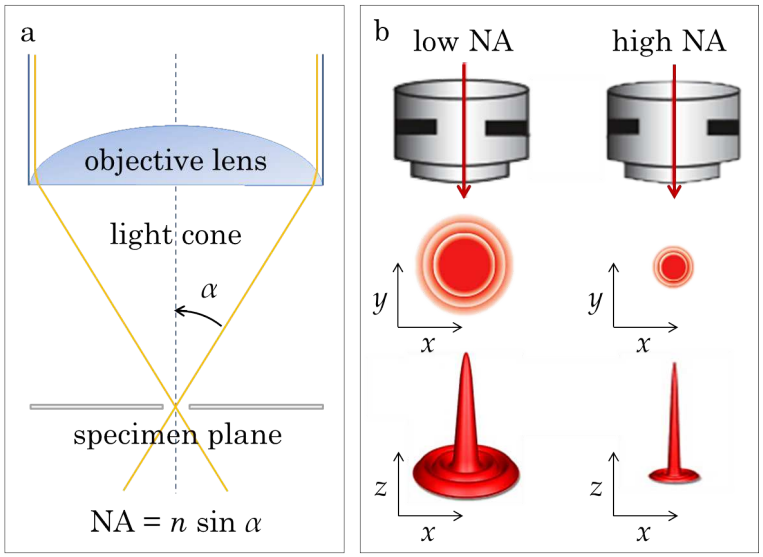

Figure 4.3: ***Numerical aperture and Airy disk size.*** *For an objective lens, the numerical aperture (NA) is the product of the refractive index n of the immersion medium and the sine of the angular aperture of the lens* $\sin\alpha$ *(a). Objects are reproduced, according to the objective NA and the light wavelength, as Airy patterns in the xy-plane, disks surrounded by concentric rings with a specific 3D distribution in space (b).*

the other hand, fluorescence is emitted isotropically in all spatial directions. As the collected emission is only part of all emitted light, information is lost. Higher spatial frequencies do not pass through the aperture. As a consequence, the resolving power is limited so details below the resolving power cannot be separated. In optical systems limited by diffraction, a point shaped object is reproduced in the xy-plane as an Airy pattern, a disk surrounded by concentric rings, whose representation and whose 3D distribution in space are shown in the Figure 4.3b. The disk diameter, and thus the ring pattern, are defined by the objective NA and the light wavelength. As long as the object dimensions are smaller than the resolving power, the image of these structures will always be represented as Airy patterns.

The spatial distribution of light in the three dimensions when emitted from a point is called the point spread function (PSF) [30, 96] and it is represented in the Figure 4.4a. This function provides a measurement of the microscope performance [30, 94, 96, 97]. The intensity distribution of a complex structure, above the resolution limit, can be represented by the superposition or convolution of a series of single point objects. The image is then constructed as the superposition of the PS functions of these point objects. The ability to discriminate two objects as separate entities is referred to as the microscope resolving power. Showing the Figure 4.4b, the Rayleigh criterion defines two objects as resolved if their relative distance is sufficiently large to separate the corresponding PS functions at least by one minimum, that is the dark fringe between the disk and the first ring, alternatively said the radius of the first dark ring in the Airy pattern. This value is proportional to the full width at half maximum (FWHM) of the PSF.

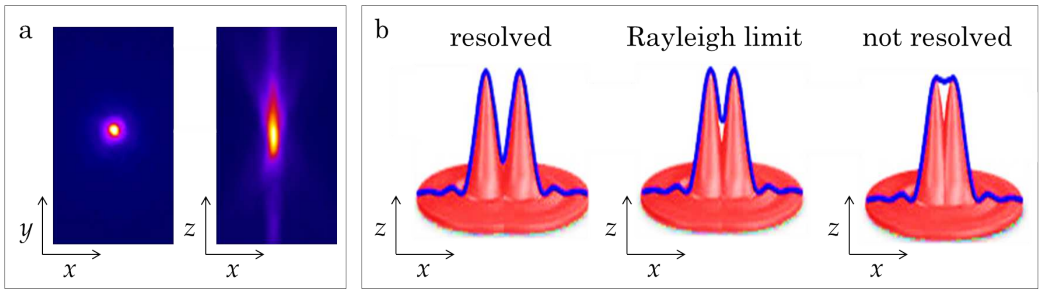

Figure 4.4: ***Point spread function (PSF) and resolution.*** *The PSF of a microscope represents the distribution of the intensity which is created by an object smaller than the resolution limit of the given microscope. The xy-section shows a symmetrical intensity distribution, while the xz-section shows a significant elongation of the intensity profile in z-direction (a). Rayleigh criterion, that defines two objects as resolved if their distance is sufficiently large to separate their point spread functions (b).*

The PSF of a microscope can be identified by imaging point objects (i.e. fluorescence beads) and then measuring the parameters of the diffraction pattern. This method also reveals optical aberrations that may compromise the

performances of the system. The definition of resolving power also requires consideration of a second parameter controlling the visibility, that is the contrast. If the signal-to-noise ratio (SNR) is too low, it will be very difficult to find the values for the theoretical resolution limit. The definition of resolving power therefore depends on the quality of the collected images. Experimentally it is possible to measure the intensity PSF in the microscope by recording the image of a sub-resolution spherical bead as it is scanned through focus. Because of the technical difficulty posed in direct measurement of the intensity point spread function, calculated point spread functions are commonly utilized to evaluate the resolution performance of different optical systems. Although the intensity PSF extends in 3D, with regard to the relation between resolution and contrast, it is useful to consider only the lateral components of the intensity distribution, with reference to the familiar Airy disk [94, 96]. The elongated shape in the direction of the optical z-axis demonstrates the anisotropy of the system. The resolution limit d_{xy}, so the minimal resolvable distance in the image plane is defined as

$$d_{xy} = \frac{0.61\ \lambda}{\mathrm{NA}} \tag{4.1}$$

where λ is the wavelength and NA is the numerical aperture of the objective lens. Microscope resolution is directly related, therefore, to the FWHM of the instrument intensity PSF in the component directions [30, 96]. The value 1.22 λ/NA is the diameter of the first dark ring and referred to as a unit of measurement for the spatial resolution named Airy unit (AU). A similar consideration can be applied to the measurement of the axial resolution limit for fluorescence microscopy. The z-extension of the first dark ring d_z is thus provided by

$$d_z = \frac{2\ n\lambda}{\mathrm{NA}^2} \tag{4.2}$$

where n is the refractive index of the immersion medium ($n = 1$ for air, $n = 1.51$ for oil, $n = 1.33$ for water). In traditional microscopy the illumination apparatus creates a homogenous intensity distribution through a volume extending over a considerable thickness outside the focal plane with an energy flux that is constant throughout the three dimensions. Consequently, the system resolution is determined by the detection of the PSF [30, 94, 96, 97]. The wavelength λ is the wavelength of the emitted light. In confocal microscopy the scanned laser beam produces an image in the focal plane corresponding to an Airy distribution depending on the excitation wavelength. PSF is instead the projection of the pinhole into the focal plane. For image acquisition, the pinhole diameter is set to cover the projected laser beam diameter. As a consequence, the Equation 4.1 and the Equation 4.2 efficiently provide an estimate of the lateral and axial resolutions in a confocal microscope if λ is set to the excitation wavelength. The Equation 4.2 is an approximation of the

real FWHM provided by

$$\frac{0.88\ \lambda}{n - \sqrt{n^2 - \mathrm{NA}^2}} \tag{4.3}$$

Although the confocal microscope configuration exhibits only a modest improvement in measured axial resolution over that of the traditional microscope, the true advantage of the confocal approach is in the optical sectioning capability in thick specimens, which results in a dramatic improvement in effective axial resolution over conventional techniques. The optical sectioning properties of the confocal microscope result from the characteristics of the integrated intensity PSF, which has a maximum in the focal plane when evaluated as a function of depth. The equivalent integral of intensity point spread function for the conventional microscope is constant as a function of depth, producing no optical sectioning capabilities.

4.2.3 Sampling rate and digital resolution

When evaluating the performance of an optical microscope, one has to remember that all considerations made so far assume continuous light intensity distributions. In reality, data collection by detectors, such as the human eyes or a digital detector, represent the result of a sampling operation at a defined frequency. The discrete values of intensity are given as bit-depth. In paricular, monochromatic image bit-depth generally varies from 8, corresponding to 256 (2^8) intensity levels up to 12 and 16 bits, corresponding to 4096 (2^{12}) and 65536 (2^{16}) intensities, respectively. The increased bit number obviously grants an increased light intensity resolution. However, image visualization on the computer screen is usually limited by the monitor performance and no substantial gain is obtained for qualitative analysis. Real image quantification fully employs this increased linearity range by shifting the saturation limit to higher levels. Spatial resolution of the system is not influenced by bit depth but relies on the number of pixels into which the field of view is divided, that is the spatial sampling frequency. Digital images, recorded both from widefield and confocal microscopes, are arrays of pixels and each of them has a physical dimension which results from the spatial extension of the total field of view and the digital dimensions, in terms of number of recorded pixels. The field of view depends on the magnification factor of the objective and the zoom factor. In particular, the size of a single pixel is equal to the distance between the detection units in the detector when projected into the focal plane. Pixel sizes range from millimeters to nanometers. In a CCD camera, the pixel corresponds to the area of the photoactive cells that compose the camera chip. This area divided by the total magnification of the microscope provides the pixel size in the object.

In traditional microscopy the physical dimension of a pixel is fixed and relates to the linear extension of the detector and the number of elementary sensor units in the CCD camera. To adapt the CCD detector size to the field

of view, relay optics are often used, with additional factors of magification. This factors has to be included in the calculation for pixel dimensions. Confocal microscopes allow a dynamic variation of the scanned area. This provides an efficient and flexible tool for controlling the spatial sampling frequency and thus the pixel dimension. In a confocal microscope, each pixel is assigned to a certain position of the laser beam in the scanned grid. Pixel spacing is controlled by the objective magnification and the movement of the scanning mirrors. As the movement of the scanning mirrors is accessible to the operator, the scanning microscope provides additional freedom as compared to the conventional microscope.

The smallest distance resolved is clearly equal to the pixel dimension. The size of a pixel must be less than the resolution limit in order to get an image which is really limited by the performance of the optical system employed. The real resolution will not increase ad infinitum when the sampling distance approaches zero. The Nyquist theorem requires a minimal physical dimension for a pixel to get a real reconstruction of the light distribution sampled by the microscope. The minimal sampling distance has to be half the optical resolution limit value in order to record a diffraction limited image. Theoretically one would expect an increasingly better image when sampling more and more data per pixel, action called oversampling. However, this also decreases the SNR and thus the general quality of the image, with a consequent decrease of its real resolution.

Some factors, such as cell viability and sensitivity to thermal damage and photobleaching, place limits on the light intensity and duration of exposure, consequently limiting the attainable resolution. Given that the available timescale may be dictated by these factors and by the necessity to record rapid dynamic events in live cells, it must be accepted that the quality of images will not be as high as those obtained from fixed and stained specimens. The most reasonable resolution goal for imaging in a given experimental situation is that the microscope provides the best resolution possible within the constraints imposed by the experiment.

4.3 Images processing and analysis

The use of image analysis for biological systems study requires much more attention than that needed for many other applications of imaging. Images are comprised of minimal elements or elementary units called pixels, but it is generally the object (i.e. a cell) or the objects population represented by the pixels, not the pixels themselves, that are of interest to a biologist. Thus, for physicians and biologists move their attention from a pixel-based representation of data to an object-based representation of data and this is the principle challenge in analyzing images. Once objects are recognized in images their properties are quantifies, such as shape, size or fluorescence.

At the practical level, image analysis are related to commercial software.

Ideally, a software package would work on very large image sets, allow multidimensional image sets to be visualized, automatically segment and track cells, quantitate the segmented objects, provide methods for using the data for modeling, and provide methods for annotating the data in a standard format. Unfortunately, no such widely useful software exists yet. There are a number of software packages that excel in some of these areas but not others. On the commercial side, the packages of note include Imaris [98], Amira [99], Volocity [100] and Metamorph [101]. These packages are all for general purpose analysis of biological images and provide tools for multidimensional visualization and some segmentation. Academic software packages under active development include ImageJ [102], CellProfiler [103], Starrynite [104], Cell-ID [105] and 3D-DIAS [106]. ImageJ is a Java-based general purpose image analysis program based on the classic NIH Image. CellProfiler is designed for high-content screening and systems analysis of cells grown in culture and performs 2D segmentation and cell-based quantitation [107]. Starrynite is specifically designed to automatically segment and track cells [108]. Cell-ID was developed for automatic segmentation and quantitation of fluorescence protein levels in yeast [105]. 3D-DIAS is designed to automatically segment cells in 3D image z-stacks of differential interference contrast (DIC) images [106].

Image processing is used to correct for problems such as uneven illumination and to enhance images for further analysis, visualization and publication. Image enhancement, such as scaling, brightness and contrast adjustment can be very useful for extracting important parts and information of the image. If two or more images are to be compared, the same processing routine must be applied to each image. In addition, differences in intensity should not to be judged anly on the basis of displayed images, because the measurements can reveal much more information than the human eye is able to discriminate.

4.3.1 Fluorescence digital images

Biological laser scanning confocal microscopy relies heavily on fluorescence as an imaging modality, mainly due to the high degree of sensitivity of this technique combined with the ability to specifically localize structures and to characterize dynamic processes in both fixed and live cells.

Fluorescence and autofluorescence

Many fluorescent probes have been constructed for years to localize specific structural region, such as the cytoskeleton, mitochondria, endoplasmic reticulum, and nucleus [87, 109]. Other probes are employed to monitor dynamic processes and to localized environmental variables, including concentrations of ions (i.e. calcium Ca^{2+}) [85, 87, 110], pH, reactive oxygen species and membrane potential. Fluorescent dyes are also useful in monitoring cellular integrity, identifying a dead and apoptotic cells, endocytosis, exocytosis, signal transduction and enzymatic activity. In addition, fluorescent probes have

been widely applied to genetic mapping and chromosome analysis in the field of molecular genetics. The synthesis of novel fluorescent probes for improved localization continues to influence the development of confocal instrumentation. Fluorochromes or fluorescent dyes have been introduced over the years with excitation and emission spectra more closely matched to the wavelengths delivered by the lasers supplied with the CLSM.

The number of fluorescent probes currently available for confocal microscopy runs in the hundreds, with many dyes having absorption maxima closely associated with common laser spectral lines. An exact match between a particular laser line and the absorption maximum of a specific probe is not always possible, but the excitation efficiency of lines near the maximum is usually sufficient to produce a level of fluorescence emission that can be readily detected. Fluorescence emission collection can be optimized by an appropriate selection of objectives, detector aperture dimensions, dichromatic and barrier filters.

Autofluorescence can be a major source of increased background when imaging some tissues. Autofluorescence occurs naturally in cells and it can be avoided by using an excitation wavelength that is out of the range of the natural autofluorescence. An idea of the amount of autofluorescence can be gained by viewing an unstained specimen at different wavelengths, and taking note of the intensity levels together with the laser power. A relatively simple solution is to collect the experimental images at settings above those recorded for autofluorescence. Autofluorescence can also be removed digitally by image subtraction. Although it is more often a problem, autofluorescence can be intended and used as a low level background signal for imaging cell morphology and structure.

Dye saturation

In confocal microscopy, irradiation of the fluorophores with a focused laser beam at high power densities increases the emission intensity up to the point of dye saturation. In the excited state, when the rate of fluorophore excitation exceeds the rate of emission decay, fluorophores are unable to absorb other incident photons. As a result, a majority of the laser energy passes through the specimen without contributing to fluorophore excitation. Therefore, balancing the fluorophore saturation with laser light intensity levels reresent a critical condition for achieving the optimal SNR in confocal experiments without losing the ability to discriminate the different levels of fluorescence intensity that often reflect important metabolic and functional characteristics.

Photobleaching

Photobleaching is the irreversible destruction of a fluorophore that can occur when the fluorophore is in the excited state. When multiple images of the same field are recorded for a long time, the signal may decrease because of photobleaching. The rate of photobleaching depends on the fluorophore and

intensity of illumination. Photobleaching should be measured in a control specimen and then corrected for in the images to be analyzed. The consequences of photobleaching are suffered in practically all forms of fluorescence microscopy, and result in an effective reduction in the levels of emission. These artifacts should be of primary consideration when designing and executing fluorescence investigations.

4.3.2 Features extraction

Quantitative microscopy measurements are made on digital images. According to the fact that in fluorescence microscopy the intensity value of a pixel is related to the number of fluorophores present at the corresponding area in the specimen, digital images can be used to extract two types of information: spatial (distances, areas, velocities) and intensity (local concentration of a fluorophore). Quantitative measurements of spatial and intensity information in fluorescence microscopy digital images can be used to answer many different questions about biological specimens. The best way to perform experiments depends on many different aspects of the experimental design, such as the molecules being studied, the fluorophores used, the type of specimen, the type of microscope, the method of image analysis, and the hypothesis being tested.

The quantitative analysis of the images represents the ability to transform a visual and intuitivly otpical sensation into its discrete form, allowing its description, classification and univocal interpretation of its spatial and temporal components. Any type of information obtainable from the images analysis reflects a physical quantity and can be extracted from the pixels arrays and from the intensity levels. In particular, the information and parameters that can be quantified from fluorescence images acquired with confocal microscope are listed and classified in the Table 4.1. The characteristics highlighted by the yellow rectangles in the Table 4.1 represent the information of interest on which the thesis work has been centered: thrombus volume evaluation, fluorescence intensity quantification and functional signals variation in space and time.

The ideal path, represented in Figure 4.5 to extract the features of interest starts from the preparation of the sample to be analyzed and passes through the labeling of the structures of interest. Successively, images are collected, preprocessed to assess their quality and the measurement accuracy and finally the features of interest are extracted. Having already introduced the aspects that anticipate the acquisition of images, now it is possible to focus the attention on the images to be acquired and on their characteristics.

Table 4.1: ***Information obtainable from digital fluorescent images.*** *Overview of the 2D, the 3D and the combined 2D/3D measurable physical quantities from the confocal image sequences acquired. The characteristics highlighted by the yellow rectangles represent the information of interest on which the thesis work has been centered.*

	Dimensions	Shape	Signals	Position
2D	- area - perimeter - diameters	- roundness - aspect ratio	- intensity - distribution	- centroid *xy*
3D	- volume - surface - diameters	- sphericity	- intensity	- baricenter *xyz*
2D / 3D	- distances between sectors and structures	- shape variation	- signal variation - signal distribution	- movements - changes of position

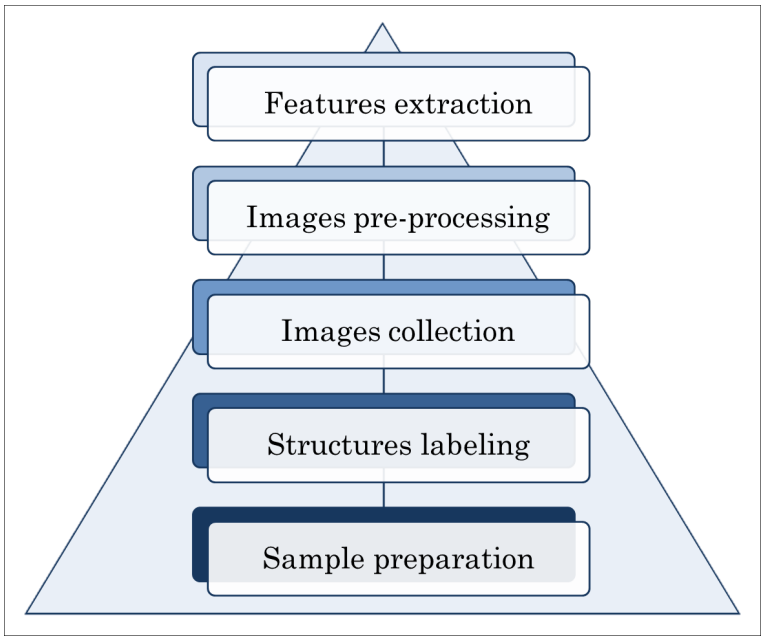

Figure 4.5: ***Ideal path from the sample to the features extraction.*** *The ideal path expect the steps of sample preparation, structures labeling, images collection, images pre-processing and finally the extraction of the features.*

Images collection

The optical z-section is the basic image unit of the confocal microscope. Data are collected from fixed and stained samples generally in single or double wavelength modes. The resulting images are in register with each other and portray

an accurate representation of the specimen, as long as an objective lens that is corrected for chromatic aberration is used. Registration can usually be relatively easily restored using digital methods. The time of image collection also depends on the size of the image and of the speed of the computer.

A z-stack is a sequence of optical sections collected at different levels along the z-dimension from the specimen under study. The z-series are collected by correlating the movement of the focus of the microscope with image collection usually using a computer controlled stepping motor to move the stage of the microscope by preset distances. This is relatively easily accomplished using a software that collects an image, moves the microscope stage to reach the desired focus by a predetermined distance, collects a second image, moves the microscope stage the reach the new focus, and carries on in this way until several images through the region of interest are collected. These programs are standard features of most of the commercially available imaging systems. The z-stacks are ideal for further processing into a 3D representation of the specimen using volume visualization techniques. This approach is now used to elucidate the relations between the 3D structure and function of tissues. Care must be taken to collect the images at the correct z-step Δz of the motor in order to reflect the actual depth of the specimen in the image. Since the z-stacks produced with the CLSM are in perfect register, assuming the specimen itself does not move during the period of image acquisition, and are in a digital form, they can relatively easily be processed into a 3D representation of the specimen under investigation. There is sometimes confusion about what is meant by optical section thickness. The series of optical sections acquired in time can also be processed into a 3D representation of the data set so that time represents the fourth dimension. This approach is useful as a method for visualizing physiological changes during development (i.e. calcium dynamics and movements).

Stacks of images generated by the confocal microscope can be thresholded in order to obtain binary images. These images are achieved by setting the pixels that reach a specified threshold as white foreground pixels and those that do not reach the threshold as black background pixels. Determining the threshold criteria has to be discussed according to the analysis scopes.

Accuracy, background and noise

Every quantitative measurement contains some amount of error. Error in quantitative fluorescence microscopy measurements may be introduced by the specimen, by the microscope or by the detector [111, 112]. Inaccuracy due to errors results in wrong answers in quantitative analyses. In addition, measuring biological specimens there is a certain level of natural variability, so variance seen in measurements made on different cells can be due to both biological variability and that which is introduced when making the measurement. To use a fluorescence confocal microscope and digital detector to quantify spatial and intensity information from biological specimens, sources of inaccuracy have

to be identified and reduced as much as possible.

In quantitative fluorescence microscopy, the aim is the measurement of the intensity signal coming from the fluorophores used to label the object of interest in the sample. However, the intensity values in the digital images represent not only the signal of interest, but also background and noise [43, 95, 112].

Background represents an addition to the signal of interest, such that the intensity values in the digital image are equal to the signal plus the background. Background in a digital image of a fluorescent specimen comes from a variety of sources. In order to accurately measure the signal of interest, background should be reduced as much as possible or even subtracted fromthe images.

Noise causes variance in the intensity values above and below the real intensity value of the signal plus the background. The amount of this deviation differs from one pixel to the others in a single digital image, with the maximum variance in an image referred to as the noise level. Noise causes a level of inaccuracy and uncertainty in measurements. To detect the presence of a signal, this has to be significantly higher than the noise level of the digital image. Otherwise, if the signal is at or below the noise level, the variation in intensity caused by noise will make the signal indistinguishable from the noise level in quantitative measurements. The accuracy in quantitative measurements is therefore limited by the SNR of the digital image, from which also the determination of the location of a fluorescently labeled object depends [113–116].

5. Experimental setup and methodologies

This chapter, consisting of a description of the experimental setup and the methodologies implemented and used to perform the experimental activity, is subdivided according to the different projects realized. The chapter will start with the introduction to the equivalent circuits used to model blood and the interface with the measurement electrodes. Then the biosensor for the individual thrombotic profile characterization under flow will be described, giving importance to the optical thresholding method to reconstruct volumes, with the optimization and the automatization of the threshold identification, and the fusion of otpical and impedance data for the same scope. Afterwards, the new algorithm for the improvement of accuracy in volumes estimation will be presented. Another biosensor, this one to perform quality controls of blood components will be described and, finally, also the new software for live cells imaging will be introduced.

5.1 Electrical equivalent circuit models for blood

5.1.1 Electrode-material interface and double layer

Preliminary considerations must be done regarding the blood composition and the interaction between the electrodes and blood, when electrical current flows through an electrode-material interface. The interaction between a biological fluid and a metal electrode forms a narrow interface, known as double layer, where the current flows as in a capacitive layer but the phase shift of current does not reach -90 deg. For this reason it has been previously useful to define the CPE and its impedance, given by

$$Z_{\mathrm{CPE}}(\omega) = \frac{1}{C_{\mathrm{CPE}}(j\omega)^{\psi}} \tag{5.1}$$

where C_{CPE} is the capacitance, not depending on the frequency, while the parameter ψ, with $0 \leq \psi \leq 1$, is the CPE index. Being a non-ideal electrical circuit element, $\theta_{\mathrm{CPE}} = -\psi\pi/2$ and the CPE resembles a pure resistor when $\psi = 0$, while it looks like an ideal capacitor when $\psi = 1$ [16].

5.1.2 Electrical models for single cells and whole blood

As introduced at the beginning, blood is a fluid composed by a conductive liquid, plasma, and the suspension of biological particles like red blood cells (RBC), white blood cells (WBC) and platelets. According to the electrical equivalent models previously described, it appeared essential to associate a physiological correspondance to each circuit element in order to evaluate the adequacy of the equivalent models to the measurement scopes.

Each of the cells suspended in plasma consists of a lipidic cellular membrane, with a capacitive behavior, which contains an intracellular fluid with dielectrical properties similar to plasma. Defining R_i the resistance of intracellular fluid, C_i the capacitive membrane and R_e the resistance of extracellular fluid, the model of a single cell in suspension in plasma can be represented with the circuital model shown in Figure 5.1a. The related impedance $Z(\omega)_{\text{cell}}$ is

$$Z_{\text{cell}}(\omega) = \frac{R_e(1 + j\omega R_i C_i)}{1 + j\omega R_e C_i + j\omega R_1 C_i} \tag{5.2}$$

Since the model must be extended to a wide number of suspended cells, it

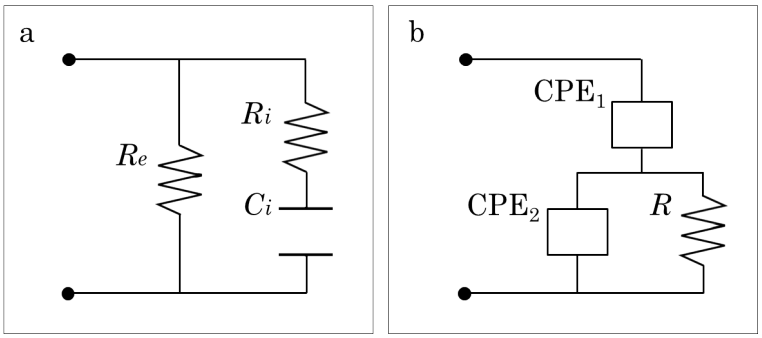

Figure 5.1: ***Electrical equivalent models.*** *Equivalent circuit for a single cell in suspension in plasma (a). Equivalent circuit to describe the whole behavior of blood (b).*

is obvious that the macroscopic impedance is a combination of a corresponding wide number of relations having the form of the Equation 5.2. Each one is supposed to have a different disposition of zeros and poles depending, for example, on the dimensions of cells, on their membrane integrity and on their spatial distribution. The assumed equivalent circuit for the whole blood and its interface with electrodes is represented in Figure 5.1b. The circuit is characterized by a series of a CPE with the parallel of another CPE to a resistor. The expression that governs the overall impedance is

$$Z_{\text{blood}}(\omega) = \frac{1}{C_{\text{CPE1}}(j\omega)^{\psi 1}} + \frac{R}{1 + RC_{\text{CPE2}}(j\omega)^{\psi 2}} \tag{5.3}$$

At the end, the overall blood impedance behavior can be modeled as a series of a CPE, representing the interface effects, with a ZARC.

5.2 Individual thrombotic profile characterization under flow

5.2.1 Blood samples preparation

For each experiment, 2 ml of venous blood were collected into D-Phenylalanyl-L-Prolyl-L-Arginine Chloromethyl Ketone dihydrochloride (PPACK, produced by Calbiochem, La Jolla, CA, 50 μmol final concentration). Informed written consent have been obtained from healthy blood donors according to the Declaration of Helsinki and the DMS of the Italian Ministry of Health, November 2nd, 2015, (quality and safety about blood and blood donors). Moreover, the Ethics Committee CRO-IRCCS Aviano approved all the studies using human blood samples and, therefore, this one. Afterwards, 200 μl droplet of acid insoluble fibrillar type I collagen (produced by Sigma Aldrich, St. Louis, MO, 1 mg ml^{-1} concentration) was applied as coating substrate for 60 minutes, to induce the aggregation process. The fluorescent dye quinacrine dihydrochloride (mepacrine, Sigma Aldrich, 10 μmol final concentration) was added to whole blood to label platelets.

5.2.2 Biosensor description

The new biosensor allows the simultaneous acquisition of optical images and related impedance data during blood perfusion in an artificial microchannel specifically designed and representing the core of the device. The bottom wall was realized with a glass where u-shaped gold electrodes were sputtered, as shown in Figure 5.2a, delimiting an investigation area of 280 x 280 μm^2, visible in Figure 5.2b. The outer electrode measures 30 μm in width, while the inner electrode is 20 μm wide. A SiO_2 passivation layer was set over the tracks to delimit the active area of the electrodes allowing a confocal acquisition like that of Figure 5.2c. More details are given showing Figure 5.3. The other

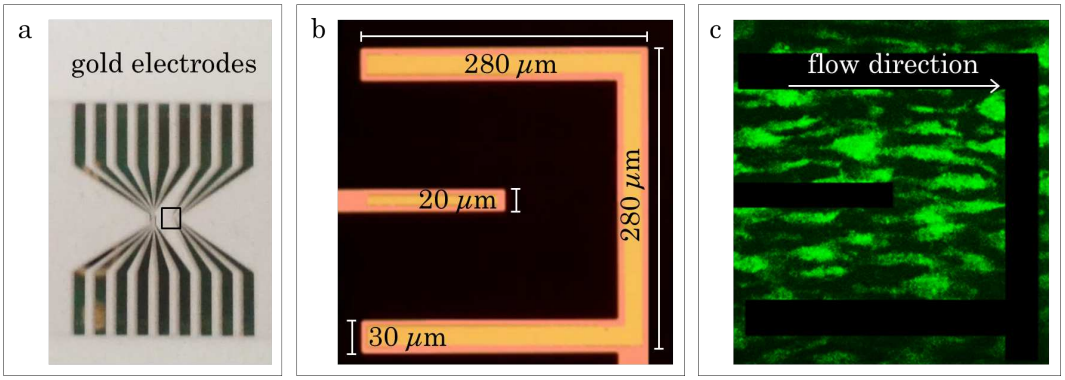

Figure 5.2: ***Gold electrodes.*** *Detail of u-shaped electrodes (a). The gold u-shaped layer is drawn in yellow, while the passivation layer is shown with pink color (b). Example of a corresponding image acquired with confocal microscope (c).*

walls of the microchannel and the microfluidic inlet and outlet connections were molded in a polycarbonate chamber that contains an o-ring for the fluid leakages prevention towards the contacts (Figure 5.3a). The blood can flow from the inlet to the outlet through a cross section of 500 x 100 μm^2. As illustrated in Figure 5.3b, a metallic holder and a component with conductive sensing wires have to be locked one another to complete the assembly of the device.

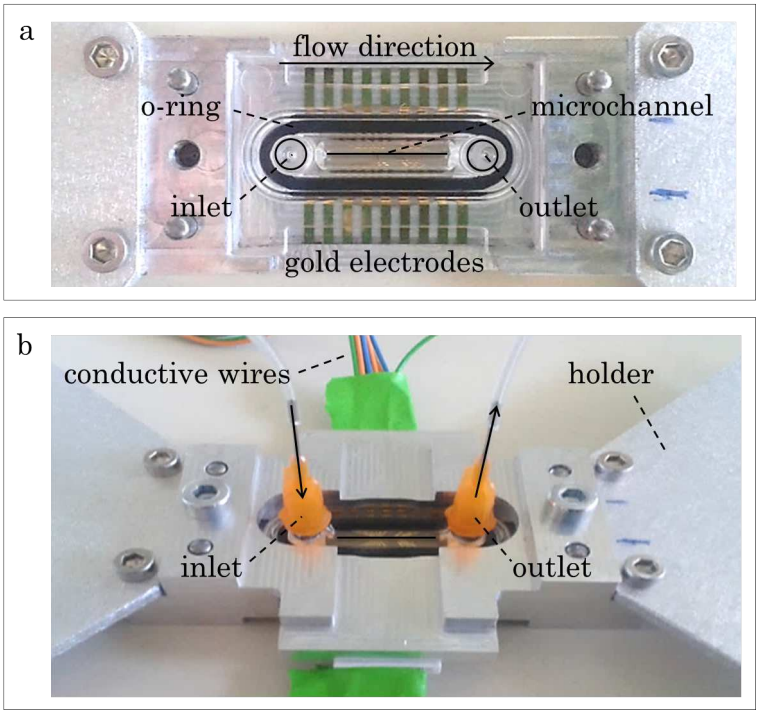

Figure 5.3: ***The new biosensor.*** *The core of the device consists of a bottom glass with gold electrodes and a polycarbonate chamber containing an o-ring that prevents blood leakages. The bottom glass and the chamber define the microchannel (cross section: 500 x 100 μm^2) where the blood flows, from the inlet to the outlet (a). Assembled device, where a metallic holder for the allocation on the microscope and a component with conductive wires have to be locked one another holding the glass with electrodes and the polycarbonate chamber inside (b).*

5.2.3 Acquisition system

The device, connected to a high precision LCR meter [83], was positioned on the stage of a confocal laser scanning microscope (CLSM, Eclipse TE300, manufactured by Nikon, Tokyo, J) based on Nipkow disk technology. A 40X oil immersion objective (numerical aperture: 1.30, Nikon) was mounted on a piezoelectric driver controlled by the Andor IQ acquisition software (made by Andor^{TM} Technology, Belfast, UK). The physiological conditions typical of the microcirculation districts, the arterioles, were reproduced *in vitro* with a

controlled fluid perfusion system. In particular, a syringe pump (manufactured by Harvard Apparatus, Boston, MA) aspirated blood from the chamber outlet for a time interval of 300 seconds, at a controlled temperature of 37 °C, with a constant flow rate of $Q = 75$ μl/min, in order to achieve the physiological shear rate γ of

$$\gamma = \frac{6Q}{wh^2} = 1500\ s^{-1}, \tag{5.4}$$

where w and h are the width (500 μm) and the height (100 μm) of the channel section, respectively [117].

Optical and electrical data were simultaneously acquired during the blood perfusion through the microchannel, as schematically shown in Figure 5.4. Fluorescent bi-dimensional (2D) images were digitized in real-time with the

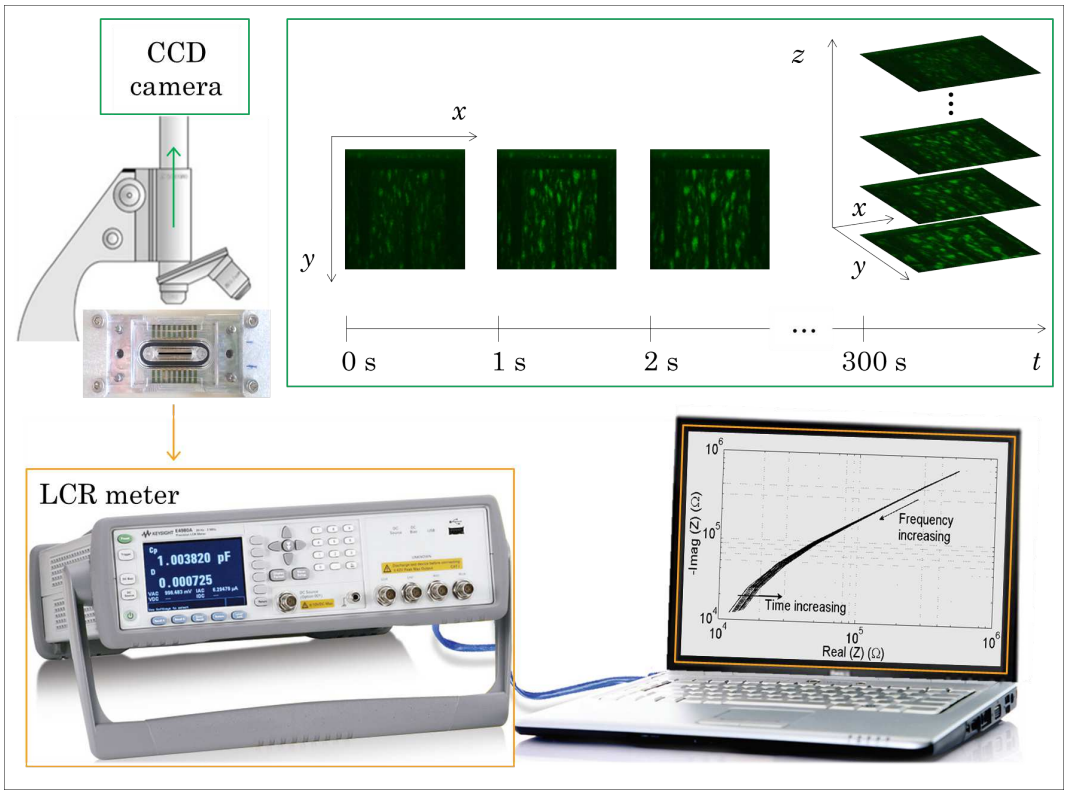

Figure 5.4: ***Measurement bench.*** *Optical 2D images have been obtained in real-time with the CCD camera of the microscope and at the end of the blood perfusion, at $t = 300$ s, a z-stack was acquired. Simultaneously, the high precision LCR meter measured the related impedance values.*

CCD camera (iXon^{EM}+, Andor^{TM} Technology) of the confocal microscope, whose internal sensor of 512 x 512 pixel detected the intensity emission of the fluorescent dye quinacrine that labeled platelets, in response of an excitation laser wavelength of 488 nm. In particular, each pixel in the digital images thus acquired carried an intensity information, represented by an integer in the interval [0, 255]. Regardless of the pseudo color representation, green in this

case, such images were composed exclusively of shades of gray, varying from black, the weakest intensity, to white, the strongest intensity). An appropriate laser power was set in order to achieve an adequate emission intensity, avoiding the pixel saturation in the CCD sensor. Taking into account the magnification determined by the optical path, for which 1 pixel = 0.33 μm, the investigation area resulted to measure 28547.48 μm^2. Images were collected during the dynamic experiment every second, for a total time of 300 seconds. The plane of acquisition in the confocal microscope, named focal plane, was identified as the plane where platelets adhered and the electrodes could be seen well focused. In this way, it corresponded to the bottom wall of the microchannel. At the end of perfusion, at $t = 300$ s, a sequence of N fluorescent images along the vertical z-dimension, called z-stack, was acquired with a z-step of $\Delta z = 0.5$ μm. The first plane acquired was the focal plane identified as the adhering base plane during the perfusion, while the last one detected was represented by the last plane where the aggregates tips were visible. As a consequence, each z-stack had a proper height $H_{z-\text{stack}} < h = 100$ μm, defined as

$$H_{z-\text{stack}} = (N-1)\Delta z. \tag{5.5}$$

The impedance measurements were performed using the high precision LCR meter in the frequency range [1, 300] kHz with eight logarithmically spaced steps and a 2-wires configuration. A drive voltage of 100 mV was chosen to avoid the redox reactions between electrodes and salts dissolved in plasma, since it was by far lower than the standard half-cell potential for gold, that is 1.5 V. In particular, the impedance data used for the thrombus volume reconstruction were extracted from the impedance magnitude measured at 150 kHz, because, at this frequency, the lipidic membrane of platelets behaved like insulators and platelets aggregation could be measured by evaluating the impedance increase, as represented in Figure 5.5. For this reason, at 150 kHz the impedance temporal variations resulted more distinct and evident, thus facilitating the signal processing and interpretation.

A total number of $n = 31$ experiments were conducted. All of them were analyzed to validate the real-time performances of the new biosensor during the perfusion, but only for 22 of them the thrombus volume was quantified from z-stacks, at $t = 300$ s. The remaining 9 experiments have not been analyzed, in terms of final volume, because in those cases the channel was empty or completely obstructed by the thrombi, thus altering the microfluidic conditions, as shown subsequently.

Most of the protocols for confocal imaging have to be based upon those developed over many years for preparing samples for the conventional microscope. A good starting point for the development of a new protocol for the confocal microscope and the new biosensor was a protocol for preparing the samples for conventional microscopy later modified for the confocal instrument. Most of the methods for preparing specimens for the conventional microscope were developed to reduce the amount of out-of-focus fluorescence. The confocal system undersamples the fluorescence in a thick sample as compared with

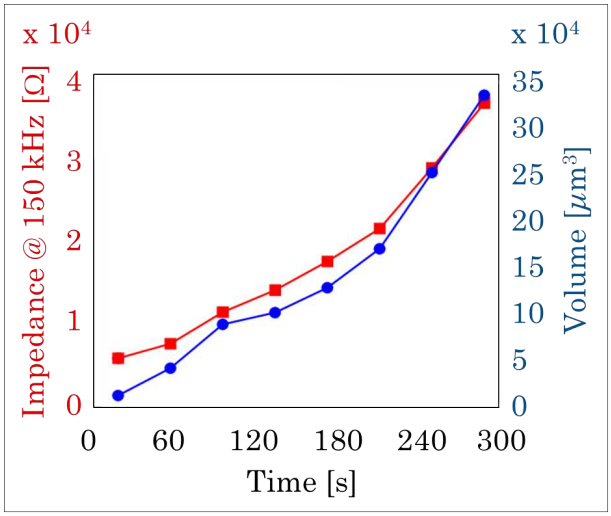

Figure 5.5: ***Impedance measurements evaluation at 150 kHz.*** *At this frequency the lipidic membrane of platelets behaved like insulators and the resulting volume could be measured by evaluating the impedance signal increase.*

a conventional microscope, with the result that samples may require increased staining times or concentrations for confocal analysis and may appear to be overstained in traditional microscopes. In order to register and to keep track of the experiments, with the aim of proposing and validating a new measurement protocol, the module shown in Figure 5.6 has been thought, created and used.

5.2.4 Thrombus volume estimation using confocal microscope

In order to have a reference measurement to evaluate the performances of the developed device, at the end of each experiment the thrombus volume was computed using the confocal z-stacks, as reported in literature [2, 38, 42]. In particular, for each z-stack, a value in the gray-scale [0, 255] was selected as threshold value Thr with the aim of separating all pixels in two groups: those that exceeded in intensity the threshold value and those that did not exceed it. Defining $f = 0.33$ μm/pixel as the conversion factor from μm to pixel, because 1 pixel = 0.33 μm, this method can be defined as optical thresholding (OT) and it allowed to extract the area A_i (μm^2) covered by the objects, with $i = 1, 2, ..., N$, for each of the N images in the z-stack as

$$A_i = \sum_{j=1}^{512} \sum_{k=1}^{512} \text{pixel}_{ijk\ (\text{intensity} \geq Thr)} f^2 \qquad i = 1, 2, ..., N \tag{5.6}$$

where pixel_{ijk} is the generic pixel of the z-stack located in the position $x = j$, $y = k$ and $z = i$, with $j, k = 1, 2, ..., 512$ and $i = 1, 2, ..., N$. The thrombus

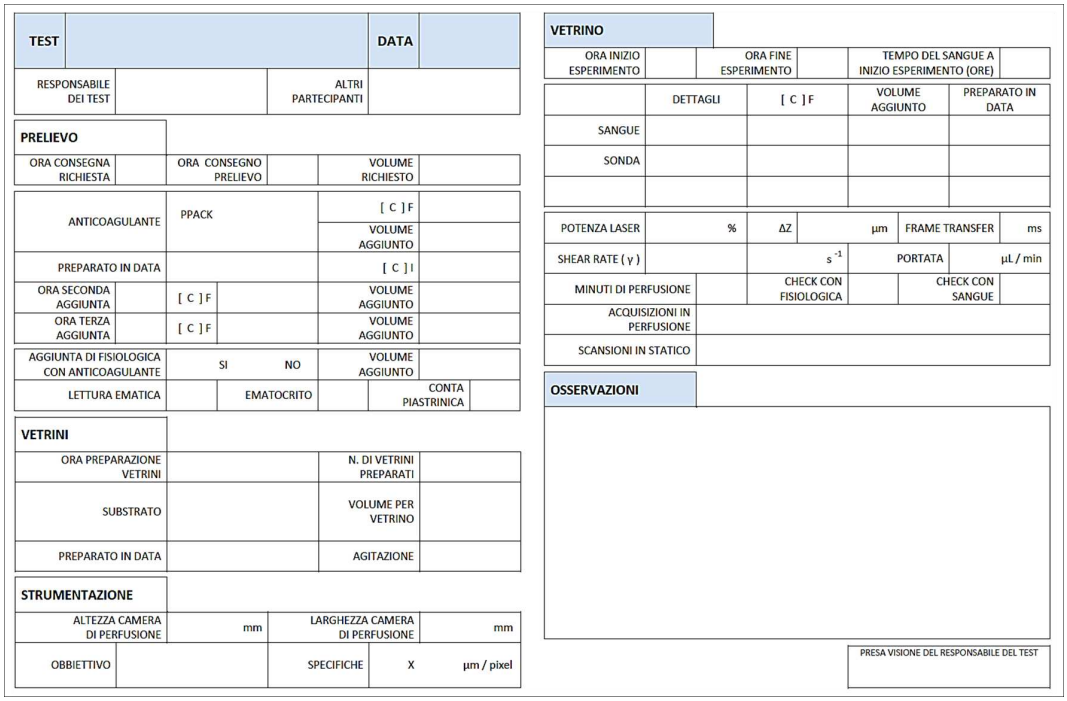

Figure 5.6: ***Measurement protocol.*** *All the experiments have been registered and tracked using a measurement protocol expressly designed and structured.*

volume V_{OT} (μm^3) related to the z-stack was then quantified as

$$V_{\mathrm{OT}} = \Delta z \sum_{i=1}^{N} A_i \tag{5.7}$$

Automatization of threshold extraction

With the purpose of compensating the subjectivity in choosing a threshold value, the proposal was a novel, fast and accurate thresholding method, an example of which is shown in Figure 5.7. The whole set of the gray-scale values [0, 255] was considered. With the thresholding method, for each z-stack acquired at $t = 300$ s, the volume V_{OT} and the maximum height H_{Max} reached by the thrombi were considered as functions of the threshold, varying from 0 to the maximum fluorescence value in the z-stack, F_{Max} , as shown in Figure 5.7a. Observing the curves relative to V_{OT} and H_{Max} it is evident that, lowering the value of the threshold integer starting from F_{Max}, H_{Max} gradually saturates to the value of $H_{z-\mathrm{stack}}$ and, correspondingly, V_{OT} diverges towards increasingly higher values (Figure 5.7a). This corresponds to a movement from a situation of underestimation of thrombus volume, with a not real small amount of low thrombi, to an overestimation state, with misrepresented overly huge thrombi. The optimal threshold value (e.g. 25 in Figure 5.7a) was identified and chosen as the point of saturation of the height curve, corresponding to the elbow point of the volume curve. The visual comparison between one of

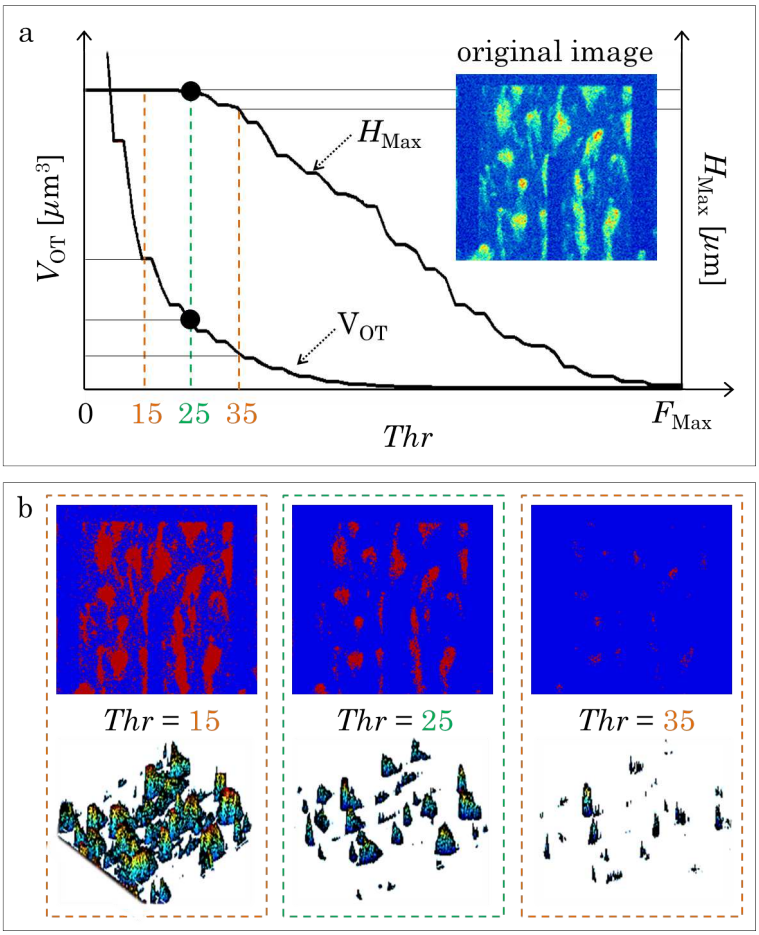

Figure 5.7: ***Automatic thresholding for thrombus volume quantification with confocal microscope.*** *The optimal threshold is always at the elbow point of the volume curve, corresponding to the point of saturation in the height curve. The absolute threshold values were given as examples (a). Binary mask representation and related 3D volume reconstruction, obtained with absolute threshold 15, 25 and 35, respectively. The absolute threshold values were given as examples (b).*

the original images, shown in Figure 5.7a, and the related area A extracted with three different threshold values (e.g. 15, 25 and 35 in Figure 5.7b) represents a graphical example of what just described. On one hand, lowering the threshold value with respect to the optimal value (e.g. 15 in Figure 5.7), the area A extracted leaded to reconstruct artifacts caused by the optical noise and thrombi appeared of square shape instead of pyramidal (Figure 5.7b, left panel). On the other hand, a thresholds higher than the optimal one (e.g. 35 in Figure 5.7b, right panel) leaded to an underestimation of the real thrombus height and volume. As shown, volume quantification and reconstruction was dramatically different if the threshold value differs, in terms of absolute integer in the range [0, 255], of $\pm$ 10 from the optimal one (Figure 5.7b, middle panel).

5.2.5 Volume estimation and reconstruction using the new device

Electrical impedance data and 2D optical images were acquired simultaneously, as stated. From impedance measurements and the related images, it was possible to reconstruct the 3D spatial and temporal distribution of thrombi using a specifically developed analysis tool, a graphical user interface (GUI), based on a finite-elements-like method [18,19,22] and represented in Figure 5.8. The electrical parameters of blood flowing in microchannel at high shear rates that have been used in the simulations can be found in [20,22], whereas the thrombus can be considered as a perfect insulator below a few hundreds of kHz. The geometry of the thrombi was reconstructed deducing a 3D solid model from the first 2D fluorescence image acquired and adjusting the 3D volume for every 2D image subsequently obtained. The thrombi height was assumed to be linearly proportional to the fluorescence intensity emitted from labeled platelets, as well established in literature [118], with respect to a unique heigth scale factor for all the pixels. The 3D solid model was thus derived with the graphical tool from fluorescence intensity values and the measured impedance. In particular, the tool shown in Figure 5.8 allows to automatically recognize the electrodes and the microchannel in the 2D images and to quantify the blood conductivity, whose difference from a patient to another one depends on the hematocrit concentration. Starting from the impedance measured at the beginning of the experiment in absence of thrombi, the heigth scale factor was iteratively modified until the simulated impedance matched the measured one [18, 22]. The thrombus volume thus quantified through the solid model

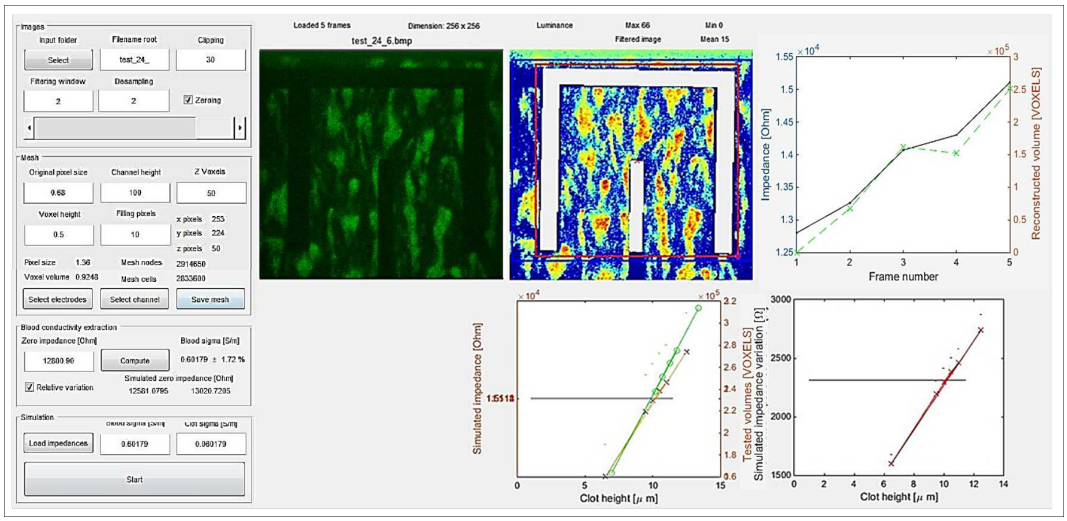

Figure 5.8: ***Tool to quantify the thrombus volume.*** *The GUI tool developed processes 2D images and identifies the shapes of the electrodes and of the channel.*

from impedance measurements is indicated as V_{IM}.

Analysis tool and fusion of electrical and optical data

The 3D steady-state current conduction analysis tool whose interface is represented in Figure 5.8 was expressly developed for this application. It was based on the discrete geometric approach on a pair of interlocked cell complexes where the current through electrodes has been assigned [22, 119, 120].

First, each image captured by the CCD camera was clipped to remove noise and desampled. Starting from the information about the shape of the electrodes and of the channel, together with the height of the channel, a cubical grid was constructed inside the selected computational domain. The thrombus geometry was thus easily obtained from the luminance information $L(p,t)$ of each pixel p at a given time instant t. In this case, with 8 bit images , the luminance reduced to the fluorescence intensity of each pixel. The linear system

$$G^T S G P = 0 \tag{5.8}$$

is assembled, where G is the standard edge-node incidence matrix, S is the Ohm's constitutive matrix [121–123] constructed by starting from the actual material distribution and P is the array of potentials attached to the nodes of the primal cell complex. Homogeneous Neumann boundary conditions were imposed on all the boundary of the domain. Each electrode was modeled as an equipotential surface characterized by an unknown potential. A non-local boundary condition was imposed on each electrode by setting the total current flowing through it. The linear system of Equation 5.8, with the non-local equations of [22], was then solved by an iterative linear and parallelized computation. Each simulation took less than 30 seconds.

The reconstruction of the thrombus geometry and volume was obtained through a novel inversion methodology based on optical and impedance data fusion at a given time instant. In particular, the geometry of the thrombus was represented by a solid model deduced from the fluorescence intensity extracted from the 2D images sampled with the microscope. Thus, for each pixel, the height H of the thrombus with respect to the slide surface was assumed to be proportional to the luminance $L(p,t)$, according to a scale factor k common for all the pixels, obtaining

$$H(p,t) = k(t) L(p,t) \tag{5.9}$$

where p is the generic pixel and t the generic time instant. The inverse problem was then related to the determination of $k(t)$ according to the minimization problem

$$\min_k |R_c(k,t) - R_m(t)| \tag{5.10}$$

where $R_c(k,t)$ is the resistance computed by using the forward solver and a scale factor k, whereas $R_m(t)$ is the measured resistance, according to a total time interval of 300 seconds. Therefore, to determine such a scale factor, a number of 3D steady-state current conduction analyses were performed with the developed forward problem solver by modifying the scale factor until the

computed resistance matched the measured one. The thrombus volume was then evaluated from the thrombus solid model. In practice, the luminance was normalized as

$$\bar{L}(p,t) = \frac{L(p,t)}{\max(L(p,t))} \tag{5.11}$$

and the height H of the thrombi was defined as

$$H(p,t) = \bar{L}(p,t)n\Delta z \tag{5.12}$$

where Δz was the height of each pixel and n was an arbitrary positive integer. Finally, the thrombus height on each image pixel was obtained by applying the floor function to $\bar{L}(p,t)n$, which from the Equation 5.12 was proportional to H.

Instead of exhaustively simulating all increasing multiples of the voxel height until the measured resistance is exceeded, the property of monotonicity of the resistance with respect to changes in conductivity σ [124] was used. Considering two distributions of conductivity σ_1 and σ_2 in the computational domain such that

$$\sigma_1 \leq \sigma_2 \qquad \forall p \tag{5.13}$$

then the resistance $R(t)$ fulfilled

$$R(\sigma_1, t) \geq R(\sigma_2, t) \tag{5.14}$$

In other words, the resistance monotonically increased when n, proportional to the thrombus volume, grew. Therefore, a bisection method had to be employed to solve the minimization problem, determining the thrombus height that better matched the measurements. That was, the algorithm repeatedly bisected the searching interval and selected a subinterval in which the solution had to lie for further iterative refinements. The electrical parameters of blood flowing in microchannels at high shear rates have been experimentally characterized in [22]. The blood conductivity $\sigma_{blood} = 0.33$ S/m used in the simulations was determined in each experiment from the initial resistance R_0 measured in absence of thrombi. The thrombus was considered as a perfect insulator below a few hundreds of kilohertz, as shown in [23] and in [17].

5.3 New algorithm to improve the accuracy in platelet thrombi volume measurement

5.3.1 Fluorescent beads preparation

Volume calibration was performed using yellow-green carboxylate-modified microspheres (2 μm diameter; Molecular Probes, Eugene, OR). The product was supplied as aqueous suspension containing 2 % solids and sodium azide (2 mM final concentration). Beads were ultraclean polystyrene microspheres coated

with a hydrophilic polymer containing multiple carboxylic acids for covalent attachment of ligands. Each sphere contains fluorescent dye molecules in its whole volume and shows little or no photobleaching, even when excited with the powerful illumination required for fluorescence microscopy.

Following the protocol suggested by Molecular Probes, the stock solution (with about 4.6 x 10^9 beads/ml) was diluted. Considering the planar experimental spreading of final fluid sample (1 cm^2, about 3500 fields of view), in order to obtain about 20 beads in each field of view, a total amount of 7 x 10^3 beads/μl was achieved in the suspended solution. Afterwards, a droplet of ProLong Diamond Antifade Mountant (Molecular Probes) was added onto a glass slide (Menzel-Gläser, Braunschweig, D), while a coverslip (Menzel-Gläser) with 1 μl of diluted solution was placed down on it. The sample was kept in the dark, at room temperature, for 24 hours.

5.3.2 Blood samples preparation

The procedure of preparing blood samples for the experiments was the same of that described before. In particular, for each experiment, 20 ml of venous blood from healthy volunteers were collected into PPACK 50 μM final concentration. Afterwards, 200 μl of acid-insoluble fibrillar type I collagen were homogeneously distributed onto a coverslip for 60 minutes. The coverslip was thus positioned in a flow chamber, forming the bottom wall of the artificial microchannel previously introduced, having a rectangular section of 500 x 100 μm^2. The fluorescent dye quinacrine was added to whole blood to label platelets. A syringe pump aspirated blood from the chamber outlet for a time interval of 3 minutes in order to achieve the physiological shear rate $\gamma = 1500\ s^{-1}$.

5.3.3 Confocal images acquisition and volumes measurement

The perfusion flow chamber was positioned on the stage of the same confocal laser scanning microscope described before, where the 40X oil-immersion objective mounted on the piezoelectric driver allowed the real-time digitalization of images with the CCD camera. The field of view area was 28547.48 μm^2. Confocal optical z-stacks were detected along the vertical z-dimension with a z-step $\Delta z = 0.2$ μm.

In order to evaluate the systematic errors in the benchmark measurements, confocal digital images were elaborated using ImageJ software [102], subjectively setting an intensity threshold to select the areas covered by the objects in all the images of a stack acquired along z-dimension. The volume was then measured as the sum of the detected areas in the images, multiplied by Δz [36–38, 40–42]. Adjusting the intensities histogram, volumes were quantified also with Volocity software (Perkin Elmer, Waltham, MA) in a similar

way [125].

Along the text all the results are expressed as mean ± standard deviation, each computed with $n = 10$ z-stacks. In order to identify significant differences among the results, the Student t-test was used.

5.3.4 Algorithm development for accuracy improvement

The proposed new algorithm was firstly applied to the images of known volume beads in order to achieve an accurate evaluation of its performances and to find an optimum value for the calibration factor. Consequently, it was applied to small aggregates to verify its robustness with non-spherical samples and finally to platelet large aggregates.

Images elaboration and signals extraction

For each z-stack (Figure 5.9a), a preliminary control was performed to exclude sequences of images with saturated pixels. For this scope, the maximum intensity projection (MIP) of all the values (Figure 5.9b) was extracted and visualized. The MIP is a fast method that projects in the visualization plane the maximum intensity that falls in the pixels along each ray traced parallel to the z-axis. In this way, two MIP renderings from opposite viewpoints are symmetrical images if they are rendered using orthographic projection. The identification and the visualization of the maximum value that each pixel assumes along the z-dimension represents a widely used technique in diagnostic imaging.

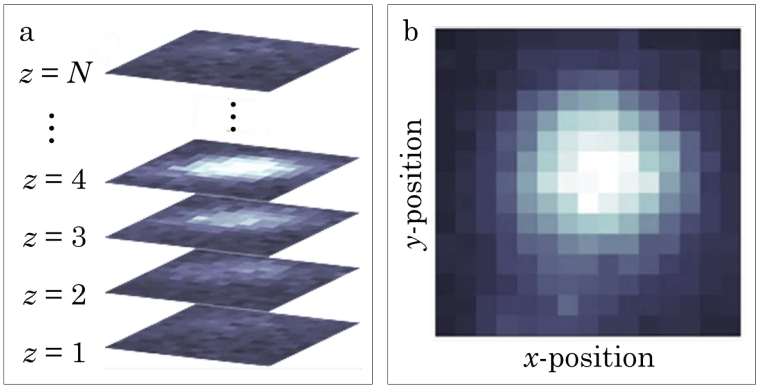

Figure 5.9: ***Images acquired.*** *Example of a z-stack of N images acquired along the z-axis with the confocal microscope (a). Maximum intensity projection related to the z-stack saved. Each pixel intensity in the MIP is the brightest among all the pixels met along along the ray parallel to the z-axis (b).*

Afterwards, for each stack, a three-dimensional (3D) matrix was defined. The x-position and the y-position of each pixel were assigned to the first and the second dimension of the matrix, respectively, while the intensity values

of each related pixel assumed along the z-axis were allocated in the third dimension of the matrix, starting from the fluorescence value computed in the first slice, $z = 1$, and going on until the value of the last slice, $z = N$. An example of the graphical representation of the matrix is shown in Figure 5.10. According to the CCD square sensor physical dimension, with $d = 512$ pixel as side, and to the number N of slices acquired for a stack, the matrix had dimension d x d x N.

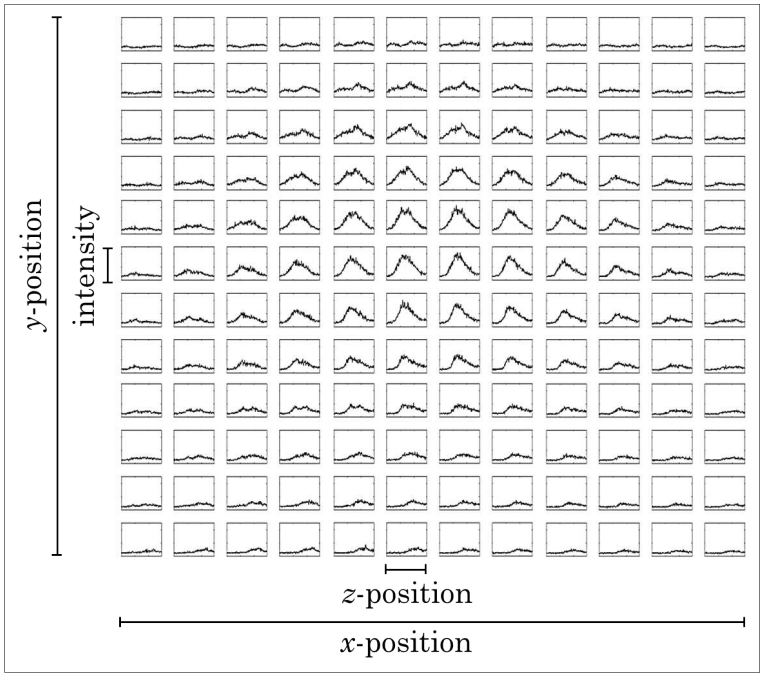

Figure 5.10: ***Example of 3D matrix defined for each z-stack.*** *The x- and the y-position of each pixel were assigned to the first and second dimension, respectively, while the N intensity values of each related pixel assumed along the z-axis are located in the third dimension.*

Since the intensities along the z-dimension were affected by noise, they have been locally smoothed with a finite impulse response (FIR) low-pass filter with the aim of compensating the high frequency noise. According to the necessity of regularizing the z-intensities without losing information the smoothing filter was designed with 13 coefficients and applied to each intensity z-signal, performing a weighted mobile averaging. As illustrated in Figure 5.11, centering the kernel of coefficients in every z-position, the associated smoothed value s_z was obtained from the neighboring original values v_{z+i}, with $z = 1, 2, ..., N$ and $i = -6, -5, ..., 0, 1, ..., 6$, as

$$s_z = \frac{\sum_{i=-6}^{6} v_{z+i} c_i}{\sum_{i=-6}^{6} c_i} \qquad z = 1, 2, ..., N \tag{5.15}$$

where c_i are the coefficients of the filter (Figure 5.11). Hence, in order to ac-

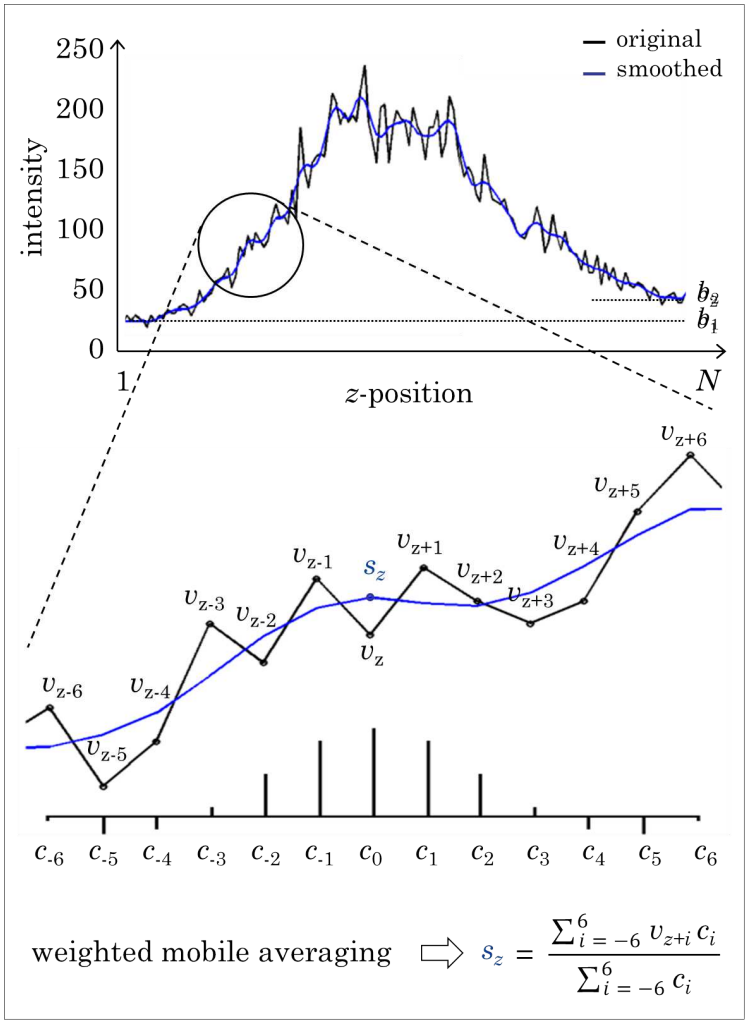

Figure 5.11: ***Smoothing of the intensity signals along the z-dimension.*** *Intensity smoothing by means of the low-pass FIR filter that allows obtaining the filtered signal s_z. Two values of background, b_1 and b_2, are quantified for every z-signal as average of the first and the last six intensity values of the signal, respectively.*

complish the limits that occur regularizing the first and the last samples of a generic signal with a kernel of coefficients [126] and to consider the variability of the background fluorescence in all the three dimensions, two values of background, b_1 and b_2, shown in Figure 5.15, were quantified for every intensity z-signal as average of its first and last six intensity values, respectively.

For every z-stack and its related 3D matrix, a binary mask was defined (Figure 5.12a), whose dimensions were the x- and the y-position of each pixel and, consequently, were connected to the first and the second dimension of the related three-dimensional matrix defined before. The value 1 was assigned to every pixel whose maximum intensity M in z-dimension reached a specific threshold over its background b_1 (Figure 5.16b). The threshold, automatically obtained, is adaptive because the intrinsic variability of biological samples

behavior in light emission does not allow to set a fixed intensity threshold. Considering as reference value the maximum intensity peak M_{x_M,y_M} among all the intensity peaks in the three-dimensional matrix (Figure 5.12a and Figure 5.12b), each pixel intensity value in the binary mask was set to 1 if the related intensity peak M over its background b_1 reached at least 1/3 of the reference value $M_{x_M,y_M} - b_{1\ x_M,y_M}$, as indicated in the Figure 5.12. Structuring the binary mask as described, it was possible to identify only the x- and the y-positions related to a real presence of volume, excluding those affected by background, noise and artifacts. The expression used to define the binary mask was

$$\text{mask}_{j,k} = \begin{cases} 1 & \text{if } \frac{M_{j,k} - b_{1\ j,k}}{M_{x_M,y_M} - b_{1\ x_M,y_M}} > \frac{1}{3} \qquad j,k = 1,2,...,d \\ 0 & \text{otherwise} \end{cases} \tag{5.16}$$

where j and k are the indexes identifying the generic x- and y-position, respectively. Accordingly, Figure 5.12c gives an example of a selected pixel, to which the value 1 was assigned because its z-signal had a peak of intensity M that raised over the threshold $1/3(M_{x_M,y_M} - b_{1\ x_M,y_M})$. Alternatively, in Figure 5.12d an example of a pixel excluded is visible, where the z-signal did not overpassed the threshold. Figure 5.13 illustrate three examples of valid pixel selection in the 3D matrix. As already said, the x- and the y-position of each pixel of the original images and of the binary mask were associated to the first and the second dimension of the related 3D matrix. Assigning in the binary mask the value 1 to the pixels that overpassed the threshold defined (pixels colored in red in the binary masks in Figure 5.13), only the valid pixels in the 3D matrix were considered for the volume measurement. This means that only the z-signals in the 3D matrix related to the x- and the y-positions selected through the binary mask definition have been processed to extract the volume associated. The other pixel were excluded from the successive computations because affected by background, noise and artifacts.

Calibration of elongation and realistic volume estimation

After having applied the binary mask to the three-dimensional matrix, a bi-dimensional matrix was initialized to attribute to every pixel the height of the volume portion there located. Referring to Figure 5.14, the positions z_1 and z_2 defined the distance $D = z_1\text{-}z_2$ that had to be calibrated accordingly to their related signal of intensities. For each intensity signal z_1 and z_2 were measured starting from the first level of background b_1, advancing forward along the signal, and from the second value of background b_2, moving backward. Considering the intensity gaps $d_1 = M - b_1$ and $d_2 = M - b_2$, the two points along the z-axis were chosen as the z-positions whose intensity reached an elevation of $d_1/10$ and $d_2/10$, respectively. The height of the volume portion for each x- and y-position was first quantified as the product of the z-distance D with the ratio between the intensity peak and the maximum among all the intensity peaks, related to their background values. Afterwards, the quantity thus

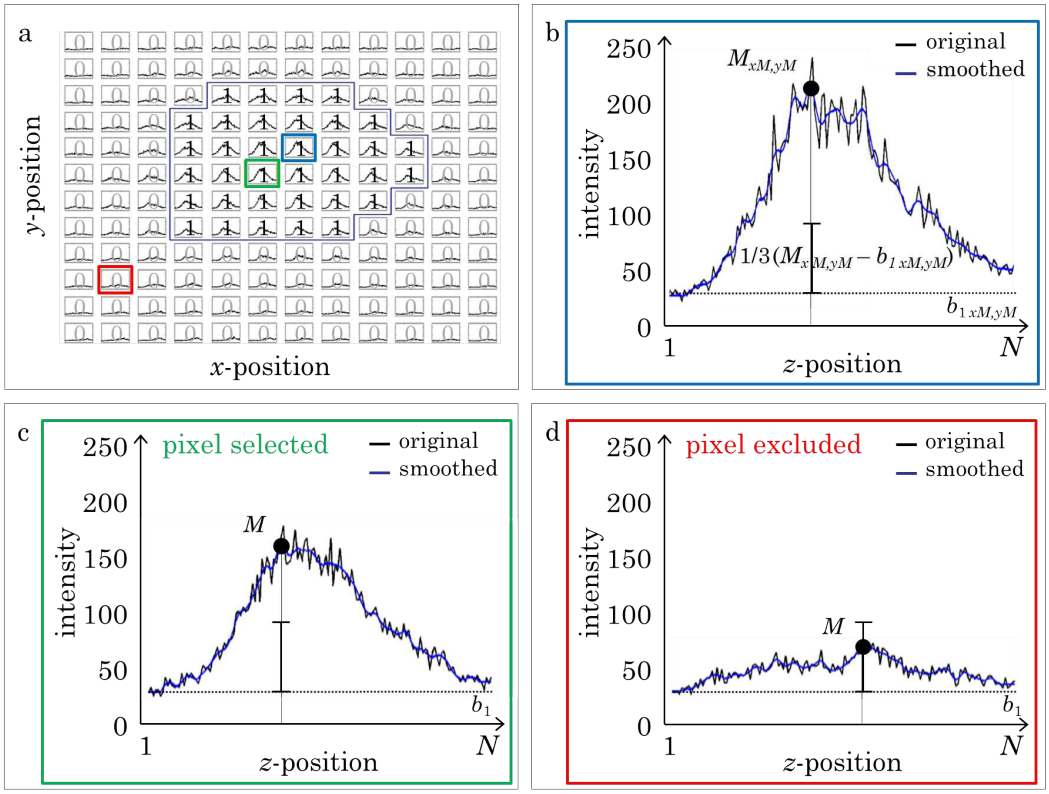

Figure 5.12: ***Binary mask definition.*** *Graphical representation of the 3D matrix defined for a sequence of images after applying the binary mask (a). The adaptive threshold was set considering 1/3 of the elevation of the maximum peak M_{x_M,y_M} over its background $b_{1\ x_M,y_M}$ (b). Example of a selected pixel, whose z-signal shows a peak of intensity M that raised over the threshold $1/3(M_{x_M,y_M} - b_{1\ x_M,y_M})$ (c). Example of a pixel excluded because its related z-signal did not go beyond the threshold (d).*

obtained was multiplied by an experimental estimated optimal factor $\hat{C}$. The heights $h_{j,k}$ associated to each x- and y-position were evaluated as

$$h_{j,k} = \hat{C} D_{j,k} \frac{M_{j,k} - b_{1\ j,k}}{M_{x_M,y_M} - b_{1\ x_M,y_M}} \qquad j,k = 1,2,...,d \tag{5.17}$$

where h and D are expressed in μm and $\hat{C}$ is the optimal calibration factor, obtained through an iterative computation applied on beads stacks in order to satisfy, at the same time, a z-dimensional condition and a volumetric condition, as specified as a result. The described calibration model was applied to small platelets aggregates and finally to more complex aggregates. According to the physical dimension of a pixel $r = 0.33$ μm, the expression for the final total platelet thrombi volume V of a stack was quantified as

$$V = r^2 \sum_{j=1}^{d} \sum_{k=1}^{d} h_{j,k} \qquad j,k = 1,2,...,d \tag{5.18}$$

where the result is expressed in μm^3. The graphical representation of the

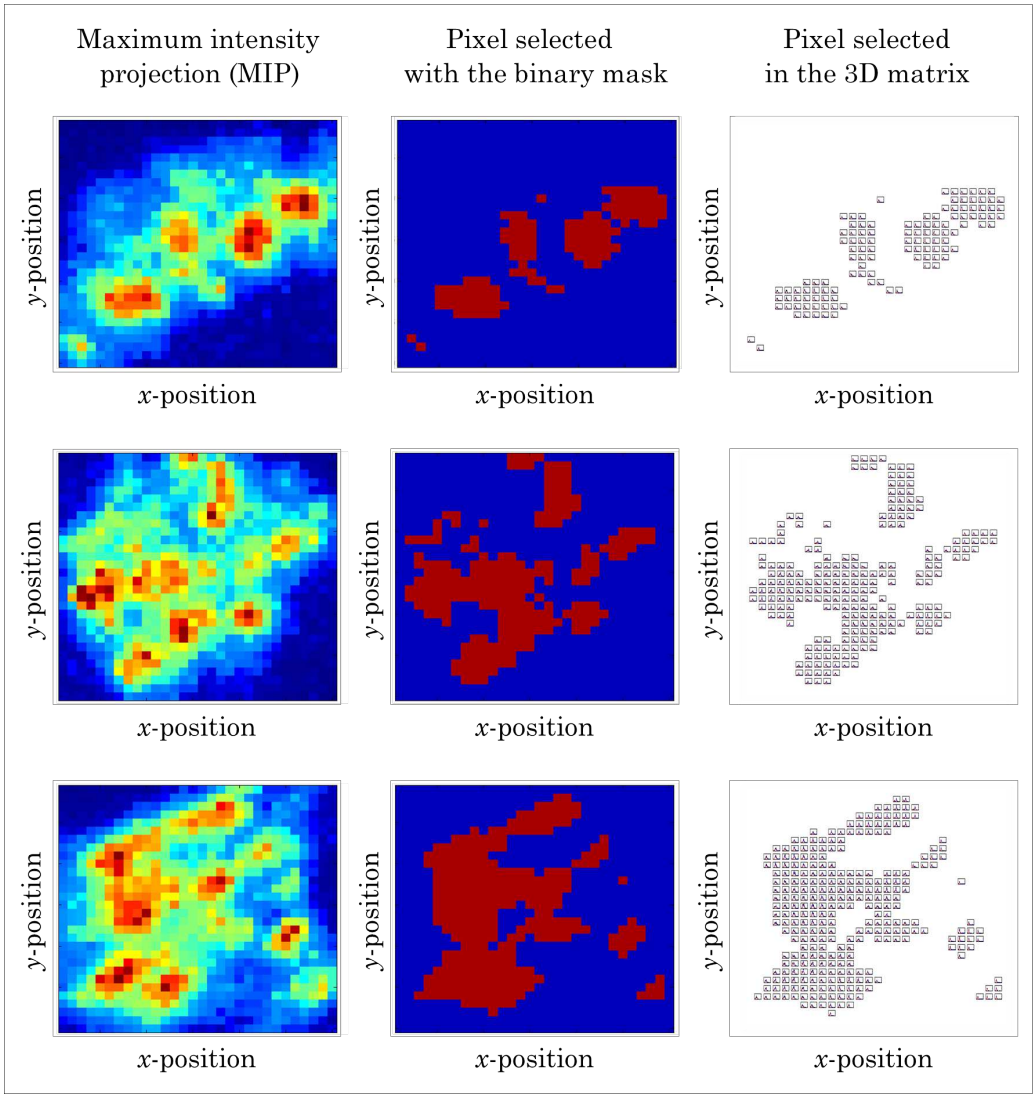

Figure 5.13: ***Examples of valid pixel selection.*** *Three examples of maximum intensity projection (MIP), in which small aggregates of platelets are visible, with the related binary mask and the corresponding pixel selected in the 3D matrix. Only the z-signals in the 3D matrix related to the x- and the y-positions selected through the binary mask definition have been considered to measure the volume.*

assignment of heights to each pixel, in order to obtain a volumetric 3D reconstruction starting from a bi-dimensional image, is simply shown in Figure 5.15.

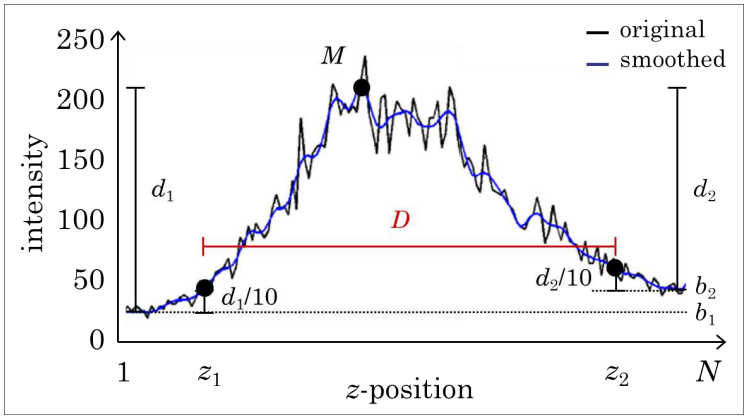

Figure 5.14: ***Calibration of z-elongation.*** *The axial distance D along z-dimension was defined for each z-signal, thus for each x- and y-position. The two z-points z_1 and z_2 have been identified as the points whose intensity reached at least the 10 % of the related intensity peak M, with respect to the background values b_1 and b_2.*

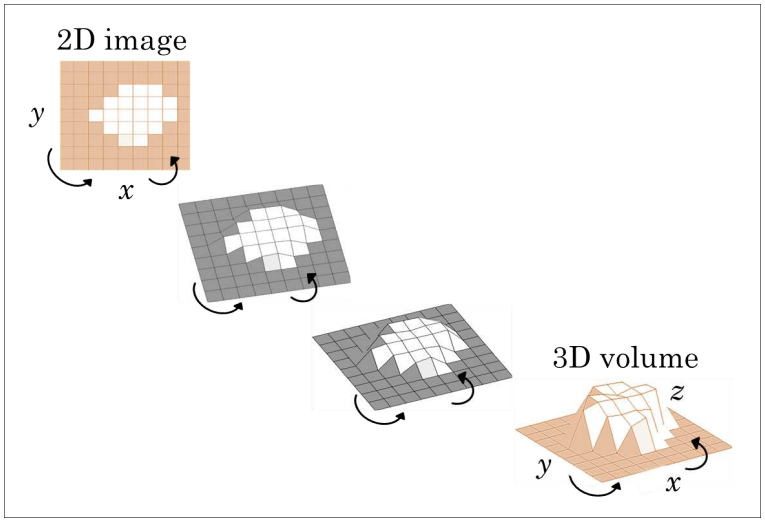

Figure 5.15: ***Example of a solid 3D volume obtained from a 2D image.*** *For each x- and y-position, so for each pixel in the image, the height of the volume portion there located was estimated obtaining a 3D solid reconstruction.*

5.4 Blood components characterization as quality control in the pre-analytical phase

5.4.1 Blood components extraction

For each experiment, 3 ml of venous blood were collected from healthy blood donors into citrate as anticoagulant (hematocrit of 38 ± 3 %. Informed written consent have been obtained from healthy blood donors according to the Declaration of Helsinki and the DMS of the Italian Ministry of Health, Novem-

ber 2_{nd}, 2015, (quality and safety about blood and blood donors). The Ethics Committee CRO-IRCCS Aviano approved the study. Afterwards, each vial of whole blood was divided in three parts, with the aim of obtaining the materials of Figure 5.16a. One part of whole blood (1 ml) was left untreated (whole blood in Figure 5.16a). Another part of whole blood (1 ml) was centrifuged to obtain, as shown in Figure 5.16b, plasma (liquid substance with all the coagulation proteins, but without cells) and whole concentrated blood (red cells, white cells and platelets, with an hematocrit of 60 $\pm$ 3 %). Finally, in the last part (1 ml), $CaCl_2$ (5 mM final concentration) was added to stimulate the coagulation process and to obtain serum (liquid substance without cells and without coagulation proteins) and the red clot (red cells, white cells, platelets and fibrin). The serum thus extracted can appear yellow (serum in Figure 5.16a) or it can show pale red shades (serum with low or high hemolysis in Figure 5.16a, Figure 5.16c and Figure 5.16d), a visible indication of the presence of hemolysis, due to red blood cells damaged. In addition, serum can sporadically contain fibrin white clots. If the serum expresses hemolysis, the white clot can contain fragments of red blood cells damaged and it looks light red (white clot with hemolysis in Figure 5.16a). These anomalous situations, not always identifiable by eye, can lead to technical problems and measurement interferences if not rapidly recognized. An example of different amounts of hemolysis in serum samples is shown in the Figure 5.17.

5.4.2 Biosensor design

The first step in this project was to propose a prototype fast and easy to be used, made with materials that were at disposal. The aim was to test the feasibility of the initial idea without initial costs, with the simplest sensing module among all those projectable.

First sensing prototypes

The first sensor was thus realized as a capacitor with parallel planar surfaces, shown in Figure 5.18. The capacitive sheets, made of copper, measured 20 mm in width and 1 mm in height, indicated as w in the Figure 5.18a, and h in the Figure 5.18b, respectively. Thinking the sensing module as a capacitor with surfaces placed in parallel respect to the measurement bench, on the first surface a plastic sheet was fixed. The result was a dielectric layer 0.35 mm high, named with letters h_d in the Figure 5.18a, with a disk shape hole of 7.5 mm of diameter, indicated as d in the Figure 5.18b. A polycarbonate holder at the bottom and a polycarbonate bar on the top of the capacitive surfaces allowed the stable positioning and the assembling of the capacitor, as illustrated in Figure 5.18b and in Figure 5.18c.

The sensor has been designed to horizontally deposit, in an easy and simple manner, a little droplet of the blood component to be measured. Figure 5.19 an example is given about the droplet deposition of blood plasma, whole blood

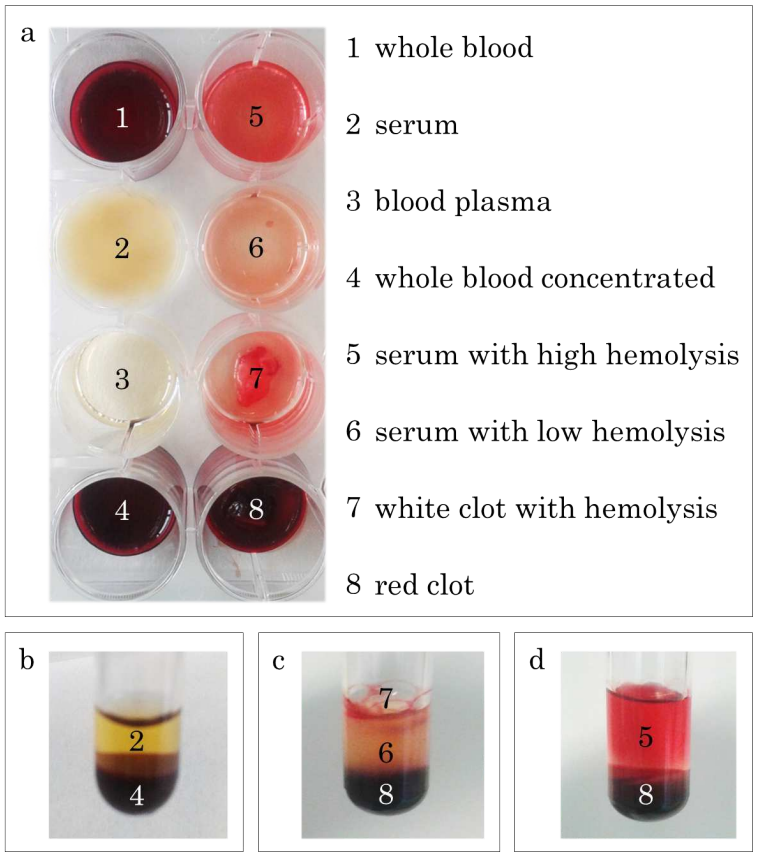

Figure 5.16: ***Blood components characterized with impedance measurements.*** *Components disposed in plastic wells (a). Whole blood centrifuged (b). Blood coagulated and centrifuged, with serum showing low (c) and high hemolysis (d).*

Figure 5.17: ***Serum samples.*** *Different amounts of hemolysis in serum samples, leading to to technical problems and measurement interferences.*

and red clot, on the left, in the middle and on th right, respectively. Working with very small volumes, on one hand there was a gain in terms of the quantity of sample to be used, thus permitting and allowing repeated tests with minimum invasiveness. However, on the other hand, it was necessary to carry out many fluid deposition tests to evaluate the optimal quantity to be used in the measurement phase and the structural seal capacity of the device. For each

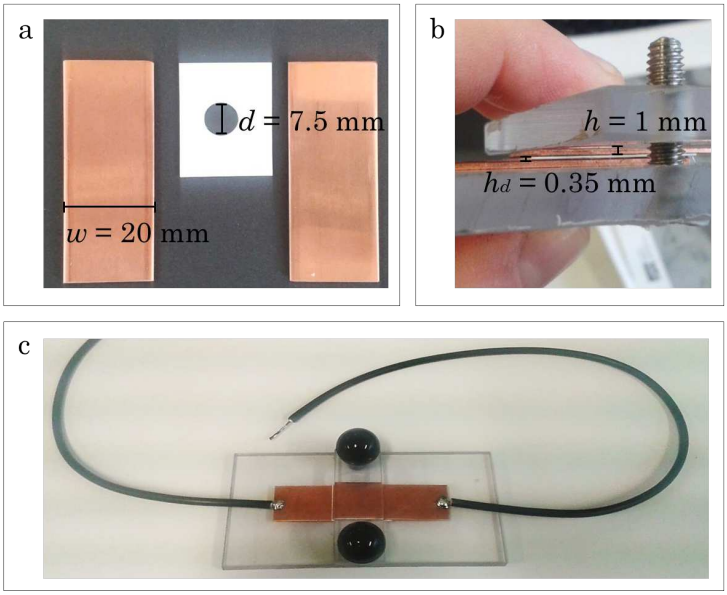

Figure 5.18: ***The first prototype.*** *Copper surfaces and dielectric layer made of plastic (a). View of the assembled layers (b). A polycarbonate holder at the bottom and a polycarbonate bar on the top of the capacitive surfaces allowed the stable positioning and the assembling of the capacitor(c).*

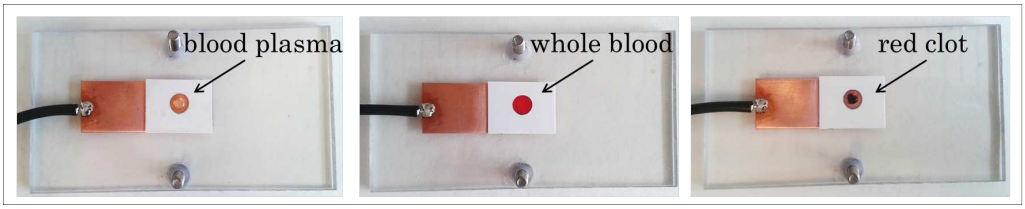

Figure 5.19: ***Droplet deposition.*** *Example of deposition of blood plasma, on the left, of whole blood, in the middle, of red clot, on the right.*

substance to be characterized, several tests of deposition, assembly, measurement and reopening have been performed, in order to evaluate if temperature or pressure could lead to the leakage of the component disposed in the disk during the measurement procedure. Repeated and prolonged measurements were performed at different frequencies to evaluate also the effects of temperature and pressure prolonged in time. Starting from the consideration that an optimal component quantity to be deposited could be that corresponding to the internal volume of the dielectric $V = \pi(d/2)^2 h_d \simeq 15$ mm^3, the deposition tests have been performed with 14 μl, 15 μl and 16 μl of substance. An example of blood plasma droplets is shown in Figure 5.20a, while Figure 5.20b represents the results obtained with a droplet of 15 μl. This quantity was finally chosen as optimal accettable quantity because because able to spread throughout the measurement disk without leaking out of it.

Despite the first measurements confirmed the potential and feasibility of this approach, the next choice was the increase of measurement sensitivity by

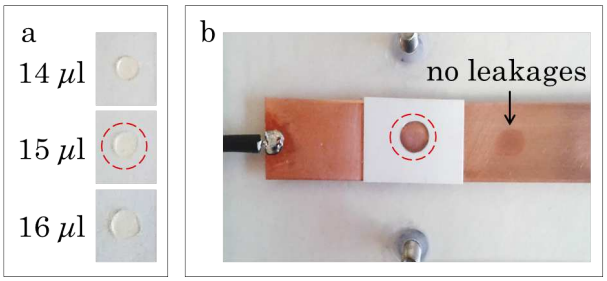

Figure 5.20: ***Droplet deposition test.*** *Blood plasma droplets (a). The quantity of 15 μl (dashed red circle) was chosen to perform measurements because able to spread throughout the measurement disk without leaking out of it (b).*

reducing the conductive surfaces that, unfortunately, led to the acquisition of unstable parasitic signals and noise. Thus, another copper sensing module was realized, by which measurements were made by conductive wires instead of large surfaces. The promising results gave the suggestion to join together the geometry of a capacitor with the accuracy and the sensitivity of reduced measurement surfaces, thus realizing the new device, immediately after described and used to perform fast and useful quality control evaluations of blood components.

New device description

Each blood component was homogeneously disposed in a single well (200 μl of substance, well diameter: 16 mm) and their electrical impedance was measured through a low cost, small and reproducible sensing module with a simple geometry (Figure 5.21a). The sensing module appears as a capacitor with parallel planar surfaces made of copper (width: 7 mm, distance between surfaces: 4 mm). A polycarbonate cap supports the accurate positioning of the capacitor in the blood substance (as schematically shown in Figure 5.21a and Figure 5.21b) and, consequently, maintains the stability of measurements.

5.4.3 Electrical impedance measurements and data analysis

The device was connected to a high precision LCR meter [83], in order to perform impedance measurement in the frequency range [100 Hz, 2 MHz], with twenty logarithmic spaced steps. A drive voltage of 50 mV was chosen, taking into consideration the electrochemical properties of materials and the open-short calibration was applied with the purpose of reducing the parasitic effects.

The equivalent circuit is presented in Figure 5.22. It allowed a satisfactory fit and correlation between experimental data and the physical processes that govern the system. The double layer at the interface was represented by CPE_1, characterized by a capacitance C_1 and a phase shift ψ_1, whose impedance is

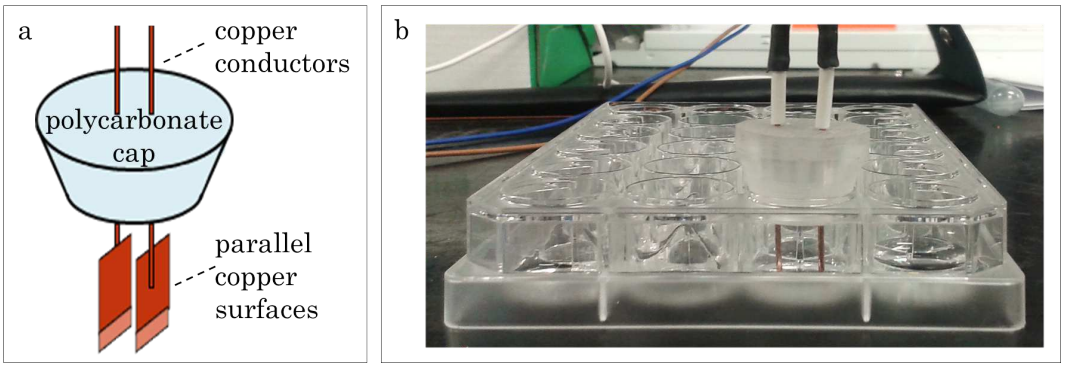

Figure 5.21: ***Biosensor for electrical impedance measurements.*** *The sensing module appears as a capacitor with parallel planar surfaces made of copper (a). Through a polycarbonate cap, the capacitor is placed on each well and immersed in the material to be measured (b).*

$Z_{\mathrm{CPE}_1}(\omega) = 1/[C_1(j\omega)^{\psi_1}]$. Besides, according to the purely resistive behavior of the extracellular fluid and considering the necessity of representing different cellular and membrane conditions with a generalized and versatile circuit element, blood was modeled in terms of a parallel of a resistance and a CPE. The CPE_2 models the cells with their membrane, it is characterized by a capacitance C_2 and a phase shift ψ_2 and exhibits and impedance $Z_{\mathrm{CPE}_2}(\omega) = 1/[C_2(j\omega)^{\psi_2}]$, while the resistance R represents the fluid in which cells are suspended.

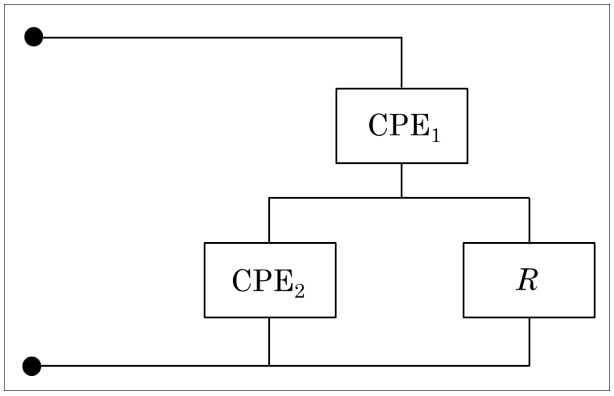

Figure 5.22: ***Equivalent circuit for blood components characterization.*** *The double layer at the interface was represented by the* CPE_1*, while blood was modeled with the parallel of the resistance* R *and another* CPE, CPE_2*, reflecting the behavior of cells and their membranes.*

The blood of $n = 20$ different donors, equally distributed among male and female, was collected and analyzed obtaining impedance signals varying with frequency and stable in time. In addition, the hematocrit was measured for all the blood samples with a commercial instrument, commonly and daily used in clinical laboratories.

The results have been represented with both magnitude and phase Bode diagrams and with Nyquist plot. Accordingly, to achieve a complete characterization of the system to be measured, the equivalent circuit fitting routine LEVM was used for further analysis of the impedance results [127]. It is an extensive and powerful complex nonlinear least squares (CNLS) program for fitting, simulation, and inversion of frequency and time domain data sets, optimized for analyzing electrochemical, dielectric and conductive system data.

5.5 Software development for live cells imaging: FluoLab

FluoLab is able to extract different metabolic signals from dissimilar cell types (e.g. platelets, megakaryocytes, mesenchymal cells). Software utilization starts from acquired fluorescence images, with the possibility to load images of different dimensions and formats. The graphical user interface (GUI) FluoLab is whown in Figure 5.23. The software has been designed to analyze contem-

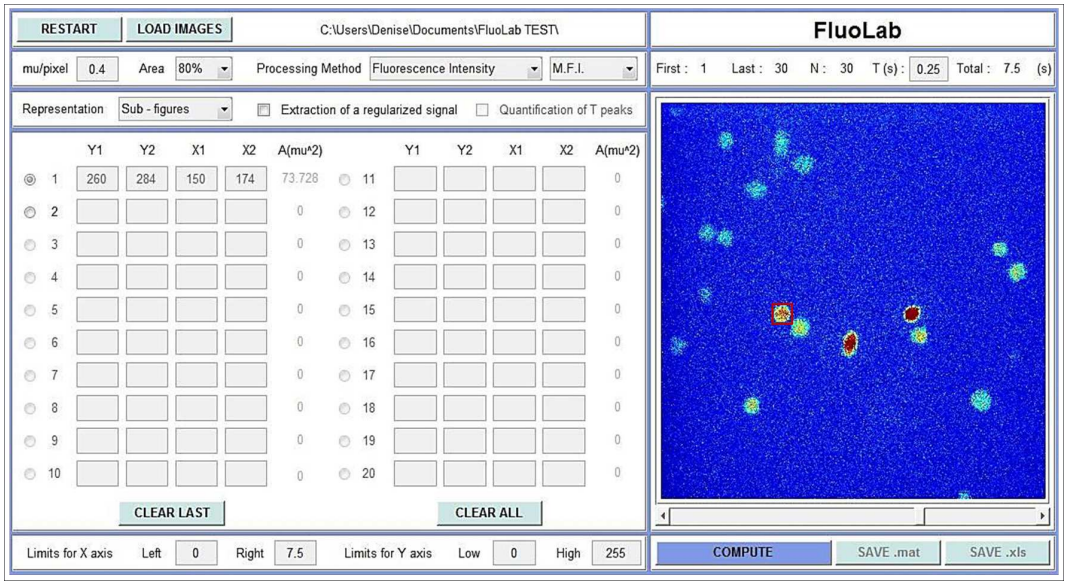

Figure 5.23: ***The graphical user interface (GUI) FluoLab.*** *The software appearance on the screen, with the possibility to load images, to select the regions to be analyzed and to regularize the signals and to extract them.*

poraneously until 20 different object for each image and to follow the region signals in time, compensating automatically the background. FluoLab allows the calcium signal extraction and analysis in a fast way, step by step in its metabolic evolution. First of all, it computes the calcium concentration combining in a single formula each pixel fluorescence intensity, the maximum and the minimum fluorescence value of each ROI, F_{Max} and F_{Min} and the dissociation constant K_d, for each kind of fluorescent probe (FLUO 3-AM, RHOD-1,

RHOD-2, TMRM). Then the software allows the filtering of calcium spurious spikes regularizing or smoothing the signals, if chosen. The software leads to the extraction of signals in terms of mean fluorescence intensity (MFI) with the possibility to convert automatically them in concentration values [μM]. In particular, in order to quantify the MFI of a cell at each time instant, thus obtaining a signal, in every 2D image the sum of all the pixel fluorescence values in the related ROI was measured, the background subtracted and the resulting value divided for the pixel total number in the ROI, in order to achieve a mean representative fluorescence value MFI from 0 to 255. In addition, with the aim of analyzing the cytosolic calcium concentration in different conditions, the fluorescence data thus computed, related to the FLUO 3-AM emission intensity, can be converted in calcium concentration values $[Ca^{2+}]_i$, for each time instant i, as reported in literature using the equation

$$[Ca_i^{2+}] = K_d \frac{F_i - F_{\text{Min}}}{F_{\text{Max}} - F_i} \tag{5.19}$$

where K_d is the dissociation constant of the interaction between FLUO 3-AM and Ca^{2+} (864 nM at 37^{o}C), F_i is the measured representative fluorescence MFI of the single platelet at the instant time i, F_{Max} is the fluorescence intensity of the single platelet treated with the ionophore Ca^{2+} A23187 (Sigma Aldrich, 10 μM final concentration) in the presence of 2 mM of $CaCl_2$ and F_{Min} is the fluorescence intensity of the unstimulated single platelet. The $[Ca^{2+}]_i$ of the resting state was calculated in single platelets in which the fluorescence intensity in each of at least 10 consecutive frames was within the 15 % of the value in the first frame and < 200 nM. At the same time, in order to investigate the correlation of the cytosolic calcium with the mitochondrial one and according to the different dimensional scale of their magnitude, the fluorescence data related to FLUO 3-AM and RHOD 2-AM were compared and expressed in terms of units comprised between 0 and 255. The fluorescence intensity variations were monitored from the beginning to end of the analysis period. The data obtained can be saved and a usable file is generated for a fast off-line data elaboration, visualization and analysis.

A common approach to image analysis is to use imaging software to segment those regions that will be analyzed. For small data sets, this is sometimes accomplished by simply outlining a region of interest ROI manually. This can be cumbersome for larger sets of data, and there are a variety of automatic methods for defining a ROI, but in this case the biologist or the physician purposely mantains its possibility to define the extremes of the tangent ROI. Thus, FluoLab leaves the freedom to the user to choose and define the specific local or global ROI (e.g. groups of cells, a whole cell, nuclei, mitochondria, granules, exosomes) from which it is possible to obtain automatically a signal related to that region, in order to be able to decide to select and analyze objects also sometimes overlapping (Figure 5.24a), or of different types, differently colored, with a different spatial hierarchy (Figure 5.24b), at the same time. This contemporary selection is not proper of other common computer programs.

Once selected, these regions can thus be further analyzed or classified based on properties such as shape and size or signal characteristics.

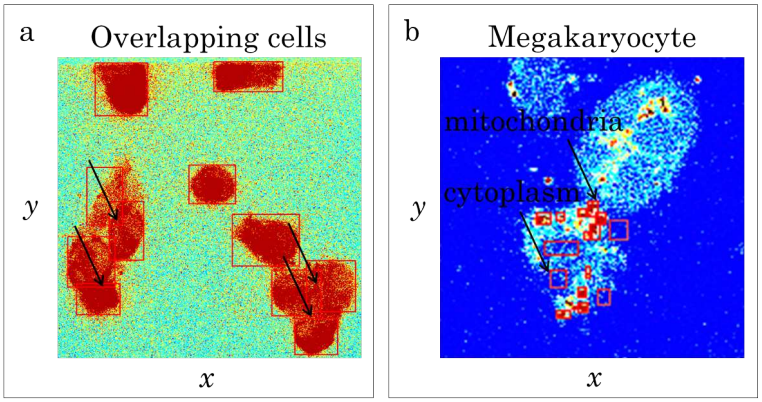

Figure 5.24: ***Advantage in the regions definition by the user.*** *Cells overlapping, not individually recognizable from common computer programs (a). Example of a contemporary selection of active mitochondria and regions of the cytoplasm related to a megakaryocyte (b).*

6. Results

The outcomes and the numerical results will be presented, likewise in the previous chapter, in relation to the different projects conduced. In particular, for the first biosensor, the results regarding the real-time monitoring, detection and prediction of the thrombotic profile will be introduced, with the evaluation of the compatibility between volumes obtained with the optical thresholding and from impedance measurements. Then the improvements in volumes estimation accuracy due to the new algorithm will be presented, with a successive evaluation of the uncertainties related to volume quantification from confocal z-stacks with the optical automatic thresholding and with the new approach. Afterwards, the results regarding the biosensor for the quality pre-analytical controls will be highlighted with, finally, the outcomes obtained with the new software for the live cells imaging.

6.1 Real-time individual thrombotic profile monitoring and prediction

A total number of 31 perfusion experiments were performed for a duration of 300 seconds. During each experiment, the CCD camera acquired 2D images at 1 frame per second, for a total number of 300 images and, simultaneously, the new device acquired impedance data. At the end of perfusion, thus at t = 300 s, a z-stack was acquired in order to evaluate the accuracy of the volume estimation provided by the new device here presented. The new device performances are shown, starting from thrombus parameters evaluation, passing to the real-time identification of unstable thrombi, and finally showing the comparison between the volume estimated with optical thresholding V_{OT} and from impedance measurements V_{IM}, with their 3D geometrical reconstruction.

6.1.1 Thrombus geometrical and electrical parameters estimation

Accordingly to the acquisition criteria of confocal sections along z-dimension, the maximum height reached by the thrombi resulted $H_{z-\mathrm{stack}} = 43 \pm 7$ μm ($n = 31$). Blood conductivity was estimated as $\sigma_{\mathrm{blood}} = 0.59 \pm 0.19$ S/m, at

a measured hematocrit percentage of 42.60 ± 1.98 %, values that appear perfectly in agreement with previously published data [128, 129]. This quantity was estimated by the analysis tool, starting from the impedance value at the beginning of each experiment, when no thrombus was formed. The thrombus conductivity should be, in this frequency range, ideally zero. However, thrombus is not a full solid geometry but it is an agglomerated structure of platelets with many interstitial spaces filled with plasma, that is conductive. From this observation, an experimental analysis was conducted, assigning a value to thrombus conductivity as a fraction of blood conductivity. The best results in terms of fit between V_{OT} and V_{IM} were obtained by setting the thrombus conductivity in the order of one eighth with respect to blood conductivity. The thrombus conductivity thus resulted to be $\sigma_{\mathrm{thrombus}} = 0.07 \pm 0.02$ S/m.

6.1.2 Real-time identification of critical events

One of the novelties of this new methodology is also represented by the possibility to identify and follow in real-time the instantaneous and rapid events of detachment of the aggregates or morphologic variation in their spatial distribution. A whole or partial detachment of aggregates was intended as a quantitative variation, while their reorganization in space as a qualitative change.

In the attempt to monitor and control the thrombotic risk and to analyze in real-time the dynamics of thrombus formation events, Figure 6.1 shows the ability of identifying instantaneously the structural variation and the detachment of aggregates. In particular, only observing the time trend of the impedance signal $\Delta|Z|$ [%] in Figure 6.1, it was possible to identify and quantify the sudden and rapid signal falling that occurred between the time instants t_1 and t_2, in Figure 6.1 268 s and 278 s, respectively. The two confocal images in Figure 6.1 show, and visibly demonstrate, the variations in terms of aggregate detachment and morphologic variations of volume distribution. The circles in the images point out with particular evidence the situation as it was before and after the signal falling.

6.1.3 Classification of blood behavior and real-time prediction of individual thrombotic risk

The non-invasive and real-time analysis of the impedance magnitude measured at 150 kHz permits to monitor the adhesion and the aggregation processes from z-stacks, not only at the end of each experiment, as always done in the benchmark approaches, but also during the entire perfusion time. This new way of monitoring in real-time the blood behavior under dynamic conditions makes concretely possible to identify experimental parameters useful for a fast evaluation and prediction of the adhesion and aggregation levels that will be reached during the whole perfusion time. In this way, this methodologies reveals promising to monitor each individual patient and to early predict the

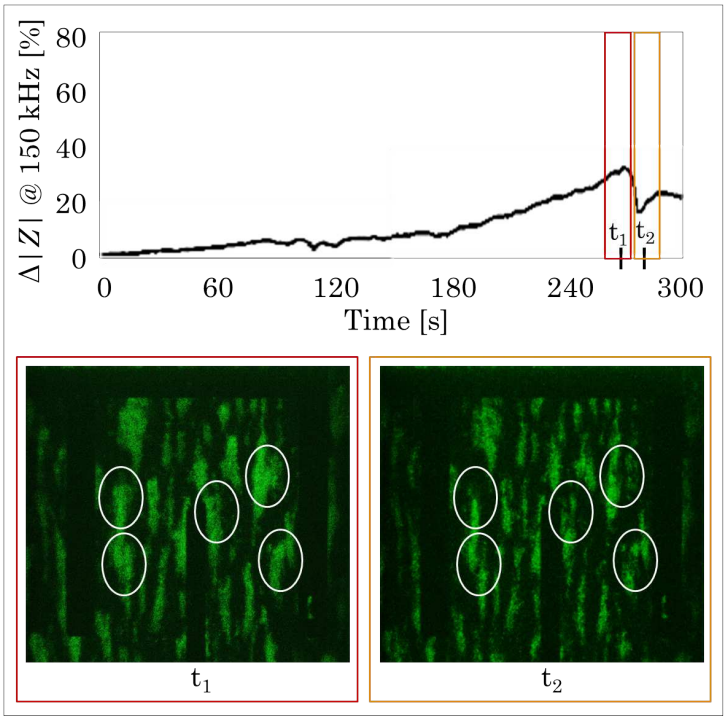

Figure 6.1: ***Real-time monitoring and identification of critical events.*** *Real-time identification of weakening and detaching aggregates and morphologic variations of their distribution based on the impedance magnitude increase in percentage $\Delta|Z|$ [%], evaluated in time. Images at time instant $t = t_1$ (268 s) and $t = t_2$ (278 s) show the distribution of the aggregates before and after the event. Circles underline the greater visible changes reflecting the signal variation.*

related thrombotic risk.

Considering and representing the relative variation of impedance magnitude with respect to its initial value ($\Delta|Z|$ [%])at 150 kHz, it was possible to distinguish four different physiological blood behaviors in terms of platelet adhesion and aggregation, among the 31 experiments performed. In Figure 6.2, each classification group is illustrated by three representative signals of impedance variation in time during the perfusion, from $t = 0$ s to $t = 300$ s, reflecting the situation represented in the 2D images on the right of Figure 6.2. The single images were acquired at $t = 300$ s and they are related to the plane of electrodes, where platelets adhered. Observing Figure 6.2, the different colors indicate an interval of percentage level of $\Delta|Z|$ reached by all the signals of the related group within the end of perfusion. The intuitive classification has been confirmed and strengthened thanks to the extraction of quantitative thresholds starting from each single value of $\Delta|Z|$ [%] measured at 150 kHz and reached at $t = 300$ s. The extraction of the classification threshold is illustrated in Figure 6.3a. In particular, according to the Figure 6.2 and the Figure 6.3a, it is possible to state, with our measuring system and the proposed sensor, that if a signal does not exceed the threshold $\Delta|Z| = 10$ % within

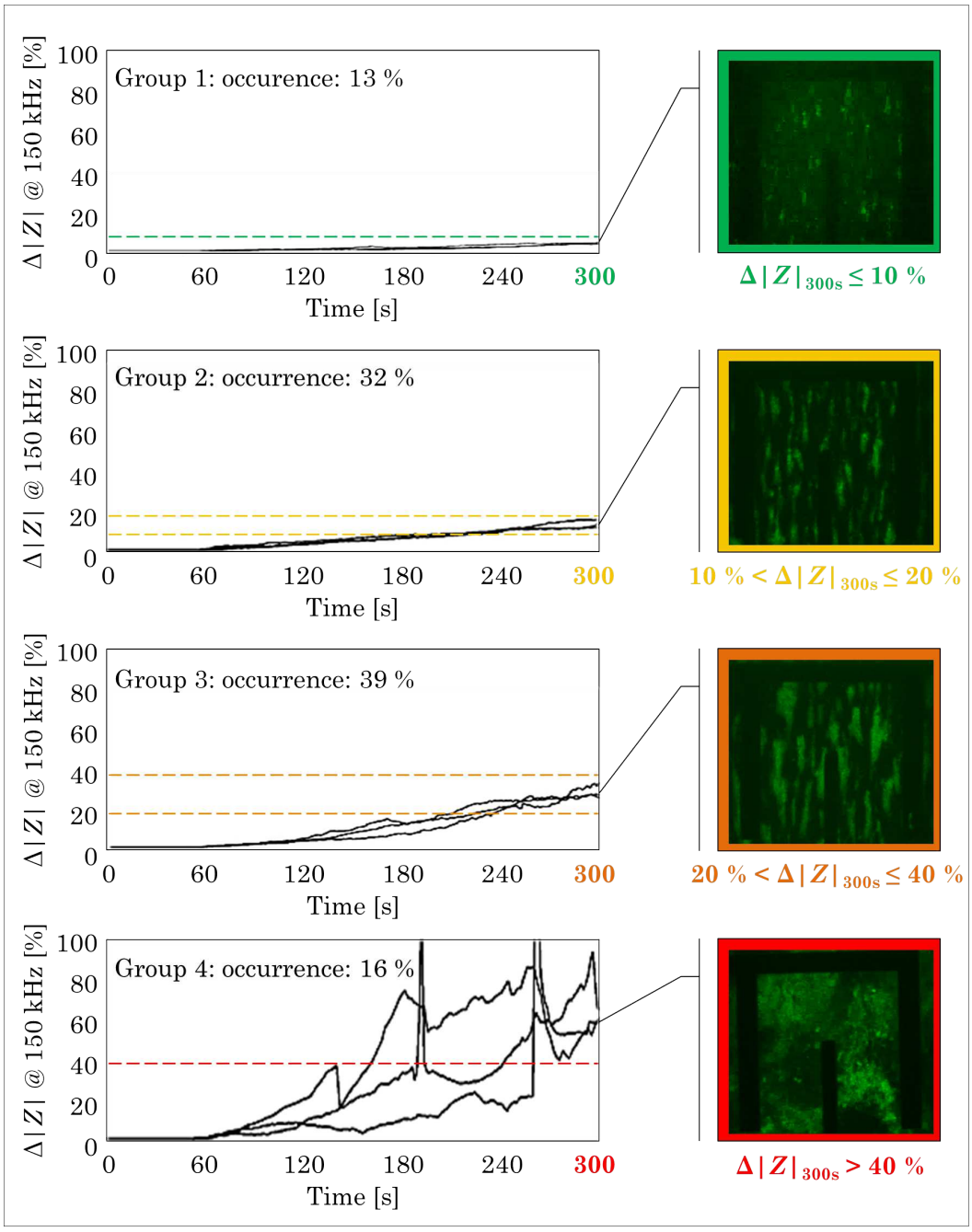

Figure 6.2: ***Classification of blood behavior.*** *Signals, expressed as impedance magnitude percentage increase $\Delta|Z|$ [%] at the frequency of 150 kHz, were classified in four groups, on the basis of the levels of platelet adhesion and aggregation exhibited during the experiment, confirmed by the representative images acquired at $t = 300$ s, on the right. For each group, three representative signals are shown. Group 1:* $\Delta|Z|_{300\ \mathrm{s}} = 7.55 \pm 1.42$ %, *green. Group 2:* $\Delta|Z|_{300\ \mathrm{s}} = 16.55 \pm 1.88$ %, *yellow. Group 3:* $\Delta|Z|_{300\ \mathrm{s}} = 31.15 \pm 5.43$ %, *orange. Group 4:* $\Delta|Z|_{300\ \mathrm{s}} = 65.46 \pm 20.12$ %, *red.*

300 seconds the related patient blood presents a behavior characterized by low adhesion and weak aggregation. More frequent and physiological conditions were found, instead, in the signals exhibiting a final value $\Delta|Z|_{300\ \mathrm{s}}$ between 10 % and 20 % or between 20 % and 40 %, while with signals that reached a percentage increase of over 40 % the patient should be consider at risk in terms of tendecy to develop thrombi. In particular, for the group 1, colored in green at the top in Figure 6.2, $\Delta|Z|_{300\ \mathrm{s}} = 7.55 \pm 1.42$ %, always less that the 10 % threshold, as stated. Afterwards, for the signals of group 2, colored in yellow in Figure 6.2, $\Delta|Z|_{300\ \mathrm{s}} = 16.55 \pm 1.88$ %, while for the orange group 3 $\Delta|Z|_{300\ \mathrm{s}} = 31.15 \pm 5.43$ %. Group 4, colored in red in the Figure 6.2 represents the group with the greatest signal variability because of the divergence and the lack of control of the platelet aggregation in this classification group, reflecting a thrombotic real risk. For this reason, the signals belonging to this group exhibit a final impedance magnitude increase higher than 40 %, in particular $\Delta|Z|_{300\ \mathrm{s}} = 65.46 \pm 20.12$ %. The percentage of classification for the groups, experimentally obtained from the experiments, resulted to be of 13 % of occurrence for the group 1 (4 experiments out of 31), 32 % of occurrence for the group 2 (10 experiments out of 31), 39 % of occurrence for the group 3 (12 experiments out of 31) and 16 % of occurrence for the group 4 (5 experiments out of 31).

It is interesting and important to clarify that all the blood samples measured have been taken from completely healthy people, in the sense that they had never manifested cardiovascular problems or diseases or related symptoms. Nevertheless, the results of the classification appeared, as evident from the Figure 6.2, very heterogeneous and scattered. This aspect led to further investigations and tests with the aim of finding an explanation about the causes of this variability among signals of equally healthy individuals. The results were very surprising. In fact, in the individuals belonging to the group 1 cell concentration percentage has been noticed to be lower than in the normal conditions, while in the individuals of group 4 mutations of coagulation factors have been found and reported with deepened clinical laboratory tests. It is therefore necessary to underline the fact that healthy individuals, who have never experienced any problems or cardiovascular symptoms, have discovered for the first time, thanks to the measurements made with this new sensor, to have a predisposition to the development of thrombosis. This predisposition, once identified, will be monitored and managed with a preventive and predictive approach, avoiding the occurrence of acute events, critical and dangerous for life.

Confirming the potential of this device and this methodology, in addition to the classification of the acquired impedance signals, for the first time a predictive thresholds have been proposed. In particular, the threshold of the $\Delta|Z| = 10$ %, the lowest among those considered in the classification phase, has been maintained to extract the time instant at which each signal exceeded this threshold. Plotting these time instants according to the classification group

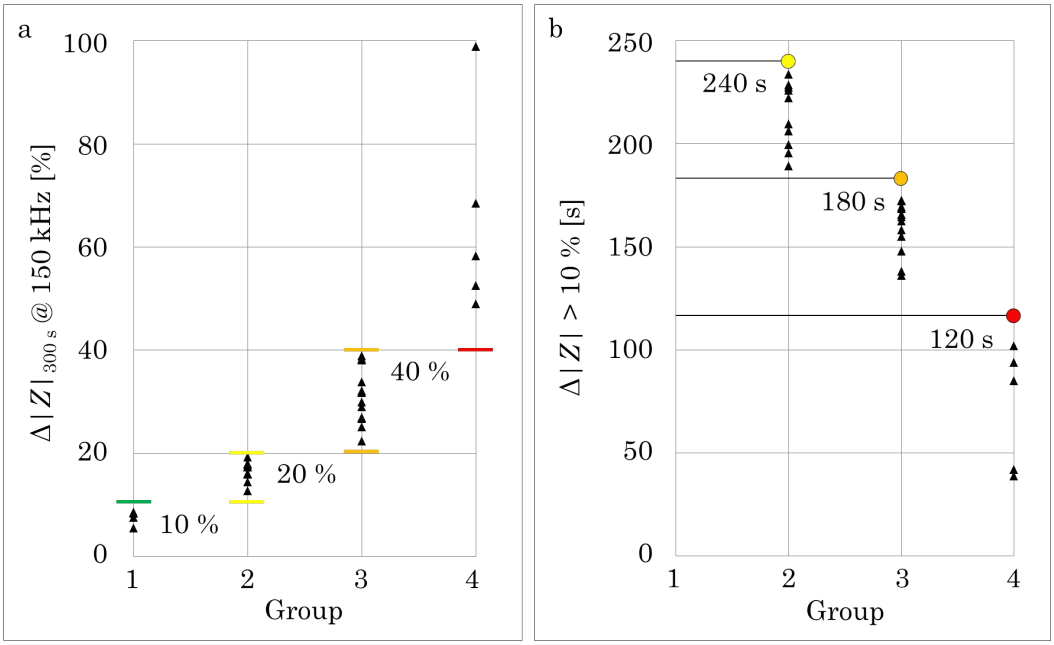

Figure 6.3: ***Extraction of thresholds.*** *The overall percentage increase of the impedance magnitude reached within 300 seconds. Group 1:* $\Delta|Z|_{300\ s} = 7.55 \pm 1.42$ %, $\Delta|Z|_{300\ s}$ *always* ≤ 10 %, *green. Group 2:* $\Delta|Z|_{300\ s} = 16.55 \pm 1.88$ %, $10\ \% < \Delta|Z|_{300\ s} \leq 20$ %, *yellow. Group 3:* $\Delta|Z|_{300\ s} = 31.15 \pm 5.43$ %, $20\ \% < \Delta|Z|_{300\ s} \leq 40$ %, *orange. Group 4:* $\Delta|Z|_{300\ s} = 65.46 \pm 20.12$ %, $\Delta|Z|_{300\ s} > 40$ %, *red. These values characterize the proposed classification thresholds (a). The predictive intermediate time instants of the* 10% *threshold overpassing have been experimentally defined, for each group, from the corresponding values of each experiment. Group 1: the curves did not overpass the threshold of* 10%. *Group 2:* $t_{\Delta|Z| > 10\ \%} = 213.83 \pm 15.76$ *s, yellow dot at* $t = 240$ *s. Group 3:* $t_{\Delta|Z| > 10\ \%} = 159.32 \pm 12.63$ *s, orange dot at* $t = 180$ *s. Group 4:* $t_{\Delta|Z| > 10\ \%} = 72.37 \pm 29.81$ *s, red dot at* $t = 120$ *s. These values characterize the proposed predictive thresholds (b).*

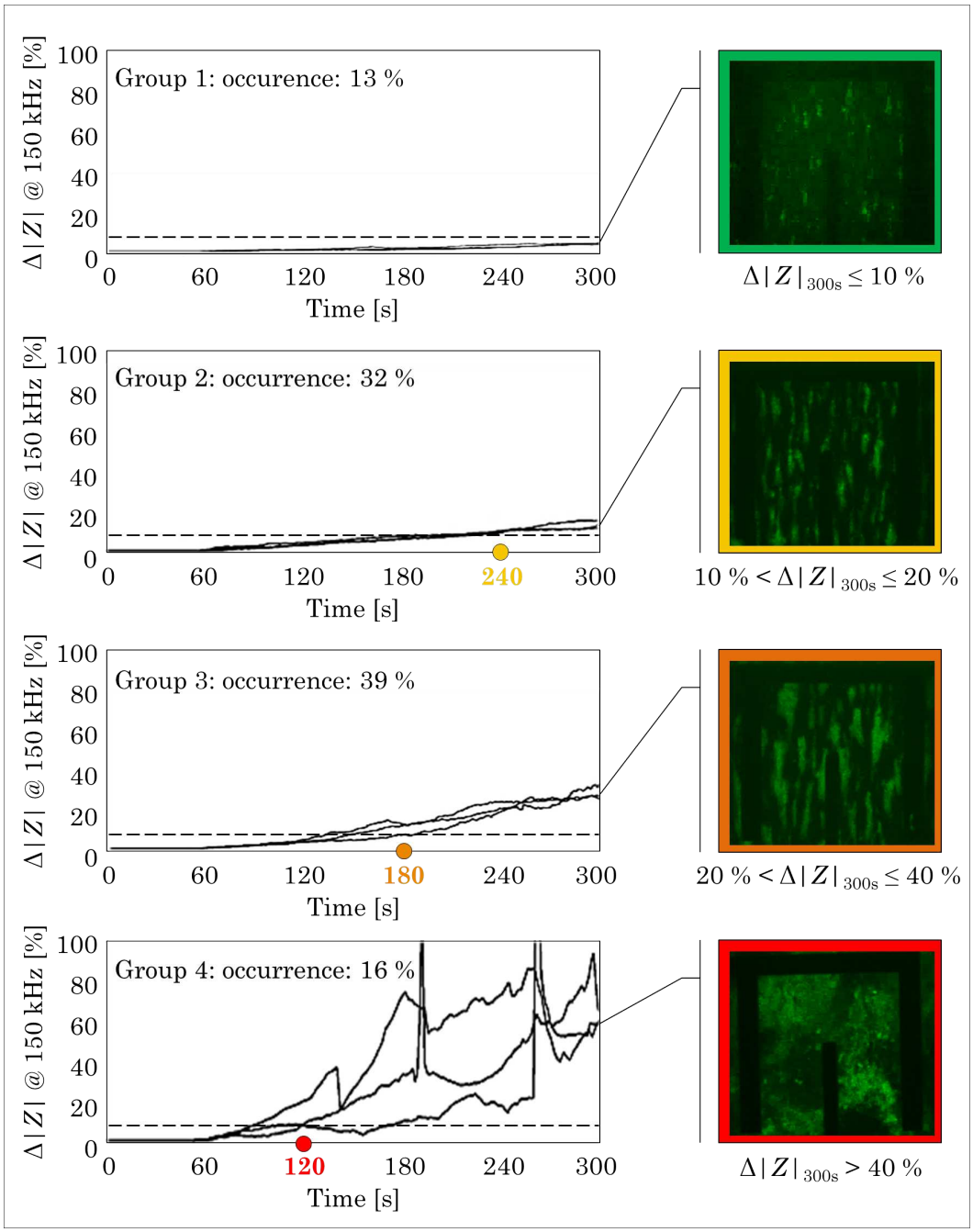

Figure 6.4: ***Real-time monitoring and prediction of individual thrombotic profile.*** *The dots on the horizontal axes indicate the time instants at which all the signals of the related group passed the 10 % of impedance increase (dashed line). Group 1: the curves did not overpass the threshold of* 10%*. Group 2:* $t_{\Delta|Z| > 10\ \%} = 213.83 \pm 15.76$ *s, yellow dot at* $t = 240$ *s. Group 3:* $t_{\Delta|Z| > 10\ \%} = 159.32 \pm 12.63$ *s, orange dot at* $t = 180$ *s. Group 4:* $t_{\Delta|Z| > 10\ \%} = 72.37 \pm 29.81$ *s, red dot at* $t = 120$ *s.*

to which they belonged, as illustrated in Figure 6.3b, maximum predictive time instants have been found for each group, within which each signal of that group overpassed the threshold of $\Delta|Z| = 10$ %. These characteristic time instants represent important predictive indices because, on the basis of the level of $\Delta|Z|$ [%] reached by a generic signal within these time instants, it is possible to predict the blood behavior as it will be at the end of the experiment. The further significant aspect, as confirmed by the Figure 6.4, is represented by the fact that, the more worrying is the condition of platelet adhesion and aggregation, the earlier is the ability to predict it. This implies, for the situations with high trombotic risk, the possibility to have a greater time interval to promptly take action and choose a pharmacological treatment avoiding critical events for the individual health and life. In detail, the colored dots on the horizontal axes in Figure 6.4 represent useful predictive thresholds and they indicate the time instants at which all the signals of the related group passed the 10 % of impedance increase, represented with a black dashed line. These predictive thresholds have been experimentally defined, for each group, from the corresponding values of each experiment, whose distribution is illustrated in Figure 6.3b. In particular, in group 1 the curves did not overpass the threshold of 10% until the end of the experiment. For signals belonging to the group 2, with a normal platelet adhesion and aggregation, $t_{\Delta|Z| > 10\ \%} = 213.83 \pm 15.76$ s and the predictive time instant for this group is the yellow dot at $t = 240$ s in Figure 6.4. Afterwards, in group 3, characterized by strong adhesion and aggregation, $\Delta|Z|$ exceeded the 10 % of increase within $t = 180$ s, with a $t_{\Delta|Z| > 10\ \%} = 159.32 \pm 12.63$ s. The dot associated is colored in orange in Figure 6.4. Finally, for signals of group 4, characterized by very high adhesion with massive towering aggregation leading to the microchannel occlusion, $t_{\Delta|Z| > 10\ \%} = 72.37 \pm 29.81$ s and the risk could be predicted until the predictive time instant $t = 120$ s, represented with a red dot in Figure 6.4.

6.1.4 Compatibility between volumes obtained from impedance measurements and from optical thresholding

Volumes comparison

The comparison between V_{OT} and V_{IM}, shown in Figure 6.5, reveals that they appeared highly correlated to each other exhibiting a Pearson's correlation coefficient [130] $r = 0.96$ (p value < 0.01). Data were obtained, as previously explained, from 22 experiments (71 % of the total), corresponding to the experiments classified as group 2 and 3, as shown in Figure6.2 and in Figure 6.4. In detail, only the experiments associated to a physiological (groups 2 and 3) and not pathological or at risk (groups 1 and 4) blood behavior have been used to compute V_{IM} and for the comparison with the related V_{OT} with the aim of validating the new method. This not because of detection limits of the new biosensor but because the benchmark optical thresholding method showed high limits in terms of accuracy in quantifying excessively small or

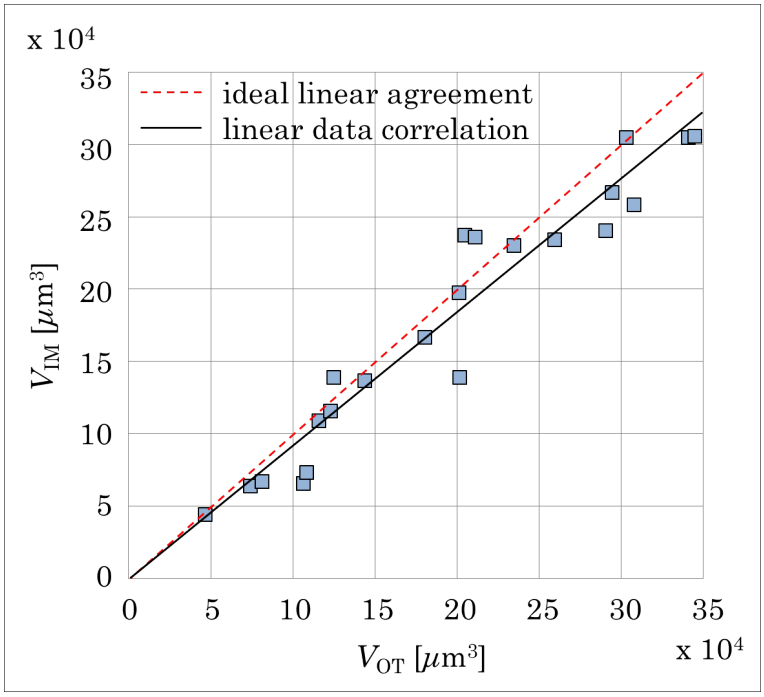

Figure 6.5: ***Volumes comparison.*** *Comparison between volumes V_{OT} and V_{IM} obtained at $t = 300$ s from optical and impedance data ($n = 22$). Data are highly correlated and exhibited a Pearson's correlation coefficient r equal to 0.96 (p value < 0.01). The linear representation of data (black line) is shown together with the ideal agreement condition (red dashed line).*

huge volumes. Despite this distinction, the experiments classified as group 1 and 4 represent extreme blood behavior conditions that our biosensor is able to recognize and classify in real-time, correctly and accurately, as pathological or at risk situations, as previously described. Figure 6.6 presents, for each z-stack of groups 2 and 3, V_{OT} and V_{IM} with their related uncertainty. According to what previously described, each V_{OT} has been expressed with its uncertainty of 15 %, while each V_{IM} with its 10 % of uncertainty, previously evaluated and published in [18]. The two methodologies for the volume measurement appeared metrologically compatible. This confirms the accuracy of our new device measurements, whose methodology is based on fusion of 2D fluorescent images with electrical impedance data.

3D reconstruction

It has to be remarked and highlighted the fact that the use of the confocal microscope has proved, at this stage, to be necessary to compare and validate the performances of the new biosensor. In Figure 6.7 two representative 3D reconstructions of the volumes spatial distribution are shown: on the left the reonstruction obtained from the optical benchmark method V_{OT} is shown, while the one obtained from impedance measurement V_{IM} is illustrated on the

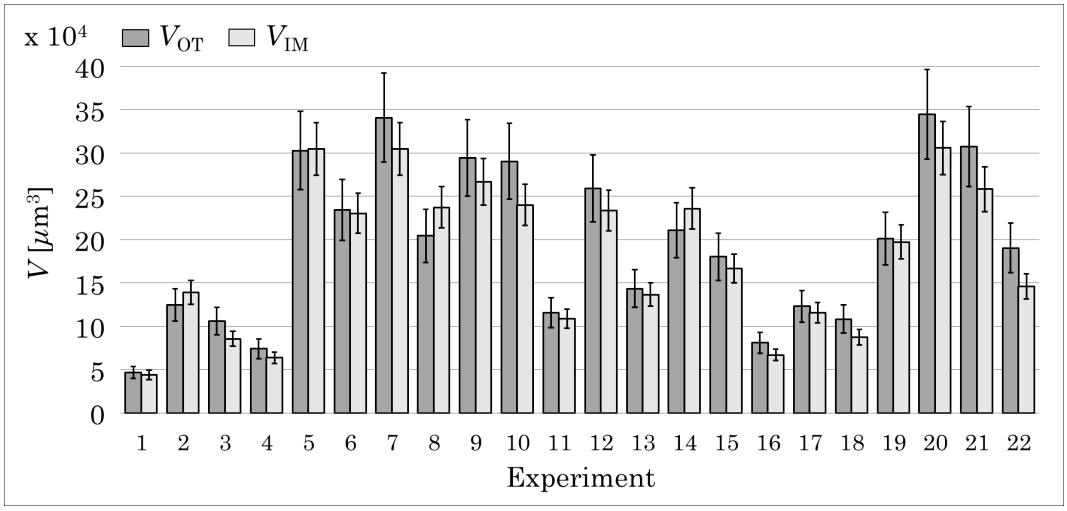

Figure 6.6: ***Compatibility evaluation between*** V_{OT} ***and*** V_{IM}***.*** *For each experiment (n = 22),* V_{OT} *has been expressed as the specific z-stack volume estimation* ± 15 *% (uncertainty of thresholding benchmark method), while* V_{IM} *has been expressed as the specific z-stack volume value estimated* ± 10 *% (uncertainty of reconstruction from impedance data).* V_{OT} *and* V_{IM} *measurements appeare compatible and, for the scopes highlighted, interchangeable.*

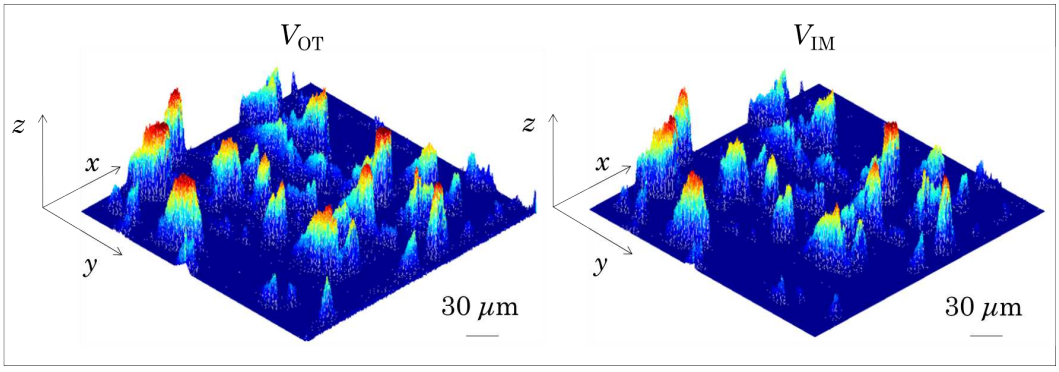

Figure 6.7: ***Three-dimensional volumes reconstruction and representation.*** *Example of a 3D reconstruction and representation of volume distributions* V_{OT} *and* V_{IM}*, obtained at* $t = 300$ *s with the benchmark method of thresholding and with impedance measurements, respectively.*

right. The two methods provided very close results.

6.2 Accuracy improvement in thrombus volume quantification and 3D reconstruction

6.2.1 Calibration of overestimation

All the measurements regarding the biomedical field require a critical interpretation and confirmation of the physician, because of the high intra- and inter-variability of the patients. With regard to the applicability of the volume measurement in clinics, it is important to remember that the biosensor was designed to be proposed as a point of care device. Nevertheless, to be the biosensor calibrated in reconstructing and measuring volumes, the 3D z-stacks acquired with the confocal microscope at the end of each experiment were needed to reconstruct the volumes with the benchmark technique, as reference values.

Optimal factor calibration estimation

The optimal calibration factor $\hat{C}$ was estimated from $n = 10$ confocal images sequences representing a single bead of known volume 4.19 μm^3. In particular, $\hat{C}$ was obtained with an iterative computation, which minimized the error function defined as the absolute difference between the real bead volume and the estimated one. The iterations stopped when the maximum height of each bead was at least equivalent to its real diameter, thus satisfying a z-dimensional condition, and when the correspondent volume was at least equal to its real known volume, thus matching a volumetric condition. The optimum factor resulted $\hat{C} = 0.10 \pm 0.01$.

The solid model of the spheres used and its sampled representation are represented in Figure 6.8a and in Figure 6.8b, respectively, according to the physical dimension of the pixels $r = 0.33$ μm, the conversion factor $f = 0.33$ μm/pixel and the real dimension of the spheres. The solid model had to be sampled in order to associate to each x- and y-position a specific heigth h to be added to the others to achieve an estimation of the total volume. In particular, the matrix in the Figure 6.8c contains the half height values associated to each pixel of the sampled model.

Calibration with fluorescent beads

In order to validate the model on a different dataset from the one used in previous subsection, the calibration with the optimal factor $\hat{C}$ has been applied on other $n = 10$ beads z-stacks, not previously used, to verify the robustness of the method. Figure 6.9a and Figure 6.9b report the numerical estimation and a graphical representation of single beads volume performed following

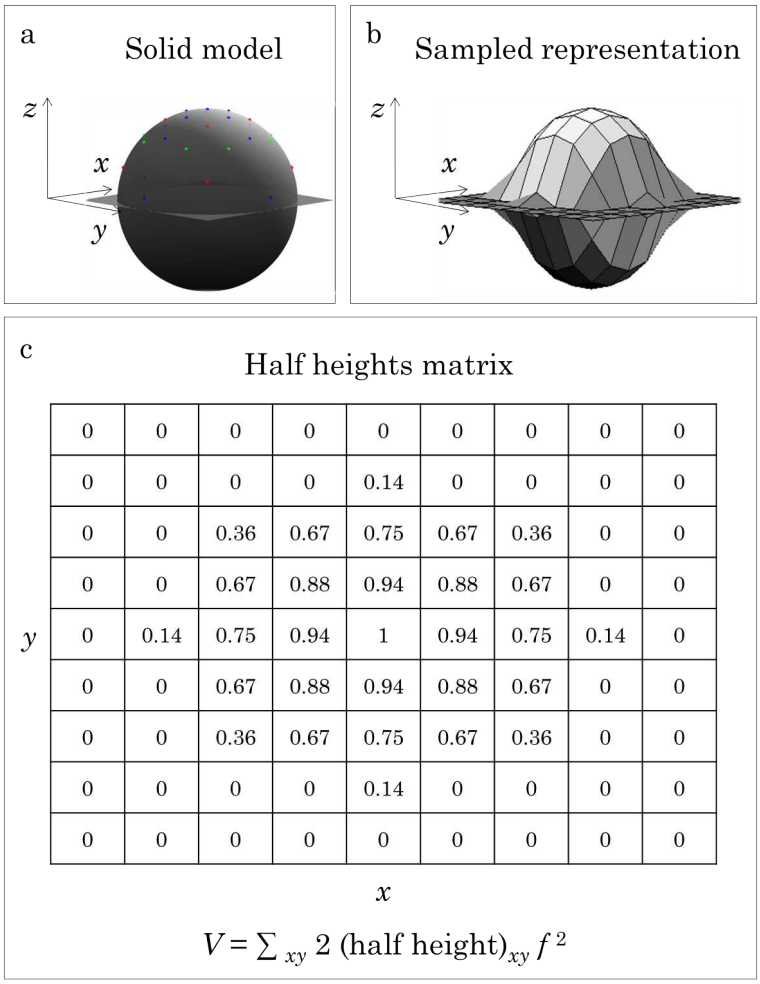

0	0	0	0	0	0	0	0	0
0	0	0	0	0.14	0	0	0	0
0	0	0.36	0.67	0.75	0.67	0.36	0	0
0	0	0.67	0.88	0.94	0.88	0.67	0	0
0	0.14	0.75	0.94	1	0.94	0.75	0.14	0
0	0	0.67	0.88	0.94	0.88	0.67	0	0
0	0	0.36	0.67	0.75	0.67	0.36	0	0
0	0	0	0	0.14	0	0	0	0
0	0	0	0	0	0	0	0	0

Figure 6.8: ***Spheres representation.*** *Solid model (a). Sampled representation of the geometrical solid model (b). Half heights matrix, from which the volume can be estimated (c).*

the procedures previously described. The results were compared with those obtained with ImageJ and Volocity computations. As shown in Figure 6.9b, the beads volume quantified applying the model calibration measured 5.9 ± 0.6 μm^3, while the volumes calculated with ImageJ and Volocity were 25 ± 1 μm^3 and 18.3 ± 0.8 μm^3, respectively. All the three methods appeared significantly different, as confirmed by the t-test: the p value, for all the comparisons, was less than 0.001. Each single volume was evaluated assuming as reference the real known volume, 4.19 μm^3, of a single bead.

Defining the volume overestimation as the ratio between the measured value and the real one, it has been quantified as 6.1 ± 0.3 with ImageJ, 4.3 ± 0.2 with Volocity and only 1.4 ± 0.1 with the new proposed algorithm (Figure 6.9c). A perfect reconstruction would yield to the optimal unitary ratio of overestimation, indicated with a dashed line in the Figure 6.9c. The proposed method permitted to reduce significantly the overestimation error and to obtain realistic volume measurements and representations. The data continued to be significantly different among each other, because each ratio was referred to the same real absolute volume. The p value for all the population comparisons remained less than 0.001.

Platelets small aggregates and multi-layer aggregates

The algorithm was then applied to $n = 10$ confocal z-stacks related to small aggregates of platelets, that are small groups of platelets, from 3 to 10, that adhere to the substrate as a single layer and whose number can be clearly observed and determined. For each small aggregate, it was thus possible to estimate a realistic absolute volume, multiplying the number of platelets observed by the representative volume of a platelet, considering its semi-spherical discoidal shape and its average diameter of 2 μm [80]. In the case of small aggregates the volume overestimation was 5.5 ± 0.8 with ImageJ, 4.3 ± 0.8 with Volocity and 1.3 ± 0.2 with the proposed method, as shown in Figure 6.10a. This confirmed the robustness of the algorithm. The new value thus obtained was significantly different to those estimated through the traditional measurement methodology, with a related p value less than 0.001.

The last step for the proposed method was represented by its application to $n = 10$ z-stacks of images of aggregates composed of a considerable number of platelets. Because of the clear impossibility of accurately pre-estimating a real reference volume, the measurements were expressed as the overestimation achieved with benchmark methods with reference to the measurement performed with the new algorithm. This expression of the results as overestimation among the methods has been done also for the measurements presented in the previous subsections related to beads and small aggregates (Figure 6.10b and Figure 6.10c).

According to this approach, the accuracy and the repeatability of the calibration algorithm proposed were confirmed by the maintenance of comparable overestimation ratios. The overestimation measured with ImageJ appeared,

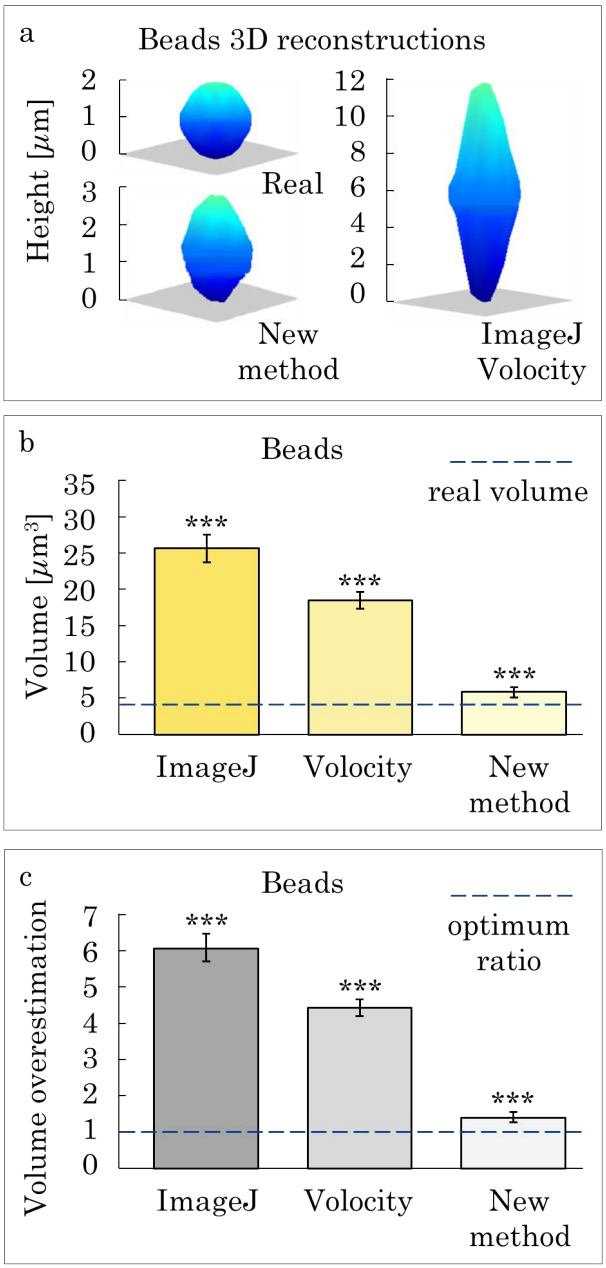

Figure 6.9: ***Results of calibration and measurements.*** *3D rendering of a representative bead (on the top, on the left), 3D reconstruction of the same bead performed with benchmark thresholding methods (on the right) and obtained with the new method (at the bottom, on the left) (a). Beads absolute volume quantification performed with ImageJ ($25 \pm 1\ \mu m^3$), Volocity ($18.3 \pm 0.8\ \mu m^3$) and the new method proposed ($5.9 \pm 0.6\ \mu m^3$). Measurement techniques appear significantly different among each other as confirmed by the t-test: p value < 0.001 ($***$). The dashed line indicates the real volume of each single bead ($4.19\ \mu m^3$) (b). Beads volume overestimation, with reference to the real volume, obtained with ImageJ (6.1 ± 0.3), Volocity (4.3 ± 0.2) and the new method proposed (1.4 ± 0.1). All the results are expressed as mean $\pm$ standard deviation. The p value remains < 0.001 ($***$). The dashed line indicates the unitary optimum ratio, that represents the perfect matching (c).*

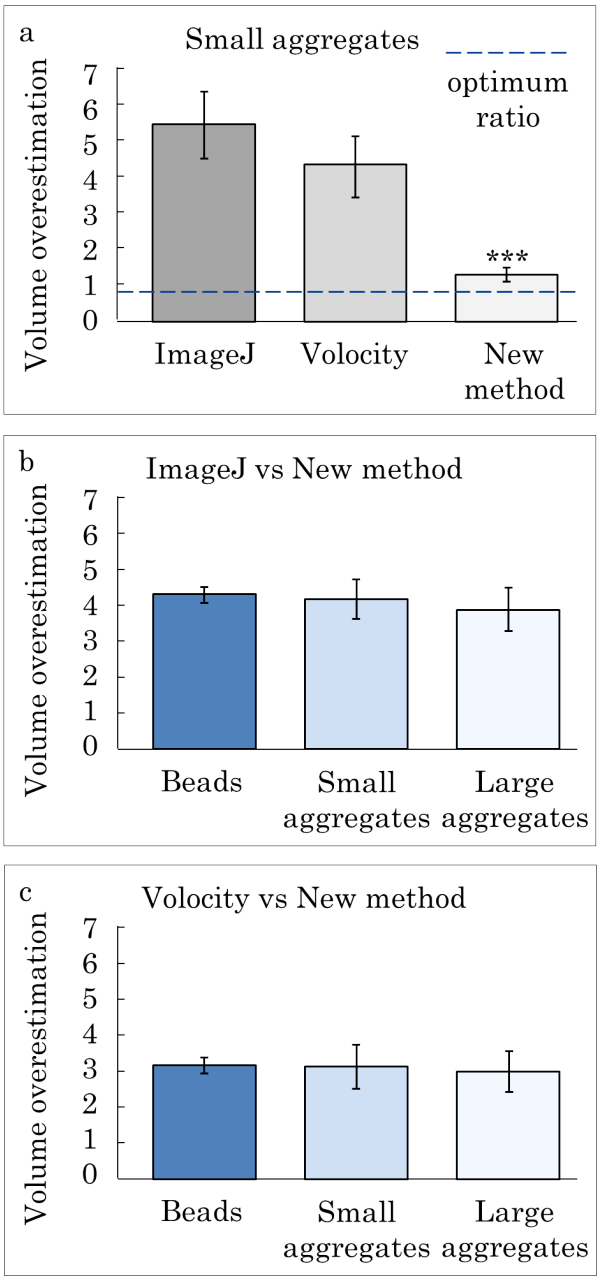

Figure 6.10: ***Volume overestimation.*** *Platelet small aggregates volume overestimation (n = 10 aggregates z-stacks), with reference to their real volume, computed with ImageJ (5.5 ± 0.8), Volocity (4.3 ± 0.8) and the new method proposed (1.3 ± 0.2). The last result was significantly different to those estimated through the benchmark methods, with a p value < 0.001 (∗ ∗ ∗).The dashed line indicates the unitary optimum ratio, that represents the perfect matching (a). Volume overestimation with ImageJ, with respect to the volume quantified with the new method (n = 10 z-stacks), was 4.2 ± 0.2 for beads, 4.1 ± 0.5 for platelet small aggregates and 3.9 ± 0.6 for large aggregates (b). Volume overestimation with Volocity, with respect to the volume quantified with the new method (n = 10 z-stacks), measured 3.1 ± 0.2 for beads, 3.1 ± 0.6 for small aggregates and 2.9 ± 0.5 for platelet thrombi. The results have been expressed as mean ± standard deviation. All the intervals were metrologically compatible (c).*

in fact, 4.2 ± 0.2 for beads, 4.1 ± 0.5 for small platelet aggregates and 3.9 ± 0.6 for large platelet aggregates. This meant that the metrological compatibility between the measurements of overestimation was respected (Figure 5b). Similarly, considering the ratios referred to the Volocity overestimation of each volume, the results obtained are 3.1 ± 0.2 for beads, 3.1 ± 0.6 for small aggregates and 2.9 ± 0.5 for large aggregates (Figure 6.10c). The overestimation of the benchmark methods was thus proved by compatible intervals.

6.3 Uncertainty evaluation

Optical thresholding uncertainty

Remembering that an accurate quantification of thrombus volume with the optical benchmark thresholding method represents an essential reference measurement to validate our impedance biosensor performances, the uncertainty $u(V_{\mathrm{OT}})$ in the computation of V_{OT} was evaluated, from the uncertainties propagation theory [82], as

$$u(V_{\mathrm{OT}}) = \left(\frac{\partial V_{\mathrm{OT}}}{\partial Thr}\right)\ u(Thr) \tag{6.1}$$

where Thr is the threshold defined as described and $u(Thr)$ is its related uncertainty. It is possible to see that the H_{Max} and the V_{OT} curves shows a stepwise behavior and the maximum step size for both of them is 3 threshold units. This step length corresponds, in the worst case, to an error in threshold identification of $\delta Thr = 3$. Assuming an uniform distribution, the uncertainty in the optimal threshold value definition can be reasonably expressed as $u(Thr) = \delta Thr/\sqrt{3} = 3/\sqrt{3}$. The quantity $\partial V_{\mathrm{OT}}/\partial Thr$ in the Equation 6.1 is shown in the Figure 6.11. Accordingly, the uncertainty $u(V_{\mathrm{OT}})$ results in the order of 15 %.

Figure 6.11 represents the results of the sensitivity analysis of the optical benchmark thresholding method. For $n = 22$ z-stacks, V_{OT} was evaluated for different threshold values in the range [Thr-10,Thr+10], where Thr is the optimal value identified as threshold for a specific z-stack. Therefore, the variation of V_{OT} as a function of the threshold was expressed as percentage variation of the volume quantity ΔV_{OT} [%] with respect to the related volume obtained with the optimal threshold value Thr

$$\Delta V_{\mathrm{OT}(Thr+i)} = 100\frac{V_{\mathrm{OT}(Thr+i)} - V_{\mathrm{OT}(Thr)}}{V_{\mathrm{OT}(Thr)}} \qquad i = -10, -9, ..., 9, 10 \tag{6.2}$$

The analysis results shown in Figure 6.11, where $\Delta V_{\mathrm{OT}(Thr-1)} = 15.38 \pm 3.67$ % and $\Delta V_{\mathrm{OT}(Thr+1)} = -12.41 \pm 2.61$ %, were perfectly in agreement with the uncertainty of 15 % obtained from the Equation 6.1. In general, it is remarkable to notice that the volume estimation using the confocal microscope

is highly sensitive to the intensity threshold variation. In fact, an error δThr of few threshold units can lead to an error in volume reconstruction greater than 100 %. The method just described allowed to establish a threshold value, not delegating all the action to the human subjectivity of the operator, thus increasing the accuracy in thrombus volume quantification and reconstruction. The results in the text are expressed as mean ± standard deviation.

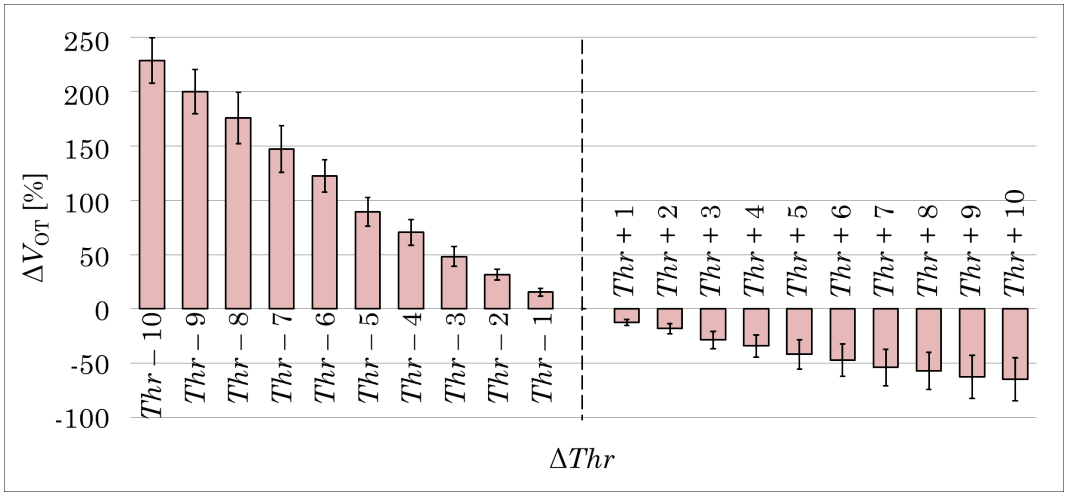

Figure 6.11: ***Sensitivity analysis of the benchmark thresholding method.*** *Volumes (n = 22) are expressed as percentage variation with respect to the volume obtained with the optimal threshold value Thr (dashed line).*

New algorithm uncertainty in volumes estimation

The uncertainty on the volume estimation has been evaluated by means of propagation of uncertainty. In particular, the main contributions of uncertainty are related to three uncertain quantities: the identification of the intensity threshold for the binary mask, the identification of intensity thresholds d_1 and d_2, to obtain the distance D and the uncertainty on $\hat{C}$. Regarding the threshold for the binary mask, the uncertainty in extracting the pixels belonging to the base area depends on the quantization of the intensities $M_{j,k}$ and $b_{1\ j,k}$, with $j,k = 1,2,...,d$ and $d = 255$. Since the intensities are quantized in 255 levels, the quantization uncertainty, assuming a uniform distribution in [-1, 1], is given by

$$u(M_{j,k}) = u(b_{1\ j,k}) = \frac{1}{\sqrt{3}} \qquad j,k = 1,2,...,d \tag{6.3}$$

Thus, the uncertainty on the volume estimation due to the uncertainty on the binary mask $u(V)|_{\text{mask}}$ can be expressed as

$$u(V)|_{\text{mask}} = \sqrt{\left(\sum_{j,k} \frac{\partial V}{\partial M_{j,k}} u(M_{j,k})\right)^2 + \left(\sum_{j,k} \frac{\partial V}{\partial b_{1\ j,k}} u(b_{1\ j,k})\right)^2} \tag{6.4}$$

with $j, k = 1, 2, ..., d$. In order to evaluate the two sensitivities in the Equation 6.4, the values of $M_{j,k}$ and $b_{1\ j,k}$ have been varied around the operating points and the change in the readout of the volume estimated has been evaluated. The two sensitivities resulted 0.02 μm^3/step for beads, 0.05 μm^3/step for small aggregates and 0.95 μm^3/step for large aggregates.

In the same way, for the uncertainty on height estimation, the uncertainty of the volume related to the intensities corresponding to d_1 and d_2 has been calculated. Since d_1 and d_2 are, again, intensities quantized in 255 levels, their uncertainty is the same as in the Equation 6.3 and the contribution to uncertainty on volume due to height estimation $u(V)|_{\text{height}}$ is thus

$$u(V)|_{\text{height}} = \sqrt{\left(\sum_{j,k} \frac{\partial V}{\partial d_{1\ j,k}} u(d_{1\ j,k})\right)^2 + \left(\sum_{j,k} \frac{\partial V}{\partial d_{2\ j,k}} u(d_{2\ j,k})\right)^2} \tag{6.5}$$

with $j, k = 1, 2, ..., d$. The sensitivities resulted to be 0.03 μm^3/step for beads, 0.14 μm^3/step for small aggregates and 1.73 μm^3/step for large aggregates. Referring to the uncertainty on volume estimation due to $\hat{C}$ extraction, this calibration coefficient revealed a multiplying factor in the relation to obtain the heights associated to each x- and y-position, so the uncertainty on volume due to $\hat{C}$ can be expressed ad

$$u(V)|_{\hat{C}} = \frac{u(\hat{C})}{\hat{C}} V \tag{6.6}$$

where $u(\hat{C}) = 0.01$ has been evaluated as the standard deviation of $\hat{C}$, as reported.

The overall uncertainty on volume finally results

$$u(V) = \sqrt{(u(V)|_{\text{mask}})^2 + (u(V)|_{\text{height}})^2 + (u(V)|_{\hat{C}})^2} \tag{6.7}$$

The last term in previous equation is prevailing, since the relative uncertainty on $\hat{C}$ is 10 %, thus, the overall uncertainty is in the order of 10 %.

Despite the uncertainty of the proposed method seems apparently high, it allows obtaining considerable improvements in terms of measurement reliability and accuracy if compared to the methods traditionally used to quantify the thrombus volume. It is important to specify that, in any case, all the measurements regarding the biomedical field require the critical interpretation and confirmation of the physician, because of the high intra- and inter-variability of the patients. Consequently, while the inaccuracy of 400-600 % with the benchmark methods makes them not applicable in real medical cases, we can affirm that the uncertainty of 10 % on volume measurements does not represent a problem with regard to the applicability of our method in clinics.

6.4 New perspectives for pre-analytical quality controls in clinical laboratories

6.4.1 Blood components characterization

Signals obtained with the sensing module through a simple pair of conductive wires represent preliminary important data for the development of the sensor, as it was described, and for the achievement of the promising results in terms of characterization of blood components and evaluation of their quality for clinical measurements.

Fast discrimination and quality indicators identification

Impedance signals related to the different blood components extracted with the capacitive biosensor described are displayed in Figure 6.12 as magnitude and phase. For each material, the average signal, with its related standard deviation, is illustrated (n = 20). It is evident the possibility, with this new prototype, to discriminate blood components on the basis of their impedance magnitude and phase, that are representative of their resistance to the current flow and depend on the amount of the capacitive contribution due to the lipidic membrane, mostly of the red blood cells. In particular, observing the magnitude of impedance at the central frequencies in Figure 6.12a, from the bottom to the top, following a decrease of conductivity, we can observe in order: white clot, plasma, serum, white clot with hemolysis, serum with increasing levels of hemolysis, whole blood at different densities and red clot. The properties of blood components, revealing that the electrical conductance decreases as the red blood cells concentration increases, can be qualitatively appreciated also from the phase diagrams of Figure 6.12b, where it is evident that all the blood components without red cells or containing damaged red cells have an impedance phase distinguishable from the impedance phase of samples with healthy red blood cells.

In addition to the visibly capability of characterizing different blood components with electrical impedance measurements, the most promising results, noticeable observing Figure 6.12, are represented by the curves of serum, pure or with hemolysis, and those relative to the blood, in particular the combination that comprehends whole blood, whole concentrated blood and red clot. These results allow associating and proposing a specific quantitative pre-analytical threshold value for a rapid control of serum and whole blood samples quality. According to the impedance magnitude signals analyzed and here shown, we can thus affirm that serum and whole blood samples can be accepted for laboratory analyses and transfusions if their impedance magnitude at the central frequencies, measured with our sensor, does not overpass 700 Ω and 3 kΩ, respectively.

An interesting aspect that deserves attention and further experiments is

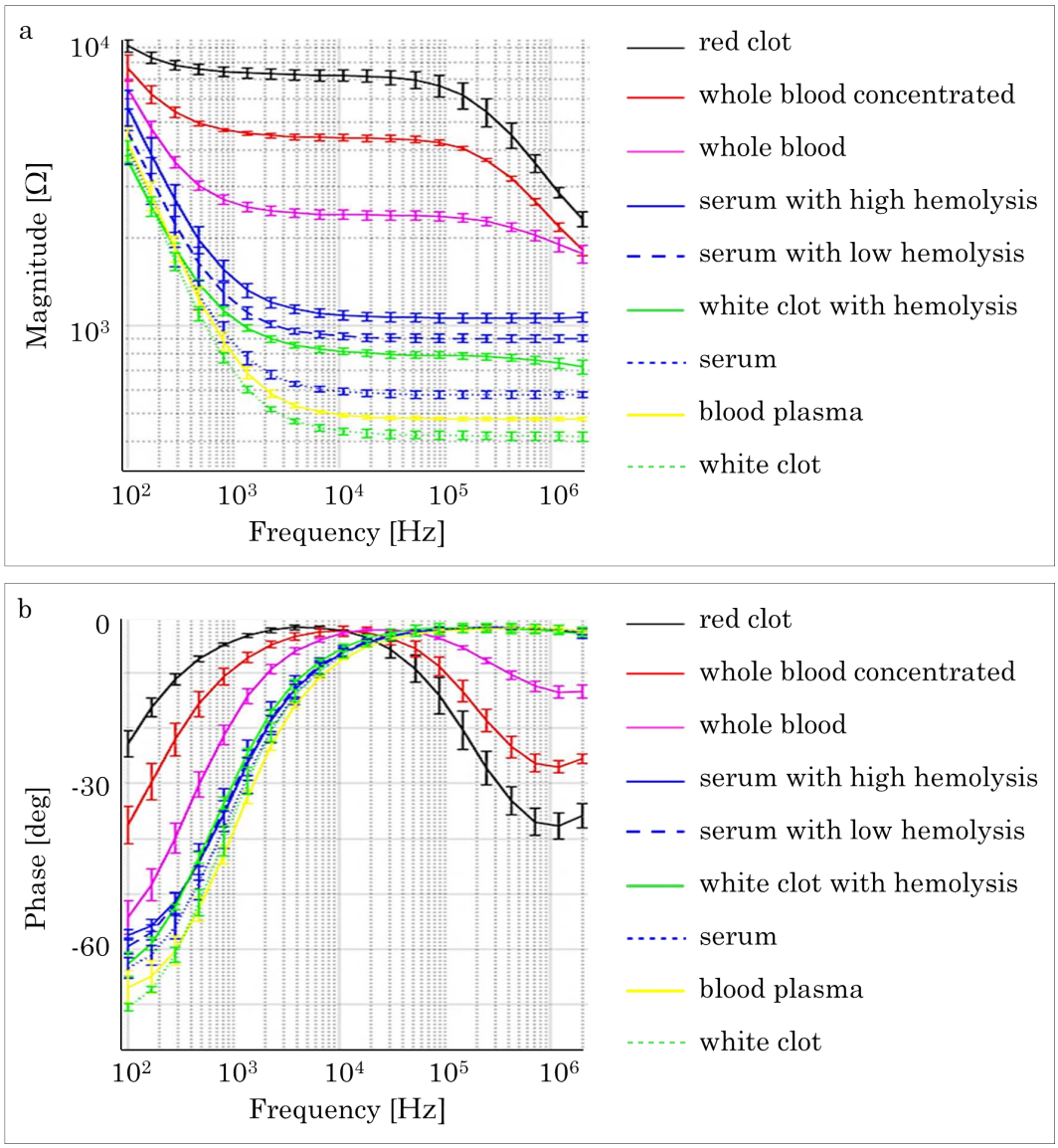

Figure 6.12: ***Impedance signals representation with Bode diagrams.*** *Electrical impedance signals displayed as magnitude (a) and phase (b). Each blood component is represented in terms of mean and standard deviation (n = 20).*

represented by the white clot curves. In Figure 6.12a white clots without hemolysis seem to be the most conductive material among those analyzed and this is due to the fiber net highly conductive structure of fibrin, combined with the absence of resistive cellular components inside. With this approach, fibrin could be electrically described and its formation could be identified and monitored in real-time during the whole physiological process of coagulation.

Lumped elements parameters quantification

The discrimination of blood components through the impedance signals is confirmed and enriched by the inverse analysis performed with a Complex Non-linear Least Square (CNLS) fitting software. Thanks to this, it was possible to quantify each single lumped elements parameter of the equivalent circuit (C_1, ψ_1, R, C_2, ψ_2) with an uncertainty in the order of 2%. The numerical parameters estimated, related to the equivalent circuit, are displayed in the Table 6.13 and are expressed in terms of mean and standard deviation (n = 20). An important aspect of the electrical characterization of a system

		C_1 (F)	ψ_1 (·)	C_2 (F)	ψ_2 (·)	R (Ω)
—	red clot	9.43E-7 ± 7.10E-8	8.53E-1 ± 1.15E-2	9.66E-11 ± 1.40E-11	8.80E-1 ± 6.25E-2	5.44E+3 ± 3.44E+2
—	whole blood concentrated	9.21E-7 ± 5.60E-8	8.67E-1 ± 2.31E-2	4.81E-11 ± 4.30E-12	7.83E-1 ± 5.77E-3	4.46E+3 ± 1.23E+2
—	whole blood	8.99E-7 ± 7.70E-8	8.63E-1 ± 5.77E-3	1.87E-11 ± 6.30E-12	7.40E-1 ± 1.00E-2	2.39E+3 ± 9.14E+1
—	serum high hemolysis	8.85E-7 ± 8.70E-8	8.33E-1 ± 5.78E-3	1.02E-12 ± 1.90E-13	1	1.06E+3 ± 3.76E+1
- - -	serum low hemolysis	9.50E-7 ± 6.10E-8	8.37E-1 ± 5.80E-3	2.00E-12 ± 7.20E-13	1	8.96E+2 ± 3.08E+1
—	white clot hemolysis	9.50E-7 ± 1.30E-7	8.13E-1 ± 5.77E-3	1.70E-11 ± 7.10E-12	7.89E-1 ± 1.15E-3	7.89E+2 ± 1.95E+1
·····	serum	9.70E-7 ± 5.50E-8	8.60E-1 ± 1.00E-2	4.60E-12 ± 1.60E-12	1	5.76E+2 ± 1.78E+1
—	plasma	9.10E-7 ± 1.00E-7	8.70E-1 ± 1.00E-2	6.40E-12 ± 9.50E-13	1	4.75E+2 ± 1.01E+1
·····	white clot	9.10E-7 ± 6.90E-8	8.90E-1 ± 1.00E-2	6.40E-12 ± 1.40E-12	9.17E-1 ± 7.64E-2	4.19E+3 ± 1.05E+1
		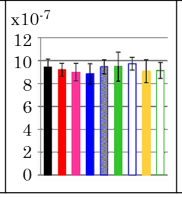	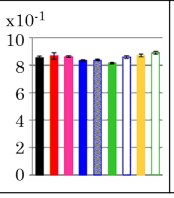	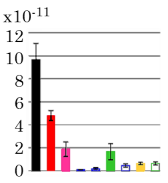	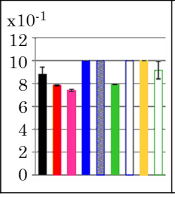	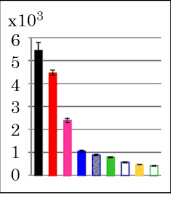

Figure 6.13: ***Extracted lumped elements according to the equivalent circuit.*** *The values of C_1, ψ_1 represent the common double layer effect, while the specific intrinsic blood components behavior can be described through the values of C_2, ψ_2 and R.*

is the possibility to identify and associate equivalent circuit elements with specific physical processes occurring. In particular, the parameters of CPE_1, related to the double layer, (C_1, ψ_1) appear almost equal for all the blood components analyzed. In fact, the double layer is common to all the blood components because it is associated to the interface interaction between the material and the metallic electrodes. For this reason, CPE_1, representing a common electrical behavior, can be compensated with the aim of evidencing

the specific electrical properties of each biological material, dealing with the specific electrical response of the material alone. The numerical results confirm that the CPE_2 is directly related to the presence or the absence of cells (mostly red blood cells) and their possible membrane breaking. In particular, the values of the CPE2 parameters (C_2, ψ_2) and R exhibit a significant difference if there are cells (the higher the number or the concentration, the higher the value), if cells are absent or if there are cells with damaged membrane (hemolysis condition). In addition, the phase shift of CPE_2, ψ_2, measures exactly 1 when cells are absent or their membrane are damaged (blood plasma and serum), indicating that, in these cases, CPE_2 behaves like an ideal capacitor, with a very low capacitance C_2.

Interpolations of frequency-points are shown in Figure 6.14, for all the blood components analyzed, in a real-imaginary plot, without double layer compensation (Figure 6.14a) and with compensation (Figure 6.14b) which highlights the samples differences on the basis of their intrinsic characteristics. Imagining the natural extension of the compensated curves in Figure 6.14b towards infinite frequencies, it is evident that they tend to blood plasma, in agreement with the decreasing of capacitive behavior at high frequencies. All the results confirm and verify the physical reasonability of the equivalent circuit chosen and proposed.

6.4.2 Single-frequency measurements

With the aim of obtaining more accurate and informative results, measurements are generally expected to be performed using a multi-frequency approach. As previously described, electrical impedance of blood components was measured over a large frequency range, from 100 Hz to 2 MHz. Observing the signals of impedance magnitude in Figure 6.12a, we tried to identify a frequency, among those used, that could be optimal in terms of accuracy and capability in discriminating the different blood components with resolution, with the purpose of improving the efficiency and the performances of our measurements.

Figure 6.15, according to the color legend of Figure 6.12 and Figure 6.14, shows the quantitative analysis to extract the optimal frequency in the range [100 Hz, 2 MHz]. Observing impedance magnitude signals in Figure 6.12a, it is intuitive that the best frequency usable for a single-frequency measurement takes place in the central interval of the frequencies used, where the distance between signals seems to be greater than the distance at lower or higher frequencies. According to this observation, we quantified, for all the possible couples of signals belonging to adjacent blood components visible in Figure 6.12a, their percentage difference in impedance magnitude, choosing the worst difference to represent in Figure 6.15a the minimal distance between a blood component and its adjacent one. For example, to present the black line in Figure 6.15a, the percentage differences were computed between each red clot

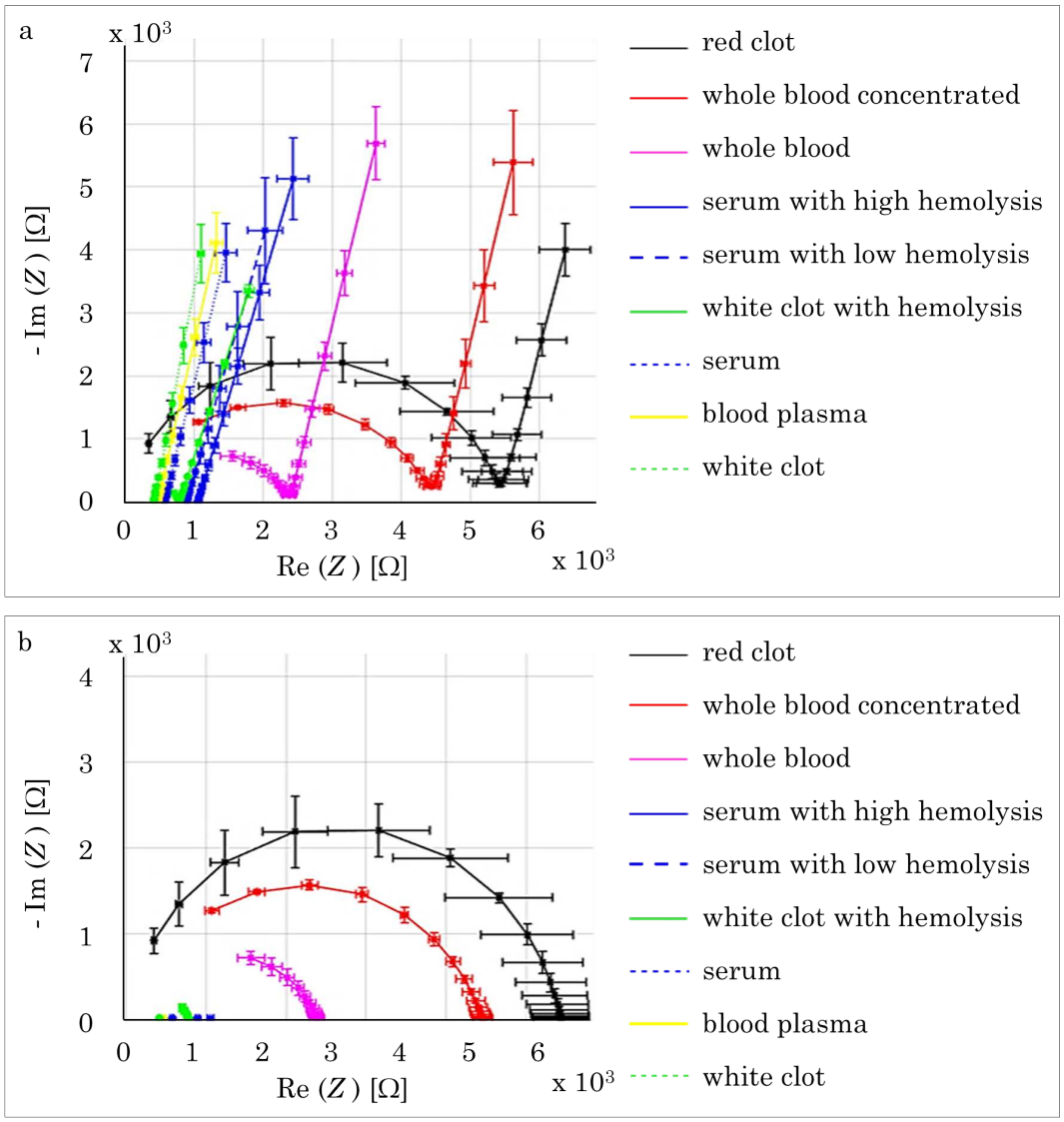

Figure 6.14: ***Impedance signals representation in the complex plane.*** *Electrical impedance signals displayed without (a) and with (b) the compensation of the double layer effect. Each blood component is represented in terms of mean and standard deviation, both for the real and the imaginary part (n = 20).*

signal and each signal of whole blood concentrated, choosing, at the end, the lowest among the signals thus quantified. At the same time we examined the trend of impedance magnitude standard deviation for every blood component, expressing it as percentage of its average value and illustrating them in Figure 6.15b. According to the results of Figure 6.15a and Figure 6.15b, the optimal frequency revealed to be 10^4 Hz because, at this frequency, all the blood components can be accurately and completely discriminated in terms of impedance magnitude from the adjacent ones, also in the worst case. Figure 6.15c shows the discrimination of blood components at 10^4 Hz.

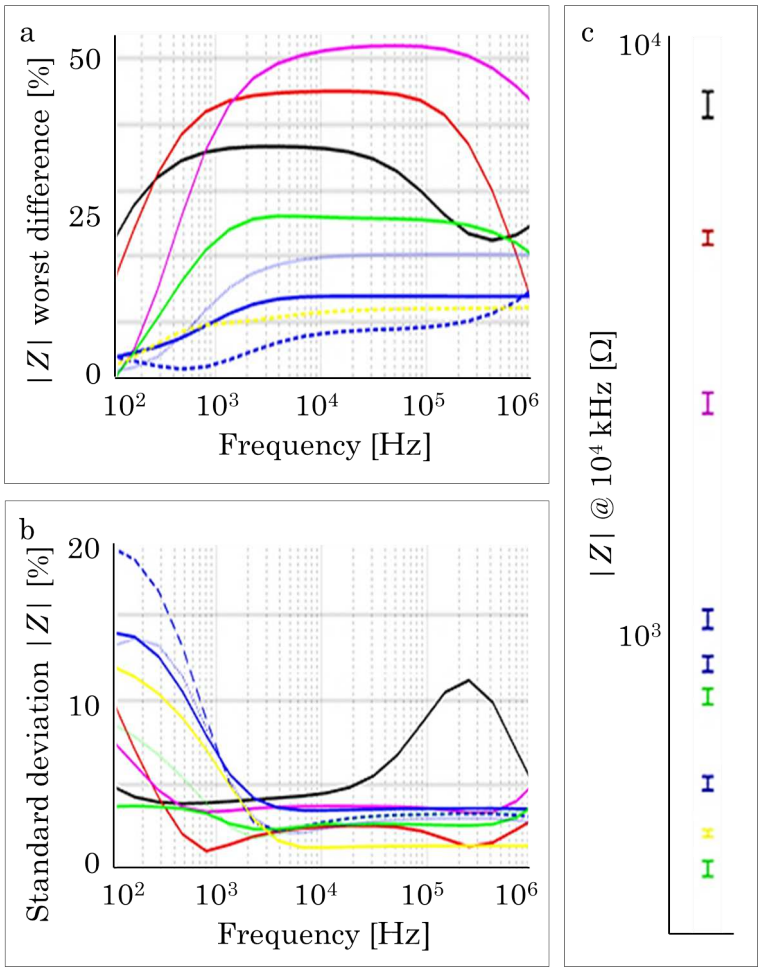

Figure 6.15: ***Optimal frequency quantification for single-frequency measurements.*** *Worst percentage differences in impedance magnitude between adjacent blood components (a). Impedance magnitude standard deviation for each blood component, expressed as percentage of the related average value (b). Impedance magnitude at* 10^4 *Hz (c), where each blood component is represented in terms of mean and standard deviation (n = 20).*

6.4.3 Blood hematocrit detection

Hematocrit is the volume of red blood cells as a percentage of the whole blood volume and its value can give information about transport and storage conditions quality. Hematocrit is a crucial parameter to identify and quantity density variations or aggregative states in blood samples, situations of alteration that makes blood unsuitable for analyses and not compatible with transfusion. The hematocrit of each whole blood sample was measured with a commercial instrument, commonly and daily used in clinical laboratories, and compared with the impedance magnitude of each same sample measured at 10^4 Hz. As shown in Figure 6.16, measuring the impedance with the proposed sensor we are able to rapidly achieved the related hematocrit value. In fact, the data

appear highly correlated, with a Pearson's correlation coefficient $r = 0.89$ and the correlation can be linearly approximated with the relation $y = 62.9x + 6.8$, where y represents the impedance magnitude and x represents the hematocrit values. The obtained results show that the proposed measuring system can be used to detect rapidly the blood hematocrit level.

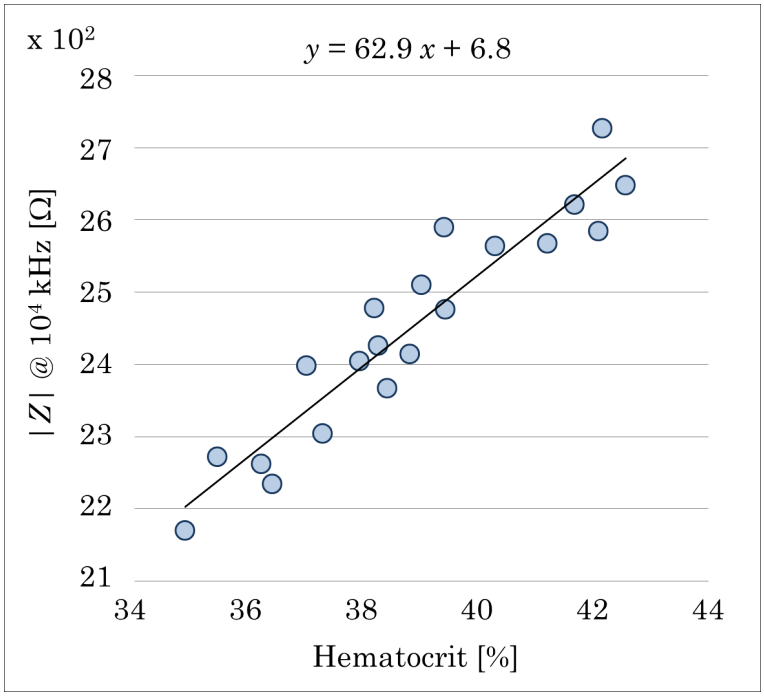

Figure 6.16: ***Quantitative comparison between impedance magnitude at*** 10^4 ***Hz and the hematocrit measured in laboratory, for whole blood samples.*** *Data are highly correlated (Pearson's correlation coefficient* $r = 0.89$*) and the correlation is linearly represented by the equation* $y = 62.9x + 6.8$*, where* y *represents the impedance magnitude and* x *represents the hematocrit values.*

6.5 Live cells imaging with FluoLab

6.5.1 Calcium signaling in mitochondria-related diseases

Early and minimally-invasive diagnostics has become a prerogative in medicine. Platelets are circulating blood particles without a nucleus, whose activation is characterized and identifiable by a series of cytosolic calcium ions movements and spikes. Mitochondria are organelles whose presence in platelets influences their metabolic physiological functions, both in healthy and pathological conditions. Calcium signaling, in terms of magnitude and frequency of oscillations, could help in revealing the platelets pathophysiology and in recognizing mitochondrial diseases. Thus, invasive tests could be substituted with calcium

signaling in platelets as an alternative and minimally-invasive diagnostic tool to study mitochondria-related diseases.

In medical diagnostics physicians need useful tools and instruments able to identify and discriminate normal and abnormal platelets responses. Platelets do not possess a nucleus, for ages considered the exclusive regulator center of cells activity. Otherwise, interestingly, they exhibit a spatiotemporal complexity in calcium ions Ca^{2+} signaling that is typical of nucleated cells. The release of calcium from platelet stores induces a variety of cellular responses that can affect many biological processes, first of all the exposure of membrane receptors that facilitate platelets adhesion and thrombus formation on different adhesive surfaces. In the last years, mitochondria have been identified as sensors and regulators of calcium signals in platelets and, recently, attention moved towards the assessment of functional correlation between platelets and mitochondria to understand the basis of several human diseases.

Herein, a specific calcium signal processing with Fluolab for the investigation of platelet response to estrogen receptors (ERs) engagement is presented. In fact, venous thrombosis represents a factor risk in oral estrogen treatments and platelets are involved in these processes through ERs expressed on their membrane. Beta-ERs (ERβ) and alpha-ERs (ERα) have been detected in human platelets and also in their mitochondria and the different response of ERs could influence the procoagulant activity of platelets, not only in terms of alteration and variation of platelet energy, but also in terms of modulation of Ca^{2+} ions or soluble mediators release. With FluoLab it was possible for the first time to rapidly and easily extract and analyze cytosolic Ca^{2+} signals in platelets and correlated them to Ca^{2+} movements in mitochondria (Figure 6.17), in the specific examination of estrogen treatment effects. According to

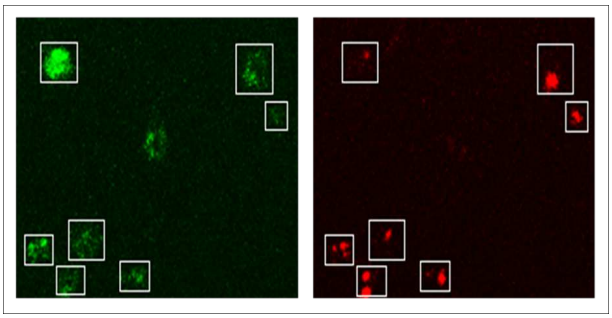

Figure 6.17: ***Extraction of cytosolic Ca^{2+} signals in platelets and correlation to Ca^{2+} movements in mitochondria.*** *Example of a couple of a green and a red image showing the FLUO 3-AM and the RHOD 2-AM fluorescence emission, respectively. In the green image rectangular ROIs were defined around platelets, while in the corresponding ROIs of the red image active mitochondria are visible.*

the obtained results, it has been demonstrated that differences in ERs response in platelets and, more specifically, in mitochondria lead to different metabolic functional effects. Thus FluoLab could be seen as an alternative minimally-

invasive tool to identify and quantitatively investigate the calcium signaling in mitochondria-related diseases.

Various reagents were added to the blood cell suspension before perfusion. These included the selective ERs agonists ligands propylpyrazolepriol (PPT, 10 μM final concentration) for ERα and diarylpropionitrile (DPN, 10 μM final concentration) for ERβ. In some experiments platelets were also incubated with 17β-estradiol (10 nM final concentration), the natural endogenous hormone ligands for ERβ. Typical calcium signals related to cytosolic oscillations are shown in Figure 6.18. The role of ERs in platelets labeled with FLUO 3-AM has been investigated analyzing the effects of ERs agonists under flow, in terms of variation of $[Ca^{2+}]$ signals in single platelets. In particular the right column of Figure 6.18 displays cytosolic calcium signals in an untreated representative situation of control and the effects of PPT and 17β-estradiol in terms of signal variation. In order to visibly appreciate the signal differences, for every experimental condition only 3 representative single platelet traces among those analyzed. Untreated platelets exhibit peaks ($[Ca^{2+}]_{Max}$) of 1.27 $\pm$ 0.15 μM. While treatment with PPT seems to not have effects on cytosolic calcium concentration ($[Ca^{2+}]_{Max}$ = 1.26 $\pm$ 0.11 μM), with 17β-estradiol platelets appear more activated, with a $[Ca^{2+}]_{Max}$ that reaches the value of 2.12 $\pm$ 0.21 μM. One of the most interesting results is represented by the effect of DPN addition in all the three situations mentioned above, as presented in the left columns of the Figure 6.18. DPN acts always lowering $[Ca^{2+}]$ levels. The reduction of cytosolic calcium oscillations with DPN is thus visibly considerable: $[Ca^{2+}]$ traces exhibit peaks of $[Ca^{2+}]_{Max} = 0.65 \pm 0.13$ μM, compared to the untreated situation of control, while calcium concentration levels reaches values of 0.72 $\pm$ 0.15 μM and 0.68 $\pm$ 0.16 μM adding DPN to PPT and 17β-estradiol, respectively, as presented in the Figure 6.18. One of the most interesting results is represented by the effect of DPN addition in all the three situations mentioned above, as presented in the left columns of the Figure 6.18. DPN acts always lowering $[Ca^{2+}]$ levels. The reduction of cytosolic calcium oscillations with DPN is thus visibly considerable: $[Ca^{2+}]$ traces exhibit peaks of $[Ca^{2+}]_{Max} = 0.65 \pm 0.13$ μM, compared to the untreated situation of control, while calcium concentration levels reaches values of 0.72 $\pm$ 0.15 μM and 0.68 $\pm$ 0.16 μM adding DPN to PPT and 17β-estradiol, respectively, as presented in the Figure 6.18.

It is important to notice that DPN and 17β-estradiol are different ligands for the same receptor, but they show opposite effects on platelet activity. The emerging studies about mitochondrial signaling pathways addressed us towards the investigation of this surprising outcome through the analysis of the functional correlation between cytosolic calcium variations and mitochondrial calcium movements. In the Figure 6.19 the black traces represent single platelet cytosolic calcium fluorescence, extracted from FLUO 3-AM green images, while red traces represent single mitochondrion calcium fluorescence and were measured from RHOD 2-AM red images. Signals magnitudes are repre-

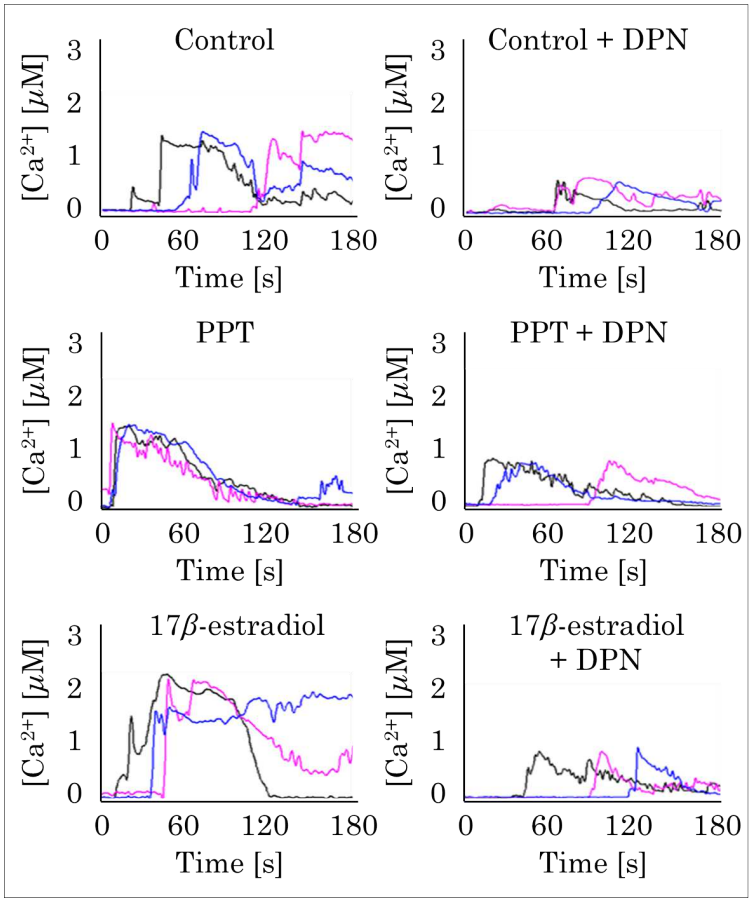

Figure 6.18: ***Cytosolic calcium concentration in platelets labeled with FLUO 3-AM under different experimental treatments.*** *The right column shows calcium signals in an untreated situation of control and the effects of PPT and 17β-estradiol on cytosolic calcium oscillations. The left column shows the effect of DPN addition in control, PPT and 17β-estradiol. Traces are representative of a single platelet.*

sented in terms of mean fluorescence intensity (MFI), in arbitrary units (AU) from 0 to 255. It is noticeable that mitochondrial calcium movement in terms of shape of calcium variation in time in single mitochondria influences the cytosolic calcium signal in platelets and, thus, platelet activation. In this way the regulator role of mitochondria on platelets metabolism and activity was confirmed. In addition, for the first time, the mitochondrial Ca^{2+} buffering was identified as the key trigger in shaping amplitude and patterns of cytosolic Ca^{2+} in platelets, as shown in the Figure 6.19. The 17β-estradiol activates more mitochondria than the DPN and the activation persists in time sustaining and feeding also the cytosolic calcium. With DPN, instead, mitochondria are not able to remain active for a long time and, consequently, the cytosolic calcium does not reach high levels and soon after decreases.

Platelets are considered accessible and valuable to study mitochondrial

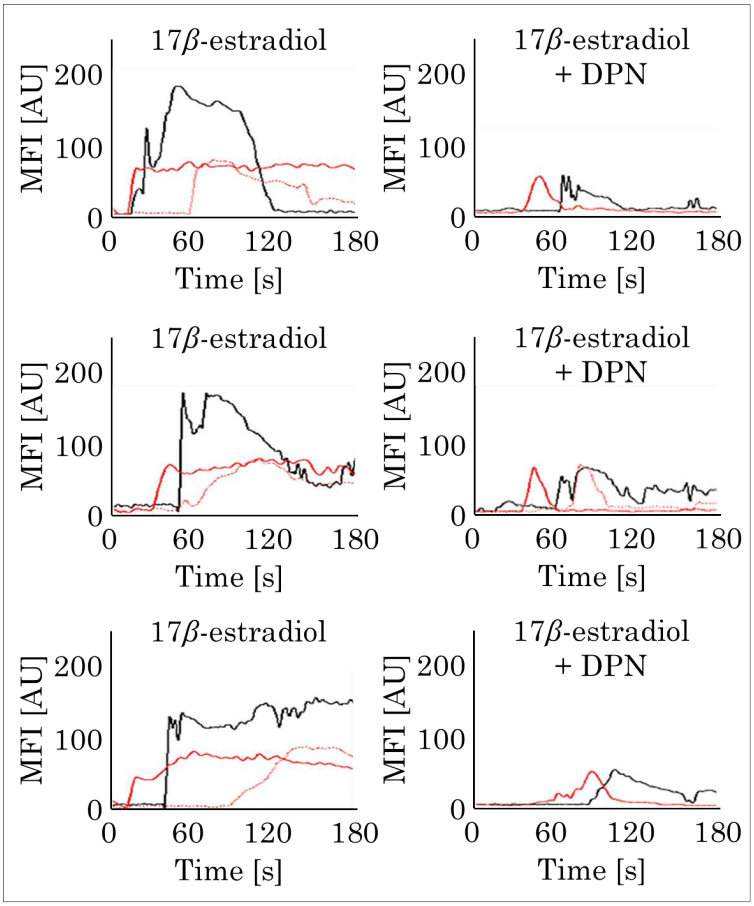

Figure 6.19: ***The effect of DPN addition on cytoplasmic and mitochondrial calcium oscillations.*** *Black traces represent single platelet cytosolic calcium fluorescence, extracted from FLUO 3-AM green images, while red traces represent single mitochondrion calcium fluorescence and were measured from RHOD 2-AM red images. The right and the left columns show the correlation between cytosolic calcium signals and mitochondrial ones in platelets treated with 17β-estradiol and DPN, respectively. The addition of DPN readly reverse the red lines. In fact, the mitochondrial calcium heavily influence the Ca^{2+} cytosolic oscillation. Signals magnitudes are represented in terms of mean fluorescence intensity (MFI), in arbitrary units (AU) from 0 to 255.*

functions, owing to their greater content of fully functional mitochondria compared with other metabolically active organelles. Mitochondria in platelets have functions far more than thrombogenesis regulation and, alongside this, here we have shown a real perspective of application of calcium signaling in the development of potential biomarkers of platelet mitochondrial dysfunction in mitochondria-related diseases. The close relationship between mitochondrial and cytosolic calcium oscillations was for the first time quantified and specifically analized. In particular, acting on the ERα, with the agonist PPT, the cytosolic calcium variations revealed comparable to those of control, while

17β-estradiol, which acts on ERβ, significantly increased platelet activation in terms of cytosolic [Ca^{2+}] peaks.

6.5.2 Discovery of new communication pathways in megakaryocytes (MKs)

A rectangular region of interest (ROI) was defined around each megakaryocyte (MK), tangent to its surface. The MFI value was thus quantified at each temporal instant to obtain a time series or signal of MFI values for each megakaryocyte, related to its calcium variations and characterized by a cyclic recurrence of peaks or clusters of peaks. With the purpose of analyzing the oscillations of calcium movements, in the MFI signal of each megakaryocyte two different periodicities were automatically identified and extracted. The first periodicity, called p, was computed as the mean of all the peak-peak intervals, while the second one, named P, was evaluated as the average time between the first peak of a cluster of peaks and the first peak of the following cluster. Moreover, these two temporal intervals were investigated and linked with the number of nuclei visibly identified in each related megakaryocyte.

In addition, couples of MFI signals were analyzed with the aim of finding possible correlations in in the calcium variations of megakaryocytes adhering one after the other, in the flow direction, but without a physical contact. In particular, for each couple of MFI signals, the time between the peaks in the megakaryocyte upstream, according to the flow direction, and the peaks that appear as an evident consequence in the following megakaryocyte was measured. This time delay, quantified as the mean representative value of all the time shifts calculated in the couple, was correlated to the distance, along the flow direction, between the two megakaryocyte centroids. The ratio of the megakaryocytes distance with the time that elapses between their peaks can be defined as their stimulus transmission speed and, due to the fact that is common to all the megakaryocyte couples, it reveals and demonstrates their communication through the blood flow. Finally, for each megakaryocyte, other ROIs were defined to study calcium movements in the cytoplasmic and nuclear regions, separately, through a local MFI signals quantification. The MFI time series for these regions were quantified as just described. After the automatic identification of peaks, the time delay between each calcium peak in cytoplasm and the consequential calcium peaks in nuclei was measured as representative temporal parameter of calcium movement from cytoplasm to nuclei.

We noticed that p is correlated to the cellular calcium movement inside each megakaryocyte and it varies specifically among the MKs. Differently, P can be considered as a sort of inter-cellular communication periodicity because it is evidently common to all megakaryocytes, have nothing to do with the single dimension or structure of the specific MKs. This inter-cellular periodicity measures $P = 36.34 \pm 3.30$ s and the most surprising result is that, multiplying every p to the number of nuclei N of each related megakaryocyte, we obtain

$p\Delta N = 34.52 \pm 2.58$ s, value evidently equal to P. This outcome allows to discriminate and relate, at the same time, the 2 cellular communication pathways whose signaling contributes in megakaryocytes. In order to investigate if downstream megakaryocytes calcium release, according to the flow direction, could be able to influence upstream megakaryocytes calcium signal, the MFI signal of two spatially near MKs have been analyzed and matched. Surprisingly, there a real correlation between MKs was discovered and quantified for the first time. In fact, thanks to calcium release, cells are able to communicate and functionally influence each other. A calcium peak from a downstream cell induces a calcium flashes sequence in the upstream near megakaryocyte, after a specific time delay depending on the MKs distance. This aspect seemed to be not limited in time because this lasting cyclic metabolic influence suggests the presence of a continuous calcium reuptake, visible and measurable also in the absence of external calcium, therefore representing the result of an intercellular calcium movement. The ratio of the distance between 2 megakaryocytes with their peaks time delay can be defined as the stimulus transmission speed. The MKs transmission velocity of calcium signal measures 23.03 ± 1.48 μm/s. Calcium movement in megakaryocytes was also investigated analyzing local MFI signals of cytoplasmic and nuclear regions, as described. Calcium moves from cytoplasm to nuclei in 303.77 ± 73.07 s. An example of a visible communication among MKs through the flow is shown in the Figure 6.20.

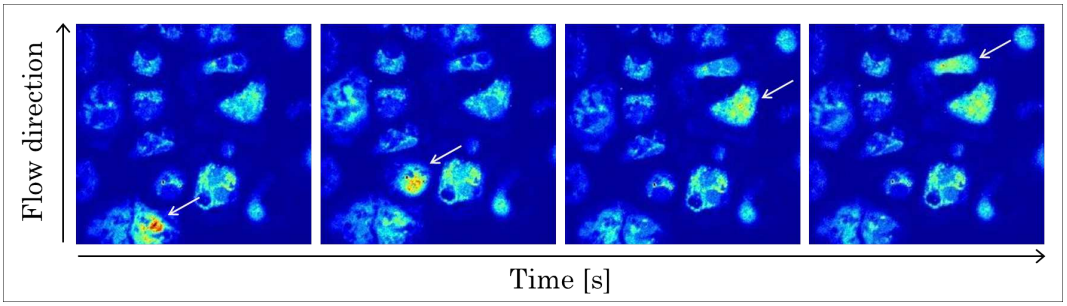

Figure 6.20: ***Communication among megakaryocytes.*** *Thanks to calcium release, cells are able to communicate and functionally influence each other. A calcium peak from a downstream cell induces a calcium flashes sequence in the upstream near megakaryocyte, after a specific time delay depending on the MKs distance.*

7. Conclusions

Medical research has moved gradually its attention to new non-invasive and real-time devices able to assess the thrombotic risk profile by reconstructing the dynamic of thrombus formation events and thus allowing the monitoring of anticoagulant and antiplatelet therapies. In the specific biological field of blood coagulation and its related diseases, the accuracy and the standardization of thrombus volume measurements, starting from confocal microscope images, have always been subject of intense investigation. However, the translation in clinical practice has been prevented because of the high costs and dimensions. Impedance measurements applied to blood analysis have received a considerable attention because of the possibility of monitoring in real-time the thrombus formation in vitro.

In order to improve the thrombus measurement accuracy, perfusion experiments have been performed for a total time of 300 seconds, measuring impedance magnitude at different frequencies, choosing in a second time the frequency of 150 kHz and simultaneously acquiring optical 2D images. At the end of each blood perfusion a z-stack has been acquired, which elaboration allowed to confirm the validity of the new device performances. After comparing the results obtained with the optical thresholding ones and after verifying their interchangeability, it was noticeable that the real-time monitoring of the individual hemostatic behavior is possible also through the only acquisition of the impedance signals and their representation in terms of relative variation of impedance magnitude $|\Delta Z|$ [%].

A fast, competitive and innovative device for the in vitro determination of thrombus formation under flow has been described. In particular, the sensor is capable of discriminating different hemostatic conditions as demonstrated by the presented results. This should be helpful to evaluate in vitro the thrombotic risk of individuals, both healthy and affected by cardiovascular diseases or other thromboembolic disorders. However, large clinical studies should be undertaken to investigate the impact of our in vitro methodology and thus to contribute to a more accurate understanding of thrombosis and therapies resistance. According to the obtained results, the biosensor can be proposed as a point of care device to adequately monitor antiplatelet therapies and pharmacologic treatments and for the construction of models with the aim of optimizing the anticoagulant treatments.

The accuracy and the standardization of thrombus volume measurements,

starting from confocal microscope images, have always been open and problematic issues. In the specific biological field of blood coagulation and cardiovascular diseases, the possibility to reconstruct and measure the individual platelet thrombi formed on different adhesive surfaces is of considerable importance for studying platelets functions and dynamic processes that involve them. The proposed algorithm allows a fast and accurate compensation of distortion effects and of the related volume overestimation. The algorithm computes a realistic and accurate volume estimation offering new perspectives in terms of standardization, inter-laboratory communication, calibration of other devices, medical diagnostics and measurements reliability.

The obtained results aim at compensating the systematic error arising when a volume is estimated from confocal z-stacks of images with benchmark commercial methods like ImageJ or Volocity. The analysis indicates that the overestimation with all the benchmark methods is proved by compatible intervals for all the populations of considered objects, that are beads, small platelet aggregates and large platelet aggregates. The overestimation error could be acceptable and treated as a common offset between measurements only in investigations about the functional effect of a substance. In medical diagnostics, instead, this overestimation is not acceptable (i.e. in tumor mass estimation). Hence, it should mandatory to compute a realistic and accurate volume measurement. The new fast calibration algorithm presented could be applied also to different objects even characterized by an irregular shape, or to clusters of objects.

Strategies in the field of risk management and patient safety are aimed at the prevention, detection and reduction of critical events through the analysis of errors that can be measured and compensated. In clinical laboratories, the majority of critical issues occurs in the pre-analytical phase, especially in the activities where the human contribution is still decisive. Information provided by clinical laboratories affects almost the totality of clinical decisions about diagnoses and treatments. Thus, the current focus of healthcare institutions is the improvement of patient safety having more attention in avoiding pre-analytical mistakes and preventing laboratory errors. Improvement of pre-analytical processes currently constitutes a challenge to be faced by clinical laboratories. The most frequent encountered situations are serum samples with hemolysis, in which their alteration is not highly visible and can compromise analyses results, and blood samples unsuitable for transfusion because of their inappropriate sampling and storage. There are different means and techniques today available to manage to manage these conditions, but the way towards a complete and effective rationalization of these laboratories is still long.

Another new simple impedance-based biosensor to perform fast impedance measurements in the pre-analytical phase has been presented and described. Different blood components have been measured and characterized in terms of impedance magnitude and phase. In particular, observing the impedance magnitude signals of serum and whole blood, an important outcome is rep-

resented by the identification of their upper thresholds of 700 Ω and 3 kΩ, respectively, as useful indicators of the quality of the samples in performing a fast check with this sensor. In addition, each blood component has been quantitatively described estimating the parameters of the equivalent circuit proposed and finding some interesting and coherent correlations between the experimental results and the physical characteristics of the system investigated. All these results, together with the interpolation of frequency points in the real-imaginary plot shown, confirmed the adequacy of the equivalent circuit chosen. The impedance analysis also allowed the quantitative identification of 10^4 Hz as the optimal frequency to perform single-frequency measurements with more efficiency and without losing accuracy. Finally, a correlation between the impedance magnitude of whole blood samples at 10^4 Hz and the hematocrit percentage value, measured in laboratory, was achieved and quantified. Thanks to the impedance measurements and the electrical characterization of different components of blood samples, a further optimization of costs, resources and means in performing quality controls, especially on serum and blood in the pre-analytic phase, has been proven to be feasible. Through static electrical impedance measurements and analysis, it is thus possible to carry out very fast and automated controls for every sample, thus reducing the risk of errors in laboratory analyses and limiting the propagation of these errors towards the patients health.

Finally, FluoLab revealed an easy-to-use tool and it still allows a multi-cell functional fast calcium ion signals analysis. In our laboratory it is fundamental and necessary to discover, discriminate and numerically characterize substances movements and communications signals inside cells or among cells, to discover new biological metabolic pathways and to automatize the computation reducing the processing time. With FluoLab important results have been achieved in the projects regarding the investigation of signaling pathways in platelets. In particular, new communication processes in platelets and in their precursors have been characterized for the first time and the signaling of specific estrogen receptors agonists in their interaction with platelets have been studying to investigate their effect on functionality and metabolism of platelets, with regard to a wider research project about estrogens and their relation with cancer development.

Bibliography

[1] M. Mazzucato, A. Santomaso, P. Canu, Z. M. Ruggeri, and L. DeMarco, "Flow dynamics and haemostasis," *Annali dell'Istituto Superiore di Sanità*, vol. 43(2), pp. 130–138, 2007, PMID: 17634661.

[2] Z. M. Ruggeri and S. P. Jackson, "Platelet thrombus formation in flowing blood," *Platelets*, pp. 399–423, 2013, https://doi.org/10.1016/B978-0-12-387837-3.00020-1.

[3] M. Mazzucato, M. R. Cozzi, P. Pradella, and Z. M. R. L. DeMarco, "Distinct roles of adp receptors in von willebrand factor-mediated platelet signaling and activation under high flow," *Blood*, vol. 104(10), pp. 3221–3227, 2004, https://doi.org/10.1182/blood-2004-03-1145, PMID: 15284110.

[4] R. VanKruchten, J. M. Cosemans, and J. W. Heemskerk, "Measurement of whole blood thrombus formation using parallel-plate flow chambers - a practical guide," *Platelets*, vol. 23(3), pp. 229–242, 2012, https://doi.org/10.3109/09537104.2011.630848, PMID: 22502645.

[5] R. Eils and C. Athale, "Computational imaging in cell biology," *Journal of Cell Biology*, vol. 161(3), pp. 477–481, 2003, https://doi.org/10.1083/jcb.200302097, PMID: 12743101.

[6] K. F. Lei, K. H. Chen, P. H. Tsui, and N. M. Tsang, "Real-time electrical impedimetric monitoring of blood coagulation process under temperature and hematocrit variations conducted in a microfluidic chip," *PLoS ONE*, vol. 8(10), p. e76243, 2013, https://doi.org/10.1371/journal.pone.0076243, PMID: 24116099.

[7] L. G. Puckett, G. Barrett, D. Kouzoudis, and C. G. L. G. Bachas, "Monitoring blood coagulation with magnetoelastic sensors," *Biosensors and Bioelectronics*, vol. 18, pp. 675–681, 2013, https://doi.org/10.1016/S0956-5663(03)00033-2, PMID: 12706578.

[8] D. Chen, S. Song, J. Ma, Z. Zhang, P. Wang, W. Liu, and Q. Guo, "Micro-electromechanical film bulk acoustic sensor for plasma and whole blood coagulation monitoring," *Biosensors and Bioelectronics*, vol. 91,

pp. 465–471, 2017, https://doi.org/10.1016/j.bios.2016.12.063, PMID: 28068607.

[9] Y. S. Zhang, F. Davoudi, P. Walch, A. Manbachi, X. Luo, V. DellErba, A. K. Miri, H. Albadawi, A. Arneri, X. Li, X. Wang, M. R. Dokmeci, A. Khademhosseini, and R. Oklu, "Bioprinted thrombosis-on-a-chip," *Lab on a Chip*, vol. 16, pp. 4097–4105, 2016, https://doi.org/10.1039/c6lc00380j, PMID: 27722710.

[10] K. Claesson, T. L. Lindahl, and L. Faxalv, "Counting the platelets: a robust and sensitive quantification method for thrombus formation," *Journal of Thrombosis and Haemostasis*, vol. 115(6), pp. 1178–1190, 2016, https://doi.org/10.1160/ TH15-10-0799, PMID: 26842994.

[11] B. R. Branchford, C. G. Ng, K. B. Neeves, and J. DiPaola, "Microfluidic technology as an emerging clinical tool to evaluate thrombosis and hemostasis," *Thrombosis Research*, vol. 136(1), pp. 13–19, 2015, https://doi.org/10.1016/j.thromres.2015.05.012, PMID: 26014643.

[12] M. Li, D. N. Ku, and C. R. Forest, "Microfluidic system for simultaneous optical measurement of platelet aggregation at multiple shear rates in whole blood," *Lab on a Chip*, vol. 12(7), pp. 1355–1362, 2012, https://doi.org/10.1039/ c2lc21145a, PMID: 22358184.

[13] E. Westein, S. D. Witt, M. Lamers, J. M. Cosemans, and J. W. Heemskerk *Platelets*, vol. 23(7), pp. 1355–1362, 2012, https://doi.org/10.3109/09537104.2012.709653, PMID: 22873212.

[14] L. Bonanno and L. A. DeLouise, "Whole blood optical biosensor," *Biosensors and Bioelectronics*, vol. 23(3), pp. 444–448, 2012, https://doi.org/10.1016/j.bios.2007.05.008, PMID: 17720473.

[15] M. Roest, A. Reininger, J. J. Zwaginga, M. R. King, and J. W. Heemskerk, "Flow chamber-based assays to measure thrombus formation in vitro: requirements for standardization," *Journal of Thrombosis and Haemostasis*, vol. 9(11), pp. 2322–2324, 2012, https://doi.org/10.1111/j.1538-7836.2011.04492.x, PMID: 22947397.

[16] E. Barsoukov and J. R. Macdonald, *Impedance spectroscopy: theory, experiment, and applications*. J. Wiley and Sons Inc., Hoboken, New Jersey, 2nd ed., March 2005, ISBN: 978-0-471-64749-2.

[17] A. Affanni, R. Specogna, and F. Trevisan, "Measurement bench for impedance tomography during hemostasis process in whole blood," *IEEE MeMeA - International Symposium on Medical Measurements and Applications*, pp. 80–83, 2011, https://doi.org/ 10.1109/MeMeA.2011.5966668.

[18] A. Affanni, G. Chiorboli, R. Specogna, and F. Trevisan, "Uncertainty model of electro-optical thrombus growth estimation for early risk detection," *Measurement*, vol. 79, pp. 260–266, 2016, https://doi.org/10.1016/j.measurement.2015.05.045.

[19] A. Affanni, G. Chiorboli, L. Codecasa, M. Cozzi, L. DeMarco, M. Mazzucato, C. Morandi, R. Specogna, M. Tartagni, and F. Trevisan, "A novel inversion technique for imaging thrombus volume in microchannels fusing optical and impedance data," *IEEE Transactions on Magnetics*, vol. 50(2), 2014, https://doi.org/10.1109/TMAG.2013.2281987.

[20] A. Affanni, R. Specogna, and F. Trevisan, "Combined electro-optical imaging for the time evolution of white thrombus growth in artificial capillaries," *IEEE Transactions on Instrumentation and Measurement*, vol. 62(11), p. 2954–2959, 2013, https://doi.org/10.1109/TIM.2013.2266012.

[21] A. Affanni, R. Specogna, and F. Trevisan, "Ex vivo time evolution of thrombus growth through optical and electrical impedance data fusion," *Journal of Physics: Conference Series*, vol. 459(1), 2013, https://doi.org/10.1088/1742-6596/459/1/012016.

[22] A. Affanni, R. Specogna, and F. Trevisan, "A discrete geometric approach to cell membrane and electrode contact impedance modeling," *IEEE Transactions on Biomedical Engineering*, vol. 59(9), pp. 2619–2627, 2012, https://doi.org/10.1109/TBME.2012.2207897, PMID: 22801483.

[23] A. Affanni, R. Specogna, and F. Trevisan, "Electrical impedance spectroscopy on flowing blood to predict white thrombus formation in artificial microchannels," *IEEE I2MTC - International Instrumentation and Measurement Technology Conference Proceedings*, p. 1477–1480, 2012 Graz (Austria), https://doi.org/10.1109/I2MTC.2012.6229295.

[24] D. Kang, D. Suh, and J. Ra, "Three-dimensional blood vessel quantification via centerline deformation," *IEEE Transactions on Medical Imaging*, vol. 28(3), pp. 405–414, 2009, https://doi.org/10.1109/TMI.2008.2004651, PMID: 19244012.

[25] E. Kollorz, D. Hahn, R. Linke, T. Goecke, J. Hornegger, and T. Kuwert, "Quantification of thyroid volume using 3d ultrasound imaging," *IEEE Transactions on Medical Imaging*, vol. 27(4), pp. 457–466, 2008, https://doi.org/10.1109/TMI.2007.907328, PMID: 18390343.

[26] J. Dehmeshki, X. Ye, H. Amin, M. Abaei, X. Lin, and S. D. Qanadli, "Volumetric quantification of atherosclerotic

plaque in ct considering partial volume effect," *IEEE Transactions on Medical Imaging*, vol. 26(3), pp. 273–282, 2007, https://doi.org/10.1109/TMI.2007.893344, PMID: 17354634.

[27] Y. Masutani, H. MacMahon, and K. Doi, "Computerized detection of pulmonary embolism in spiral ct angiography based on volumetric image analysis," *IEEE Transactions on Medical Imaging*, vol. 21(12), pp. 1517–1523, 2002, https://doi.org/10.1109/TMI.2002.806586, PMID: 12588035.

[28] M. M. Frigault, J. Lacoste, J. Swift, and C. Brown, "Live-cell microscopy - tips and tools," *Journal of Cell Science*, vol. 122, pp. 753–767, 2009, https://doi.org/10.1242/jcs.033837, PMID: 19261845.

[29] J. C. Waters, "Accuracy and precision in quantitative fluorescence microscopy," *Journal of Cell Biology*, vol. 185(7), pp. 1135–1148, 2009, https://doi.org/10.1083/jcb.200903097, PMID: 19564400.

[30] J. B. Pawley, *Handbook of biological confocal microscopy*. Springer Science Business Media LLC, New York, 3rd ed., 2006, ISBN: 978-0-387-25921-5.

[31] R. M. Schoeman, M. Lehmann, and K. B. Neeves, "Flow chamber and microfluidic approaches for measuring thrombus formation in genetic bleeding disorders," *Platelets*, vol. 28(5), pp. 463–471, 2017, https://doi.org/10.1080/09537104.2017.1306042, PMID: 28532218.

[32] R. Schoeman, K. Rana, N. Danes, M. Lehmann, J. A. D. Paola, A. L. Fogelson, K. Leiderman, and K. B. Neeves, "A microfluidic model of hemostasis sensitive to platelet function and coagulation," *Cellular and Molecular Bioengineering*, vol. 10(1), pp. 3–15, 2017, https://doi.org/10.1007/s12195-016-0469-0, PMID: 28529666.

[33] Y. Zheng, J. Chen, M. Craven, N. W. Choi, S. Totorica, A. DiazSantana, P. Kermani, B. Hempstead, C. FischbachTeschl, J. Lopez, and A. Stroock, "In vitro microvessels for the study of angiogenesis and thrombosis," *Proceedings of the National Academy of Sciences of the United States of America*, vol. 109(24), pp. 9342–9347, 2012, https://doi.org/10.1073/pnas.1201240109, PMID: 22645376.

[34] W. S. Nesbitt, S. Giuliano, S. Kulkarni, S. M. Dopheide, I. S. Harper, and S. P. Jackson, "Intercellular calcium communication regulates platelet aggregation and thrombus growth," *Journal of Cell Biology*, vol. 160(7), pp. 1151–1161, 2003, https://doi.org/10.1083/jcb.200207119, PMID: 12668663.

[35] A. L. Plant, L. E. Locascio, W. E. May, and P. D. Gallagher, "Improved reproducibility by assuring confidence in measurements in biomedical research," *Nature Methods*, vol. 11(9), pp. 895–898, 2014, https://doi.org/10.1038/nmeth.3076, PMID: 25166868.

[36] G. L. Mendolicchio, D. Zavalloni, M. Bacci, E. Corrada, M. Marconi, C. Lodigiani, P. Presbitero, L. Rota, and Z. M. Ruggeri, "Variable effect of p2y12 inhibition on platelet thrombus volume in flowing blood," *Journal of Thrombosis and Haemostasis*, vol. 9(2), pp. 373–382, 2011, https://doi.org/10.1111/j.1538-7836.2010.04144.x, PMID: 21083646.

[37] N. Pugh, A. M. Simpson, P. A. Smethurst, P. G. DeGroot, N. Raynal, and R. W. Farndale, "Synergism between platelet collagen receptors defined using receptor-specific collagen-mimetic peptide substrata in flowing blood," *Journal of Thrombosis and Haemostasis*, vol. 115(24), pp. 5069–5079, 2010, https://doi.org/10.1182/blood-2010-01-260778, PMID: 20351310.

[38] M. Mazzucato, M. R. Cozzi, M. Battiston, M. Jandrot-Perrus, M. Mongiat, P. Marchese, T. J. Kunicki, Z. M. Ruggeri, and L. DeMarco, "Distinct spatio-temporal ca2+ signaling elicited by integrin alpha2beta1 and glycoprotein vi under flow," *Blood*, vol. 114(13), pp. 2793–2801, 2009, https://doi.org/10.1182/blood-2008-12-193490, PMID: 19622836.

[39] A. Celi, G. MerrillSkoloff, P. Gross, S. Falati, D. S. Sim, R. Flaumenhaft, B. C. Furie, and B. Furie, "Thrombus formation: direct real-time observation and digital analysis of thrombus assembly in a living mouse by confocal and widefield intravital microscopy," *Journal of Thrombosis and Haemostasis*, vol. 1(1), pp. 60–68, 2003, https://doi.org/10.1046/j.1538-7836.2003.t01-1-00033.x, PMID: 12871540.

[40] Z. M. Ruggeri, J. A. Dent, and E. Saldivar, "Contribution of distinct adhesive interactions to platelet aggregation in flowing blood," *Blood*, vol. 94(1), pp. 172–178, 1999, PMID: 10381510.

[41] B. Savage, M. H. Ginsberg, and Z. M. Ruggeri, "Influence of fibrillar collagen structure on the mechanisms of platelet thrombus formation under flow," *Blood*, vol. 94(8), pp. 2704–2715, 1999, PMID: 10515874.

[42] B. Savage, F. Almus-Jacobs, and Z. M. Ruggeri, "Specific synergy of multiple substrate-receptor interactions in platelet thrombus formation under flow," *Cell*, vol. 94(5), pp. 657–666, 1998, https://doi.org/10.1016/S0092-8674(00)81607-4, PMID: 9741630.

[43] J. M. Murray, P. L. Appleton, J. R. Swedlow, and J. C. Waters, "Evaluating performance in three-dimensional fluorescence microscopy," *Journal of Microscopy*, vol. 228(3), pp. 390–405, 2007, https://doi.org/10.1111/j.1365-2818.2007.01861.x, PMID: 18045334.

[44] T. Visser and J. Oud, "Volume measurements in three-dimensional microscop," *Scanning*, vol. 16(4), pp. 198–200, 1994, https://doi.org/10.1002/sca.4950160403, PMID: 19564400.

[45] S. Hell, G. Reiner, C. Cremer, and E. H. Stelzer, "Aberrations in confocal fluorescence microscopy induced by mismatches in refractive index," *Journal of Microscopy*, vol. 169(3), pp. 391–405, 1993, https://doi.org/10.1111/j.1365-2818.1993.tb03315.x.

[46] Y. Hiraoka, J. Sedat, and D. Agard, "Determination of three-dimensional imaging properties of a light microscope system. partial confocal behavior in epifluorescence microscopy," *Biophysical Journal*, vol. 57(2), pp. 325–333, 1990, https://doi.org/10.1016/S0006-3495(90)82534-0, PMID: 2317554.

[47] G. Lippi, M. Plebani, and A. M. Simundic, "Quality in laboratory diagnostics: from theory to practice," *Biochemia Medica*, vol. 20(2), pp. 126–130, 2010, https://doi.org/10.11613/BM.2010.014.

[48] G. LimaOliveira, W. Volanski, G. Lippi, G. Picheth, and G. C. Guidi, "Pre-analytical phase management: a review of the procedures from patient preparation to laboratory analysis," *Scandinavian Journal of Clinical and Laboratory Investigation*, vol. 77(3), pp. 153–163, 2017, https://doi.org/10.1080/00365513.2017.1295317, PMID: 28266238.

[49] M. Plebani, L. Sciacovelli, A. Aita, A. Padoan, and M. L. Chiozza, "Quality indicators to detect pre-analytical errors in laboratory testing," *Clinica Chimica Acta*, vol. 432, pp. 44–48, 2014, https://doi.org/10.1016/j.cca.2013.07.033, PMID: 4012653.

[50] G. Lippi, G. C. Guidi, C. Mattiuzzi, and M. Plebani, "Preanalytical variability: the dark side of the moon in laboratory testing," *Clinical Chemistry and Laboratory Medicine*, vol. 44(4), pp. 358–365, 2006, https://doi.org/10.1515/CCLM.2006.073, PMID: 16599826.

[51] P. Carraro and M. Plebani, "Process control reduces the laboratory turnaround time," *Clinical Chemistry and Laboratory Medicine*, vol. 40(4), pp. 421–422, 2002, https://doi.org/10.1515/CCLM.2002.068, PMID: 12059086.

[52] G. Lippi, M. Plebani, and E. J. Favaloro, "Technological advances in the hemostasis laboratory," *Seminars in Thrombosis and Hemostasis*, vol. 40(2), pp. 178–185, 2014, https://doi.org/10.1055/s-0033-1364206, PMID: 24443219.

[53] G. Lippi, G. L. Salvagno, N. Blanckaert, D. Giavarina, S. Green, S. Kitchen, V. Palicka, A. J. Vassault, and M. Plebani, "Multicenter evaluation of the hemolysis index in automated clinical chemistry systems,"

Clinical Chemistry and Laboratory Medicine, vol. 47(8), pp. 934–939, 2009, https://doi.org/10.1515/CCLM.2009.218, PMID: 19548845.

[54] K. C. Gersh, C. Nagaswami, and J. W. Weisel, "Fibrin network structure and clot mechanical properties are altered by incorporation of erythrocytes," *Thrombosis and Haemostasis*, vol. 102(6), pp. 1169–1175, 2009, https://doi.org/10.1160/TH09-03-0199, PMID: 19967148.

[55] C. F. R. Rizzuto, *Imaging living cells*. Springer Science Business Media LLC, New York, 1998, ISBN: 978-3-642-60003-6.

[56] L. Mackay, N. Mikolajewicz, S. V. Komarova, and A. Khadra, "Systematic characterization of dynamic parameters of intracellular calcium signals," *Frontiers in Physiology*, vol. 7, p. eCollection, 2016, https://doi.org/0.3389/fphys.2016.00525, PMID: 27891096.

[57] M. V. Thomas, *Techniques in calcium research*. Academic Press, Cambridge, Massachusetts, 1982, ISBN: 0-1268-8680-6.

[58] M. D. Bootman, "Calcium signaling," *Cold Spring Harbor Perspectives in Biology*, vol. 4(7), p. a011171, 2012, https://doi.org/10.1101/cshperspect.a011171, PMID: 22751152.

[59] C. Giorgi, A. Romagnoli, P. Pinton, and R. Rizzuto, "Ca2+ signaling, mitochondria and cell death," *Current Molecular Medicine*, vol. 8(2), pp. 119–130, 2008, https://doi.org/10.2174/156652408783769571, PMID: 18336292.

[60] M. Fritzsche, R. A. Fernandes, H. ColinYork, A. M. Santos, S. F. Lee, B. C. Lagerholm, S. J. Davis, and C. Eggeling, "Calquo: automated, simultaneous single-cell and population-level quantification of global intracellular ca2+ responses," *Scientific Reports*, vol. 5, p. 16487, 2015, https://doi.org/10.1038/srep16487, PMID: 26563585.

[61] L. C. Wong, B. Lu, K. W. Tan, and M. Fivaz, "Fully-automated image processing software to analyze calcium traces in populations of single cells," *Cell Calcium*, vol. 48(5), pp. 270–274, 2010, https://doi.org/10.1016/j.ceca.2010.09.008, PMID: 20952058.

[62] E. A. Mukamel, A. Nimmerjahn, and M. J. Schnitzer, "Automated analysis of cellular signals from large-scale calcium imaging data," *Neuron*, vol. 63(6), pp. 747–760, 2009, https://doi.org/10.1016/j.neuron.2009.08.009, PMID: 19778505.

[63] J. Wenus, H. Dussmann, P. Paul, D. Kalamatianos, M. Rehm, P. Wellstead, J. Prehn, and H. Huber, "Alissa: an automated live-cell imaging system for signal transduction analyses," *Biotechniques*,

vol. 47(6), pp. 1033–1040, 2009, https://doi.org/10.2144/000113247, PMID: 20041856.

[64] M. R. Cozzi, G. Guglielmini, M. Battiston, S. Momi, E. Lombardi, E. C. Miller, D. DeZanet, M. Mazzucato, P. Gresele, and L. DeMarco, "Visualization of nitric oxide production by individual platelets during adhesion in flowing blood," *Blood*, vol. 125(4), pp. 697–705, 2015, https://doi.org/10.1182/blood-2014-06-579474, PMID: 25480660.

[65] C. DiBuduo, F. Moccia, M. Battiston, L. DeMarco, M. Mazzucato, R. Moratti, F. Tanzi, and A. Balduini, "The importance of calcium in the regulation of megakaryocyte function," *Haematologica*, vol. 99(4), pp. 769–778, 2014, https://doi.org/10.3324/haematol.2013.096859, PMID: 24463213.

[66] J. L. Mehta, "Influence of calcium-channel blockers on platelet function and arachidonic acid metabolism," *American Journal of Cardiology*, vol. 55(3), pp. B158–B164, 1985, https://doi.org/10.1016/0002-9149(85)90626-5, PMID: 2982252.

[67] L. Grajales, L. E. Lach, P. Janisch, D. L. Geenen, and J. Garcia, "Temporal expression of calcium channel subunits in satellite cells and bone marrow mesenchymal cells," *Stem Cell Reviews and Reports*, vol. 11(3), pp. 408–422, 2015, https://doi.org/10.1007/s12015-014-9566-4, PMID: 25277766.

[68] A. Siegman and S. Abboud, "Bioimpedance technique for monitoring cerebral artery stenosis in a 3d numerical model of the head," *Medical Engineering and Physics*, vol. 34(8), pp. 1095–1100, 2012, https://doi.org/10.1016/j.medengphy.2011.11.015, PMID: 22177574.

[69] R. Sharma and S. Sharma, *Physiology, Blood Volume.* StatPearls Publishing LLC, Treasure Island, Finland, September 2018, PMID: 30252333.

[70] H. F. VanBreugel, P. G. DeGroot, R. M. H. RM, and J. J. Sixma, "Role of plasma viscosity in platelet adhesion," *Blood*, vol. 80(4), pp. 953–959, 2009, PMID: 1498335.

[71] L. Holley, N. Woodland, W. T. Hung, K. Cordatos, and A. Reuben, "Influence of fibrinogen and haematocrit on erythrocyte sedimentation kinetics," *Biorheology*, vol. 36(4), pp. 287–297, 1999, PMID: 10690265.

[72] Z. Li, M. K. Delaney, K. A. OBrien, and X. Du, "Signaling during platelet adhesion and activation," *Arteriosclerosis, Thrombosis, and Vascular Biology*, vol. 30(12), p. 2341–2349, 2010, https://doi.org/10.1161/ATVBAHA.110.207522, PMID: 21071698.

[73] R. Colman, *Hemostasis and Thrombosis: Basic Principles and Clinical Practice*. Lippincott Williams and Wilkins, Filadelfia, Pennsylvania, 5th ed., 2006, ISBN: 978-0-781-74996-1.

[74] R. K. Andrews and M. C. Berndt, "Platelet physiology and thrombosis," *Thrombosis Research*, vol. 114, pp. 447–453, 2004, https://doi.org/10.1016/j.thromres.2004.07.020, PMID: 15507277.

[75] M. Chatterjee, J. E. Purvis, L. F. Brass, and S. L. Diamond, "Pairwise agonist scanning predicts cellular signaling responses to combinatorial stimuli," *Nature Biotechnology*, vol. 28(7), pp. 727–732, 2010, https://doi.org/10.1038/nbt.1642, PMID: 20562863.

[76] R. W. Farndale, J. J. Sixma, M. J. Barnes, and P. G. DeGroot, "The role of collagen in thrombosis and hemostasis," *Journal of Thrombosis and Haemostasis*, vol. 2(4), pp. 561–573, 2004, https://doi.org/10.1111/j.1538-7836.2004.00665.x, PMID: 15102010.

[77] A. T. Franco, A. Corken, and J. Ware, "Platelets at the interface of thrombosis, inflammation, and cancer," *Blood*, vol. 126(5), pp. 582–588, 2015, https://doi.org/10.1182/blood-2014-08-531582, PMID: 26109205.

[78] P. Kubes, "The versatile platelet contributes to inflammation, infection, hemostasis, coagulation and cancer," *Seminars in Immunology*, vol. 28(6), p. 535, 2016, https://doi.org/10.1016/j.smim.2016.11.002.

[79] H. H. Versteeg, J. W. Heemskerk, M. Levi, and P. H. Reitsma, "New fundamentals in hemostasis," *Physiology Review*, vol. 93, pp. 327–358, 2013, https://doi.org/10.1152/physrev.00016.2011.

[80] J. Thon, L. Mazutis, S. Wu, J. L. Sylman, A. Ehrlicher, K. R. Machlus, Q. Feng, S. Lu, R. Lanza, K. B. Neeves, D. A. Weitz, and J. E. Italiano, "Platelet bioreactor-on-a-chip," *Blood*, vol. 124(12), pp. 1857–1867, 2014, https://doi.org/10.1182/blood-2014-05-574913, PMID: 25606631.

[81] Joint Committee for Guides in Metrology (JCGM), *International vocabulary of metrology - Basic and general concepts and associated terms (VIM)*, 3rd ed., 2012.

[82] Joint Committee for Guides in Metrology (JCGM), *Evaluation of measurement data - Guide to the expression of uncertainty in measurement (GUM)*, 1st ed., 2008.

[83] Agilent Technology, *Agilent E4980A Precision LCR Meter Users Guide*, 7th ed., 2008, Manufacturing No. E4980-90070, http://www.agilent.com/find/e4980a.

[84] A. R. Hibbs, *Confocal microscopy for biologists*. Springer Science Business Media LLC, New York, 1st ed., April 2004, ISBN: 978-1-4757-0983-4.

[85] B. Matsumoto, *Cell biological applications of confocal microscopy*. Academic Press, Cambridge, Massachusetts, 2nd ed., December 2002, ISBN: 978-0-124-80277-3.

[86] M. Muller, *Introduction to confocal fluorescence microscopy*. Shaker Publishing B.V., Maastricht, The Netherlands, 2002, ISBN: 978-9-042-30203-7.

[87] S. W. Paddock, *Confocal microscopy methods and protocols*. Humana press, Totowa, New Jersey, 1999, ISBN: 0-89603-526-3.

[88] M. Gu, *Principles of three-dimensional imaging in confocal microscopes*. World Scientific, Singapore, 1996, ISBN: 981-02-2550-4.

[89] A. R. Clarke and C. N. Eberhardt, *Microscopy techniques for materials science*. Woodhead Publishing, Sawston, Cambridge, 1st ed., October 2002, ISBN: 978-1-855-73587-3.

[90] M. Minsky, "Memoir on inventing the confocal scanning microscope," *Scanning: Journal of Scanning Microscopies*, vol. 10(4), pp. 128–138, 1988, https://doi.org/10.1002/sca.4950100403.

[91] M. Minsky, "Microscopy apparatus," Patent number: US3013467, December 1961, http://www.freepatentsonline.com/3013467.html.

[92] P. Davidovits and M. D. Egger, "Scanning laser microscope for biological investigations," *Applied Optics*, vol. 10 (7), p. 1615–1619, 1971, https://doi.org/10.1364/AO.10.001615, PMID: 20111173.

[93] P. Davidovits and M. D. Egger, "Scanning laser microscope," *Nature*, vol. 223, p. 831, 1969, https://doi.org/10.1038/223831a0, PMID: 5799022.

[94] K. R. Spring and S. Inoue, *Video microscopy: the fundamentals*. Plenum Press, New York, 2nd ed., 1997, ISBN: 978-0-306-45531-5.

[95] J. R. Swedlow, K. Hu, P. D. Andrews, D. S. Roos, and J. M. Murray, "Measuring tubulin content in toxoplasma gondii: a comparison of laser-scanning confocal and wide-field fluorescence microscopy," *Proceedings of the National Academy of Sciences of the United States of America*, vol. 99(4), p. 2014–2019, 2001, https://doi.org/10.1073/pnas.022554999, PMID: 11830634.

[96] E. H. K. Stelzer, "Contrast, resolution, pixelation, dynamic range and signal- to-noise ratio: fundamental limits to resolution in fluorescence light microscopy," *Journal of Microscopy*, vol. 189(1), pp. 15–24, 1998, https://doi.org/10.1046/j.1365-2818.1998.00290.x.

[97] D. B. Murphy, *Fundamentals of light microscopy and electronic imaging*. J. Wiley and Sons Inc., Hoboken, New Jersey, 1st ed., 2001, ISBN: 0-471-25391-X.

[98] Imaris - microscopy image analysis software (Bitplane), http://www.bitplane.com.

[99] Amira (Thermo Fisher Scientific), https://www.fei.com/software/amira-avizo.

[100] Volocity (PerkinElmer), http://www.perkinelmer.com/it/lab-products-and-services/resources/cellular-imaging-software-downloads.html.

[101] MetaMorph - microscopy automation and image analysis software (Molecular Devices), https://www.moleculardevices.com/products/cellular-imaging-systems/acquisition-and-analysis-software/metamorph-microscopy.

[102] *Image processing and analysis in Java - ImageJ*, https://imagej.nih.gov/ij/.

[103] CellProfiler - cell image analysis software, http://cellprofiler.org.

[104] Starrynite, http://starrynite.sourceforge.net.

[105] A. Gordon, A. ColmanLerner, T. E.Chin, K. R. Benjamin, R. C. Yu, and R. Brent, "Single-cell quantification of molecules and rates using open-source microscope-based cytometry," *Nature Methods*, vol. 4(2), pp. 175–181, 2007, https://doi.org/10.1038/nmeth1008, PMID: 17237792.

[106] D. W. D, S. Kuhl, and D. R. Soll, "Application of 2d and 3d dias to motion analysis of live cells in transmission and confocal microscopy imaging," *Methods in Molecular Biology*, vol. 346, pp. 261–279, 2006, https://doi.org/10.1385/1-59745-144-4:261, PMID: 16957296.

[107] A. E. Carpenter, T. R. Jones, M. R. Lamprecht, C. Clarke, I. HanKang, and O. Friman, "Cellprofiler: image analysis software for identifying and quantifying cell phenotypes," *Genome Biology*, vol. 7(10), p. R100, 2006, https://doi.org/10.1186/gb-2006-7-10-r100, PMID: 17076895.

[108] Z. Bao, J. I. Murray, S. L. Ooi, M. J. Sandel, and R. H. Waterston, "Automated cell lineage tracing in caenorhabditis elegans," *Proceedings of the National Academy of Sciences of the*

United States of America, vol. 103(8), p. 2707–2712, 2006, https://doi.org/10.1073/pnas.0511111103, PMID: 16477039.

[109] R. W. Sabnis, *Handbook of fluorescent dyes and probes*. J. Wiley and Sons Inc., Hoboken, New Jersey, 1st ed., June 2015, ISBN: 978-1-118-02869-8.

[110] S. A. Stricker, V. E. Centonze, S. W. Paddock, and G. Schatten, "Confocal microscopy of fertilization-induced calcium dynamics in sea urchin eggs," *Developmental Biology*, vol. 149(2), pp. 370–380, 1992, https://doi.org/10.1016/0012-1606(92)90292-O, PMID: 1730391.

[111] A. P. J. end E. D. Salmon and S. K. Bloom, "Counting kinetochore protein numbers in budding yeast using genetically encoded fluorescent proteins," *Methods in Cell Biology*, vol. 85, pp. 127–151, 2008, https://doi.org/10.1016/S0091-679X(08)85007-8, PMID: 18155462.

[112] D. E. Wolf, C. Samarasekera, and J. R. Swedlow, "Quantitative analysis of digital microscope images," *Methods in Cell Biology*, vol. 81, pp. 365–396, 2007, https://doi.org/10.1016/S0091-679X(06)81017-4, PMID: 17519175.

[113] B. Huang, W. Wang, M. Bates, and X. Zhuang, "Three-dimensional super-resolution imaging by stochastic optical reconstruction microscopy," *Science*, vol. 319(5864), p. 810–813, 2008, https://doi.org/10.1126/science.1153529, PMID: 18174397.

[114] S. Manley, J. M. Gillette, G. Patterson, H. Shroff, H. F. Hess, E. Betzig, and J. LippincottSchwartz, "High-density mapping of single-molecule trajectories with photoactivated localization microscopy," *Nature Methods*, vol. 5(2), p. 155–157, 2008, https://doi.org/10.1038/nmeth.1176, PMID: 18193054.

[115] L. S. Churchman, Z. Okten, R. S. Rock, J. F. Dawson, and J. A. Spudich, "Single molecule high-resolution colocalization of cy3 and cy5 attached to macromolecules measures intramolecular distances through time," *Proceedings of the National Academy of Sciences of the United States of America*, vol. 102(5), pp. 1419–1423, 2005, https://doi.org/10.1073/pnas.0409487102, PMID: 15668396.

[116] A. Yildiz and P. R. Selvin, "Fluorescence imaging with one nanometer accuracy: application to molecular motors," *Accounts of Chemical Research*, vol. 38(7), p. 574–582, 2005, https://doi.org/10.1021/ar040136s, PMID: 16028892.

[117] B. Bhushan, *Handbook of nanotechnology*. Springer, Germany, 2017, ISBN: 978-3-662-54355-9.

[118] J. Hubbell and L. V. McIntire, "Technique for visualization and analysis of mural thrombogenesis," *Review of Scientific Instruments*, vol. 57(5), pp. 892–897, 1986, https://doi.org/10.1063/1.1138830.

[119] R. Specogna, "Complementary geometric formulations for electrostatics," *International Journal for Numerical Methods in Engineering*, vol. 86(8), pp. 1041–1068, 2011, https://doi.org/10.1002/nme.3089.

[120] P. Bettini, R. Specogna, and F. Trevisan, "Electroquasistatic analysis of the gas insulated line for the iter neutral beam injector," *IEEE Transactions on Magnetics*, vol. 45(3), pp. 996–999, 2009, https://doi.org/10.1109/TMAG.2009.2012538.

[121] P. Dular, R. Specogna, and F. Trevisan, "Constitutive relations for discrete geometric approach over hexahedral grids," *IEEE Transactions on Magnetics*, vol. 46(8), pp. 3077–3080, 2010, https://doi.org/10.1109/TMAG.2010.2043653.

[122] L. Codecasa, R. Specogna, and F. Trevisan, "Discrete constitutive equations over hexahedral grids for eddy-current problems," *CMES Computer Modeling in Engineering and Sciences*, vol. 31(3), pp. 129–144, 2008, https://doi.org/10.3970/cmes.2008.031.129.

[123] P. Dular, R. Specogna, and F. Trevisan, "Constitutive matrices using hexahedra in a discrete approach for eddy currents," *IEEE Transactions on Magnetics*, vol. 44(6), pp. 694–697, 2008, https://doi.org/10.1109/TMAG.2007.916230.

[124] C. E. Shannon and D. W. Hagelbarger, "Concavity of resistance functions," *Journal of Applied Physics*, vol. 27(1), pp. 42–43, 1956, https://doi.org/10.1063/1.1722193.

[125] PerkinElmer, *3D Image Analysis Software - Volocity User Guide*, 22nd ed., 2011, http://www.perkinelmer.com/.

[126] C. H. Chen, *Signal processing handbook*. Marcel Dekker Inc., New York, 1988, ISBN: 0-8247-7956-8.

[127] J. R. Macdonald, *CNLS immittance, inversion and simulation fitting programs - LEVM/LEVMW Manual*, 2015, http://www.jrossmacdonald.com.

[128] A. Zhbanov and S. Yang, "Effects of aggregation on blood sedimentation and conductivity," *PLoS One*, vol. 10(6):e0129337, 2015, https://doi.org/10.1371/journal.pone.0129337.

[129] F. G. Hirsch, E. C. J. Texter, L. A. Wood, W. C. J. Ballard, F. E. Horna, and I. S. Wright, "The electrical conductivity of blood," *Blood*, vol. 5(11), pp. 1017–1035, 1950, PMID: 14791582.

[130] K. Pearson, "Notes on regression and inheritance in the case of two parents," *Proceedings of the Royal Society of London*, vol. 58, pp. 240–242, 1895, https://doi.org/10.1098/rspl.1895.0041.

Scientific production of the author

Research articles

D. De Zanet, M. Battiston, E. Lombardi, R. Specogna, F. Trevisan, L. De Marco, A. Affanni, M. Mazzucato, "A new method for the accurate platelet thrombi volume measurement using confocal microscope," ***Acta Imeko***, **2018** (accepted, in editing).

D. De Zanet, M. Battiston, E. Lombardi, A. Da Ponte, R. Specogna, F. Trevisan, L. De Marco, A. Affanni, M. Mazzucato, "Fast blood impedance measurements as quality indicators in the pre–analytical phase to prevent laboratory errors," ***Acta Imeko***, vol. 7(4), pp. 26-32, **2018**.

D. De Zanet, M. Battiston, E. Lombardi, R. Specogna, F. Trevisan, L. De Marco, A. Affanni, M. Mazzucato, "Impedance biosensor for real–time monitoring and prediction of thrombotic individual profile in flowing blood," ***PLoS ONE***, vol. 12(9): e0184941, **2017**, https://doi.org/10.1371/journal.pone.0184941, PMID: 28922391.

Oral presentations

D. De Zanet, A. Affanni, M. Mazzucato, "Monitoring and prediction of the individual thrombotic profile from electrical impedance measurements," ***XXXV Congresso Nazionale di Misure Elettriche ed Elettroniche – GMEE***, **2018**, September 17-19, Padova .

D. De Zanet, A. Affanni, M. Mazzucato, "New methodologies for the study of hemostasis in oncology – Electrical impedance sensing and signal processing," ***VII Conferenza del Dottorato di Ricerca*** *in Ingegneria Industriale e dell'Informazione*, **2018**, May 24, Udine.

D. De Zanet, M. Battiston, E. Lombardi, A. Da Ponte, R. Specogna, F. Trevisan, A. Affanni, M. Mazzucato, "Blood components characterization for

preanalytical rapid quality controls through impedance measurements," ***22nd IMEKO TC4 International Symposium*** *and 20th International Workshop on ADC Modelling and Testing*, **2017**, September 14-15, Iasi – Romania, ***International Best Paper Award***.

D. De Zanet, A. Affanni, M. Mazzucato, "Structural and functional blood characterization through electrical impedance sensing and optical signals analysis – from laboratory to clinic," ***VI Conferenza del Dottorato di Ricerca*** *in Ingegneria Industriale e dell'Informazione*, **2017**, May 25, Udine.

D. De Zanet, A. Affanni, M. Mazzucato, "Sviluppo di nuove metodologie elettromagnetiche per lo studio dell'emostasi globale in ambito oncologico," ***V Conferenza del Dottorato di Ricerca*** *in Ingegneria Industriale e dell'Informazione*, **2016**, May 26, Udine.

Other papers

D. De Zanet, M. Battiston, E. Lombardi, R. Specogna, F. Trevisan, A. Affanni, M. Mazzucato, "Misure di impedenza elettrica di campioni biologici in fase pre-analitica per prevenire errori nelle analisi di laboratorio," ***XXXIII Congresso Nazionale di Misure Elettriche ed Elettroniche – GMEE***, **2018**, September 17-19, Padova (proceeding - poster).

D. De Zanet, M. Battiston, E. Lombardi, R. Specogna, F. Trevisan, A. Affanni, M. Mazzucato, "Monitoraggio e predizione del profilo trombotico individuale mediante misure di impedenza elettrica," ***XXXIII Congresso Nazionale di Misure Elettriche ed Elettroniche – GMEE***, **2018**, September 17-19, Padova (proceeding - oral presentation).

D. De Zanet, A. Affanni, M. Mazzucato, "New methodologies for the study of hemostasis in oncology – Electrical impedance sensing and signal processing," ***VII Conferenza del Dottorato di Ricerca*** *in Ingegneria Industriale e dell'Informazione*, **2018**, May 24, Udine (poster - oral presentation).

M. Battiston, K.B. Neeves, **D. De Zanet**, E. Lombardi, F. Agostini, A. Da Ponte, C. Durante, L. De Marco, M. Mazzucato, "Il ruolo dei recettori estrogenici sulla funzionalità piastrinica in condizioni di flusso," ***43° Convegno Nazionale di Studi di Medicina Trasfusionale – SIMTI***, **2018**, May 23-25, Genova (abstract - poster).

M. Battiston, K.B. Neeves, **D. De Zanet**, E. Lombardi, F. Agostini, A. Da Ponte, C. Durante, L. De Marco, M. Mazzucato, "New insights on calcium signaling and platelet function following estrogen receptors stimulation," ***25th***

Biennial International Congress on Thrombosis – BIC, **2018**, May 23-26, Venezia (abstract - poster).

D. De Zanet, M. Battiston, E. Lombardi, A. Da Ponte, R. Specogna, F. Trevisan, A. Affanni, M. Mazzucato, "Blood components characterization for preanalytical rapid quality controls through impedance measurements," ***22nd IMEKO TC4 International Symposium*** *and 20th International Workshop on ADC Modelling and Testing*, **2017**, September 14-15, Iasi – Romania (proceeding) ***International Best Paper Award***.

D. De Zanet, M. Battiston, E. Lombardi, R. Specogna, F. Trevisan, A. Affanni, M. Mazzucato, "FluoLab: a new easy-to-use Graphical User Interface for the multi-cell functional calcium signals analysis," ***22nd IMEKO TC4 International Symposium*** *and in Ingegneria Industriale e dell'Informazione*, ***22nd IMEKO TC4 International Symposium*** *and 20th International Workshop on ADC Modelling and Testing*, **2017**, September 14-15, Iasi – Romania (proceeding).

D. De Zanet, A. Affanni, M. Mazzucato, "Structural and functional blood characterization through electrical impedance sensing and optical signals analysis – from laboratory to clinic," ***VI Conferenza del Dottorato di Ricerca*** *in Ingegneria Industriale e dell'Informazione*, **2017**, May 25, Udine (poster - oral presentation).

M. Battiston, F. Agostini, E. Lombardi, **D. De Zanet**, S. Zanolin, M. Michieli, M. Rupolo, L. De Marco, C. Di Buduo, A. Balduini, A. Da Ponte, C. Durante, M. Mazzucato, "Il differenziamento megacariocitario e la formazione di piastrine a partire da cellule CD34+ criopreservate: dal laboratorio alla clinica," ***5a Conferenza Nazionale dei Servizi Trasfusionali – SIMTI***, **2017**, May 25-27, Firenze (abstract - poster).

D. De Zanet, A. Affanni, M. Mazzucato, "Misure di trombo – formazione da segnali di impedenza elettrica: identificazione di eventi critici in tempo reale," ***XXXIII Congresso Nazionale di Misure Elettriche ed Elettroniche – GMEE***, **2016**, September 19-21, Benevento (proceeding - poster).

D. De Zanet, A. Affanni, M. Mazzucato, "Misure di trombo – formazione con microscopio confocale: l'accuratezza dei dati nella ricerca biomedica," ***XXXIII Congresso Nazionale di Misure Elettriche ed Elettroniche – GMEE***, **2016**, September 19-21, Benevento (proceeding - poster).

F. Agostini, M. Battiston, E. Lombardi, **D. De Zanet**, S. Zanolin, M. Valvasori, B. Tommasini, L. De Marco, A. Da Ponte, C. Durante, M. Mazzucato, "An optimized expansion protocol of adipose mesenchymal stem cells can im-

prove homing potential and calcium signaling in fluid dynamic conditions," ***VII meeting Stem Cell Research Italy***, **2016**, June 21-23, Bologna (abstract - poster).

D. De Zanet, A. Affanni, M. Mazzucato, "Sviluppo di nuove metodologie elettromagnetiche per lo studio dell'emostasi globale in ambito oncologico," ***V Conferenza del Dottorato di Ricerca*** *in Ingegneria Industriale e dell'Informazione*, **2016**, May 26, Udine (poster - oral presentation).

Research articles in preparation

M. Battiston, K.B. Neeves, E. Lombardi, **D. De Zanet** et al., "Estrogen receptors and platelet calcium signaling," (draft).

M. Battiston, **D. De Zanet** et al., "Intercellular and intracellular Ca2+ signaling via serotonin 5-HT2A receptors," (draft).

M. Battiston, F. Agostini, E. Lombardi, **D. De Zanet** et al., "Crucial role for Ca2+ signaling in megakaryocytes and platelet maturation," (draft).

Acknowledgements

Foremost, I would like to express my sincere gratitude to my Supervisors Prof. Antonio Affanni and Dr. Mario Mazzucato, for the opportunity of these Ph.D. studies and research, for their suggestions, their insightful comments and their support.

My sincere thanks also goes to all the people of the team, for the stimulating discussions and their esteem, for their high patience and motivation.

A special thanks goes to the new people discovered during this experience and revealed friends, for their encouragement, their true affection and for all the fun had in these years togheter.

Last but not the least, I would like to thank my family and all the people who believed in my capabilities and supported me with carefulness throughout these years. I could not have imagined receiving better people for my life.